UNIVERSIDAD COMPLUTENSE DE MADRID
FACULTAD DE CIENCIAS FÍSICAS

TESIS DOCTORAL

Optics-measurement-based Beam Position Monitor calibration

Calibración de monitores de posición del haz basado en medidas ópticas

MEMORIA PARA OPTAR AL GRADO DE DOCTOR

PRESENTADA POR

Ana García-Tabares Valdivieso

Director

Rogelio Tomás García

Madrid

Universidad Complutense de Madrid
Facultad de Ciencias Físicas
Departamento de Estructura de la Materia, Física Térmica y Electrónica

Optics-measurement-based Beam Position Monitor calibration.
Calibración de monitores de posición del haz basado en medidas ópticas.

por

Ana García-Tabarés Valdivieso

bajo la supervisión de:

Rogelio Tomás García

Memoria para optar al grado de doctor en Ciencias Físicas
Julio 2019

Abstract

Accurate measurements of the focusing properties of an accelerator are essential for proper operation of a synchrotron, both for the machine protection and for the performance of the experiment. Measurement of linear optics functions based on turn-by-turn measurements has been developed continuously in pursuit of more accurate results [1, 2, 3, 4].

Optics functions that describe the focusing properties of the machine can be obtained from different observables: phase and amplitude of the transverse betatron oscillations and the change of the tune by modulating the current of quadrupoles (K-modulation) [5]. Reconstruction of linear optics using the phase, in combination with K-modulation, have been the main approaches for obtaining the β function in accelerators all over the world [3, 6, 7]. Measurements of optics functions based on the amplitude [8], denoted as β from amplitude, have not been used as widely as the other methods since it requires accurate beam-position-monitor (BPM) calibration. BPMs are key elements in accelerator operation, providing essential information about different beam parameters that are directly related to the accelerator performance. BPMs are calibrated before its installation in the accelerator to obtain an accurate conversion from an induced voltage to the centre of charge position. This calibration procedure can only be performed when the accelerator is in a period of non-activity and does not completely reproduce the exact conditions that occur during the machine operation.

The studies presented in this thesis have served as improvement of the β from amplitude approach, β^{A}, and they can be summarized in two groups: developing of the uncertainty associated to the β-function and mitigation of the BPM calibration factors effects.

First, a study of the error-bar associated with the measured β^{A}-function is introduced using an analytical formalism that has been contrasted with simulations and experimental results [9, 10].

Second, a study of the BPM calibration factors based on optics measurements has been developed as part of this research. Discrepancies observed during the optics measurements at the Large Hadron Collider (LHC) and the Proton Synchrotron Booster (PSB) between different β-reconstruction approaches, show that the impact of the BPM calibration factors on the optics functions was higher than expected from the design values and tolerances. Measurement of the optics functions allows obtaining extra information on BPM calibration together with its associated uncertainty and resolution. This thesis summarizes the development of two different techniques to compute the BPMs calibration factors based on optics measurements accurately. These approaches have been developed using as a test bench the LHC and the PSB, and it is foreseen to extrapolate them to future accelerators. In case of LHC, the optics developed for computing the calibration factors only allows to accurately calibrate a limited range of BPMs located in the vicinity of the experiments denoted as IRs [11, 12].

The implementation of this approach in LHC and PSB is introduced in this thesis. Together with a summary of the hardware and software upgrades needed for its implementation. In case of LHC, calibration factors have been implemented in different machine configurations, in which the β-function can be measured accurately using the three different approaches previously introduced: β^{ϕ}, β^{A} and K-modulation. In LHC IRs BPMs a systematic deviation of the BPM calibration was observed when reconstructing the β-function using the β^{A}-method with respect to the results obtained using the β^{ϕ} approach. By compensating the effect of the calibration factors in the measured β^{A}-function, the average accuracy of the β-function has improved in a 6% in Beam 1 and 4% in Beam 2 with respect to the direct measured β^{A}-function [12]. On the other hand, in case of PSB, the validation of the calibration optics has been performed using the nominal optics used during the routine operations. Calibrating the BPMs using an optics-based approach has allowed decreasing the β-function error bar, previously computed using the β^{ϕ} approach, by a factor of three [13].

Abstract

Poder medir de forma precisa las propiedades de enfoque de un acelarador es extremadamente importante para una adecuada operación del sincrotrón, tanto desde el punto de vista de proteccioń de los componentes del acelerador como desde el punto de vista del rendimiento de los experimentos [1, 2, 3, 4].

Las funciones ópticas, que describen las propiedades de enfoque del acelerador, se pueden obtener mediante distintos observables: fase y amplitud de las oscilaciones betatrónicas que realiza el haz en el plano transversal, o mediante la medida del tono mediante la modulación de la corriente en los cuadrupolos (K-modulation) [5]. En concreto, la reconstrucción de la parte linear de la óptica del acelerador se ha basado durante los últimos años en las medidas de fase y K-modulation. [3, 6, 7]. Las medidas de la óptica basadas en la amplitud [8] no han sido usadas

de forma tan extensiva como los otros dos métodos anteriores ya que están afectadas por los factores de calibración de los monitores de posición del haz (BPMs). Los BPMs son una pieza fundamental para la correcta operación del acelerador, que deben ser calibrados antes de ser instalados en el acelerador para, de esta forma, poder obtener una conversión precisa de volaje inducido a posición del centro de carga del haz. El procedimiento de calibración sólo se puede realizar cuando el acelerador está en periodo de no actividad y, por lo tanto no reproducen completamente las condiciones que ocurren durante la operación del mismo.

Los estudios presentados en esta tesis han servido como mejora del método de medida de β basado en la amplitud de las oscilaciones betatrónicas, β^{A}, se pueden resumir en dos grupos: desarrollo de las barras de error asociadas a la función β y mitigación del efecto de los factores de calibración en los BPMs.

En primer lugar, el estudio de la barra de error de la función β se ha realizado mediante desarrollo teórico que se ha contrastado tanto con simulaciones como con resultados expermientales [9, 10].

En segundo lugar, un nuevo método de calibración de BPMs basado en medidas ópticas se ha desarrollado con el objetivo de completar las actuales técnicas de calibración. Al realizar medidas ópticas tanto en el Large Hadron Collider (LHC) como en el Proton Synchroton Booster (PSB), se observó que el impacto de los factores de calibración en las medidas era mayor que el determinado por las especificaciones. La medida de la óptica del acelerador, concretamente la función β, permite obtener los factores de calibración de los BPMs junto con su indeterminación y su resolución. Esta tesis resume el desarrollo de dos técinas que permiten medr los factores de calibración de forma precisa. Estos métodos se han desarrollado en el LHC y en el PSB y está previsto que se extrapolen a otros aceleradores. En el caso del LHC, se ha desarrollado una óptica específica que permite calcuar los factores de calibración de los BPMs situados cerca de los experimentos (IRs) [11, 12]. La implementación de estos nuevos métodos de calibración se detalla en la tesis junto con un resumen de los cambios realizados tanto a nivel de hardware como a nivel de software. En el caso del LHC los factores de calibración se han implementado en distintas configuraciones donde la función β se puede medir de forma precisa con cualquiera de los tres métodos previamente descritos: β^{ϕ}, β^{A} y K-modulation. Esta diferencia sistemática se redujo de media en un 6% en el Beam 1 del acelerador y un 4% en el Beam 2 al compensar el efecto de los factores de calibración [12, 11]. Por otro lado, en el caso del PSB, la validación de la medida de los factores de calibración se ha realizado utilizando la óptica que se utiliza durante la operación normal del acelarador. Se ha observado que al calibrar los BPMs utilizando medidas ópticas es posible reducir la barra de error de la función β, calculada anteriormente utilizando medidas de fase, en un factor tres [13].

Acknowledgements

I can still remember my first day at CERN, excitement and nervousness of the start of a new journey. Almost five years have already passed since that day, and now Im completely sure that it would have not been possible without the support of numerous people.

I want to express my gratitude, in first place, to my supervisor Rogelio Tomás García. The work presented in this thesis would have not been possible without his knowledge, motivation, advice and patience. I also want to thank my university supervisor Luis Mario Fraile for his help with tedious administrative tasks.

During my first months at CERN I had the opportunity to take part in the LHC commissioning. All along these long and stressful days I managed to get into accelerators world thanks to the explanations of the Optics team members: Rogelio Tomás, Ewen McLean, Tobias Persson, Andy Langner and the Engineers in Charge: Giulia Papotti, Matteo Solfaroli and Belen Salvachua.

I would like to specially acknowledge Meghan Mcateer for teaching me how to operate the Protons Synchrotron Booster before she left CERN. Working on this small accelerator has been very challenging for me, and I would like to express my gratitude to many CERN colleagues who helped me in this task: Fanouria Antoniou, Bettina Mikulec, Elena Benedetto, Jeroen Belleman, Gian Piero di Giovanni. Thanks to all for letting me take part in the optics measurements project, giving me a chance to assume some responsibilities, and allowing me to grow in my career as researcher.

The post-processing of the optics measurements (LHC and PSB) and in general a well balanced work/rest ratio would not have been possible without the help of Jaime Maria Coello de Portugal Martinez Acacio, or Jaimeeeeee when the code was not working.

A PhD would not be the same without the constant support, motivation, funny moments provided by the best office mates ever. I thank Javier Barranco, for his sarcastic sense of humour and advice on how to survive to CERN, Laurent Barraud, for his curiosity, Lukas Malina for sharing the most fruitful coffee breaks, Gerardo Cantón for his Mexican sense of humour and Sergey Antipov for probably being the worst teacher of Russian and the best adventure organizer.

My time at CERN was fun and exciting thanks to the help of friends Elena Fol, Joschua

Dilly (also OMC members), Alejandro Sanz, Paul Thrane (aka the amazing photographer) Agnieszcka and the HIIT Spartan team.

For me, defending a PhD has been not only a process of five years. It was a longer journey that started with my first day of school and had only been possible with the continuous support of my family.

Gracias a mis abuelos, Carmen y Epifanio, Elisa y Luis, por tener solo buenos ojos para sus nietos, por sus palabras llenas de cario que tanto nos han subido la moral y por su constante ayuda económica que nos ha permitido ir ahorrando durante toda nuestra etapa como estudiantes.

Gracias a mis padres por haberme enseñado que el trabajo y la constancia son fundamentales para conseguir distintos objetivos a lo largo de la vida. A mi madre, por su constante ayuda con el orden y la organización, una tarea bastante complicada y a veces no muy agradecida. A mi padre, por dar respuesta a todas mis dudas científicas y tecnológicas desde que, de pequeña de camino al cole, me explicaba cómo funcionaban los coches.

Gracias a mis hermanas Carmen y Elisa por ser un modelo a seguir desde cuando mi memoria alcanza. Por ser una combinación entre segunda (y tercera) madre para mi, profesora particular y personal shopper.

Quiero agradecerles a todos su infinita paciencia durante estos últimos 28 aos, solo me ha hecho falta hacer una tesis doctoral para darme cuenta de todo su apoyo y cariño!

A mis sobrinos, Andrés, Luis y Elisa (y los que están por venir) porque su sonrisa y sus Te quiero mil mil le alegran el día a cualquiera.

Dedication

A la memoria de mis abuelos Luis y Epifanio.

“Beati hispani, qvibvs vivere bibere es*”

“Dichosos los hispanos, para los que vivir es beber”

“Happy are those Hispanics for whom living is drinking”

* Nota: En referencia a que los hispanos no distinguen el sonido [b] del * sonido [v] en latin.

Contents

List of Tables

List of Figures

Chapter 1

Introduction

Accelerator science focuses on the study of machines that are used for accelerating, storing and transporting charged particles using electromagnetic fields. These machines are referred to as particle accelerators, or simply accelerators. More in detail, one of the goals of accelerator physics is to describe the dynamics of the particles in an accelerator.

Accelerators have been evolving since the 1930s [18] and high-energy physics research has always been the driving force behind their development, allowing to reach higher beam energies and intensities. On the other hand, particle accelerators have been evolving through time as a consequence of the improvements developed in the fields of particle physics, electromagnetism, radiofrequency and magnet technology within the last century [19, 20].

Classification of accelerators can be performed according to their geometry- linear and circular or according to the kind of particles that are being accelerated- leptons or hadrons. Circular accelerators can be, at the same time, subdivided in two groups: synchrotons or cyclotrons. This thesis is focused on the study of synchroton accelerators where the distribution of the magnetic field defines a closed-loop. In a synchrotron the magnetic field which bends the particle beam into its closed path increases with time during the accelerating process, being synchronized to the increasing kinetic energy of the particles. Accelerators are not only used in high energy physics (HEP) but in many other different fields such as industry, medical applications and material science research [21]. In case of the HEP, colliders are more extended than fixed target synchroton allowing to reach higher energy. The beam energy, together with the type of particles being accelerated will define the machine physics goal. Beam energy has been increased since the beginning of accelerator science (Fig. 1.1), allowing the discovery of new elementary particles [22, 23, 24] and to have a complete version of the standard model. In particular, the LHC is a key accelerator based instrument of study for a wide range of high energy (HEP) phenomena.

Further and more detailed information of accelerators can be found in [25, 26, 27, 28].

1.1 Transverse beam dynamics

Beam dynamics has been widely covered in many textbooks [25, 26, 27]. This chapter aims to briefly describe the key terms that are needed to contextualize the work introduced in this

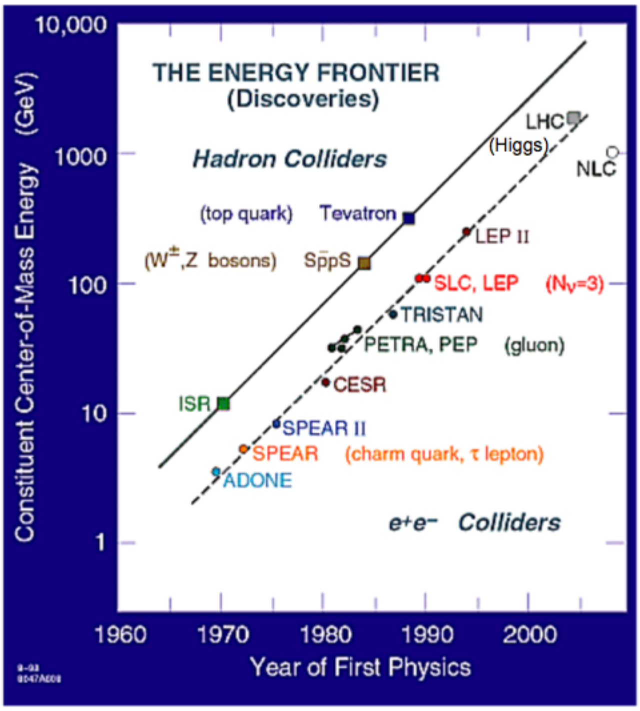

Figure 1.1: Evolution of beam energy as function of time.

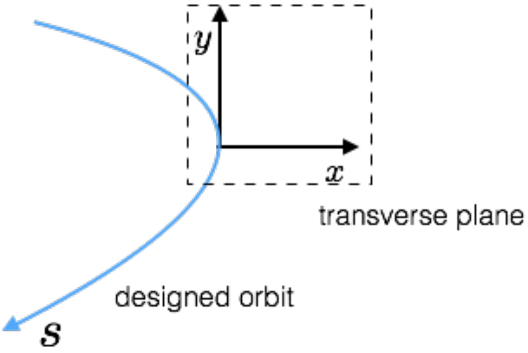

Figure 1.2: Frenet-Serret coordinate system.

thesis.

Beam dynamics describes the motion of a charged particle affected by an electric and a magnetic field. Specific, linear beam dynamics is focused on the effect of dipolar and quadrupolar fields in the trajectory of the particle. It is necessary to define a coordinate system to describe the trajectory of a particle. The most commonly used coordinate system is the Frenet-Serret system, a non-inertial coordinate system that travels with the particle. Particle motion is described with respect to a reference orbit (x,y,s) as is shown in Fig. (1.2).

In case of a circular accelerator, such as LHC or PSB, charged particles have to be guided to describe the desired trajectory. Dipolar fields, illustrated in Figs. 1.3, act as a guidance for the particles. The local radius ρ(s) can be obtained by combining the forces acting on the beam, the centripetal force and the Lorentz force:

$$\mathrm{m}\gamma\frac{v^2}{\rho} = e[\vec{v} \times \vec{B}(s)] \tag{1.1}$$

where m is the particle mass, v is the particles speed, ρ is the curvature radius as shown in Fig. 1.2, e is the elementary charge, γ is the relativistic Lorentz factor defined as $\gamma = \frac{1}{\sqrt{1-v^2/c^2}}$, $\vec{B}$ is the magnetic flux. Therefore the local bending radius can be expressed in terms of the magnetic flux density and the particle momentum:

$$\frac{1}{\rho(s)} = \frac{eB}{p} \tag{1.2}$$

In real operation, dipolar errors will perturb the designed closed orbit.

Restoring forces, similar to the spring, are needed to adjust the transverse size of the beam. Quadrupolar field, illustrated in Figs. 1.4 provides the needed restoring force, linearly proportional to this distance from the quadrupole axis. The magnetic field produced by a quadrupole is given by:

$$\begin{aligned} B_x &= -gy \\ B_y &= -gx \end{aligned} \tag{1.3}$$

where g relates the field gradient to its focusing effect. And therefore, the resulting force acting on the particle is given by:

$$\begin{aligned} F_x &= evB_y = -evgx \\ F_y &= -evB_x = evgy \end{aligned} \tag{1.4}$$

The focusing strength of a quadrupole, is defined normalized to the beam rigidity, k:

$$k = \frac{e}{p}g = \frac{ec}{\beta E}g, \quad k[m^{-2}] = \frac{0.2998g \quad [\mathrm{T/m}]}{\beta E[\mathrm{GeV}]}$$

where β is the ratio between the particle speed and the speed of light $\frac{v}{c}$ and E is the beam energy.

The effect of the quadrupole on the beam is comparable to the impact of an optical lens. The quadrupole focuses the beam when the direction of the force is toward the centre and defocuses the beam when the force acts in the opposite direction. The restoring effect is only present in one plane while in the other plane a defocusing force acts on the beam. A combination of focusing and defocusing forces have to be applied to keep the beam focused on both planes. Though a quadrupole is focusing only on one plane and defocusing in the other plane, it has been demonstrated in [29], that a sequence of alternating quadrupoles can have a net focusing effect on both planes.

A second-order differential equation describes the motion of particle travelling in a lattice created by quadrupoles and dipoles under the effect of the forces generated by the magnetic

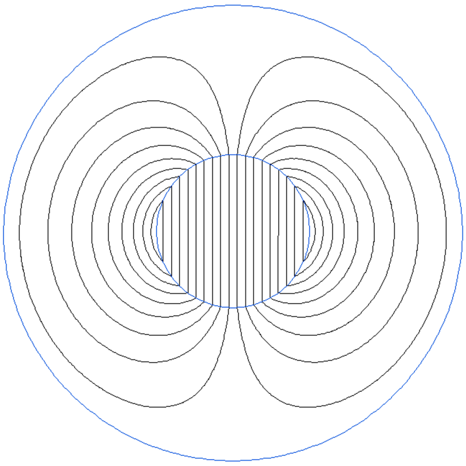

Figure 1.3: Dipolar magentic field lines.

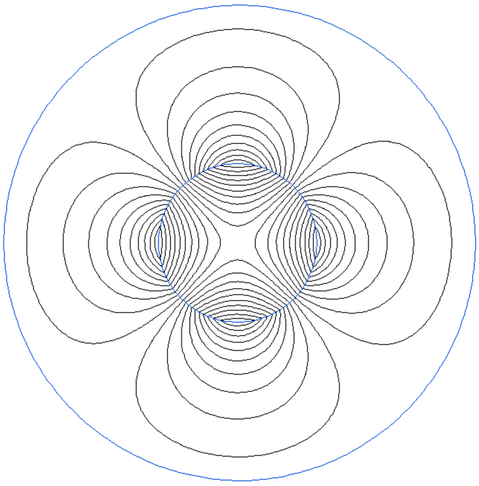

Figure 1.4: Quadrupolar magnetic field lines.

fields like the harmonic oscillator. This differential equation of motion, for an arbitrary plane z, x or y, is given by:

$$z'' + K_z(s) = 0 \tag{1.5}$$

where the derivative is with respect to the longitudinal coordinate s, i.e. $x''(s) = d^2x/ds^2$ and where $k_z(s)$ is an arbitrary function that acts as a restoring force:

$$K_x(s) = \frac{1}{\rho(s)^2} + k_x(s) \tag{1.6}$$

$$K_y(s) = k_y(s) \tag{1.7}$$

A solution of the equations of motion can be written in a generic form as:

$$z(s) = C(s)z_o + S(s)z'_o \tag{1.8}$$

$$z'(s) = C'(s)z_o + S'(s)z'_o \tag{1.9}$$

C(s), *S(s)* and their derivatives with respect to s, *C'(s)* and *S'(s)*, describe the transformation of the coordinates at the position s_o, (z_o, z'_o) to the position s (z, z').

In accelerator physics, the coordinate transformation is often written by using transform matrixes M, which describes the change of particle coordinates.

Transformation matrix M is a right approach for accelerators, assuming that each magnet has constant magnetic field along the longitudinal direction, i.e., $\rho(s)$ and $k(s)$ are constants within

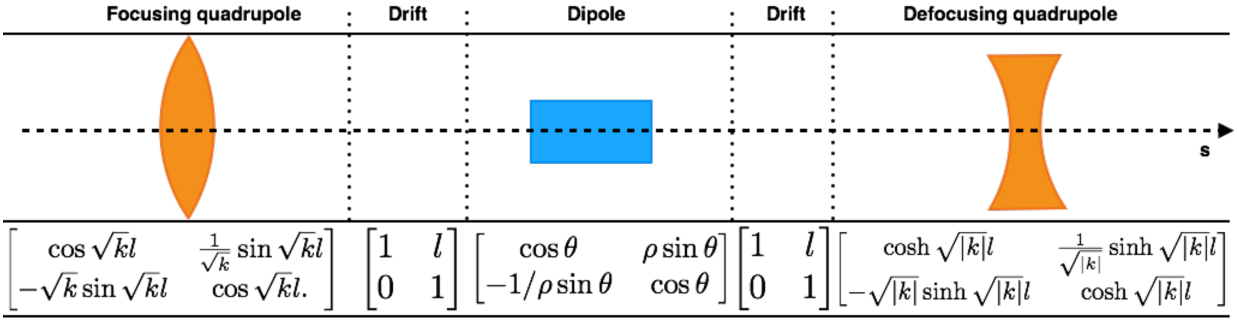

Figure 1.5: Summary of transformation matrixes associated to different elements.

the magnet length.

Figure 1.5 summarizes the transformation matrix of several magnetic elements, including; a dipole, a focusing quadrupole, a defocusing quadrupole and a drift.

In an accelerator, these elements are combined, and the transformation matrix is obtained by matrix multiplication, simplifying the particle tracking calculation. The transformation matrix for the series of elements becomes the product of the individual matrices.

A particular interesting lattice configuration is the FODO lattice used for focusing beams both in horizontal and vertical planes.

$$M_{FODO} = M_{focusing} \cdot M_{drift} \cdot M_{defocusing} \cdot M_{drift} \tag{1.10}$$

Another common combination of magnetic elements is the FBDB (focusing quadrupole-bending magnet-drift-bending magnet-focusing magnet), a FODO structure where the drift space is replaced, by a bending magnet.

In circular accelerators, other assumption that can be done is the periodicity in $\rho(s)$ and $k(s)$, i.e. $K_z(s) = K_z(s+P)$ and $\rho(s) = \rho(s+P)$. The equation of motion of a particle in a accelerator under the influence of periodic forces is called Hill's Equation and the solutions to this equation for horizontal and vertical plane are given by:

$$x = \sqrt{\epsilon_x\beta_x}\cos(\phi_x - \phi_{x,o}) \tag{1.11}$$
$$y = \sqrt{\epsilon_y\beta_y}\cos(\phi_y - \phi_{y,o}) \tag{1.12}$$

Where ϵ is the emittance of the beam, $\beta_{x,y}$ is the β function, which describes the variation of the oscillation envelope around the ring and $\phi_{x,y}$ is the betatron phase advance. The betatron function depends on the particular arrangement of quadrupole and dipole magnets and is illustrated in Fig. 1.6. Figure 1.6 also shows the trajectories envelope in a LHC region, given by $\sqrt{\beta\epsilon}$, as well as the closed orbit, particle trajectory and ideal orbit.

Analogously to the beta-function, the gamma-function, $\gamma(s)$, describes the envelope of oscillations in x' and y'. The γ and the α functions are defined as:

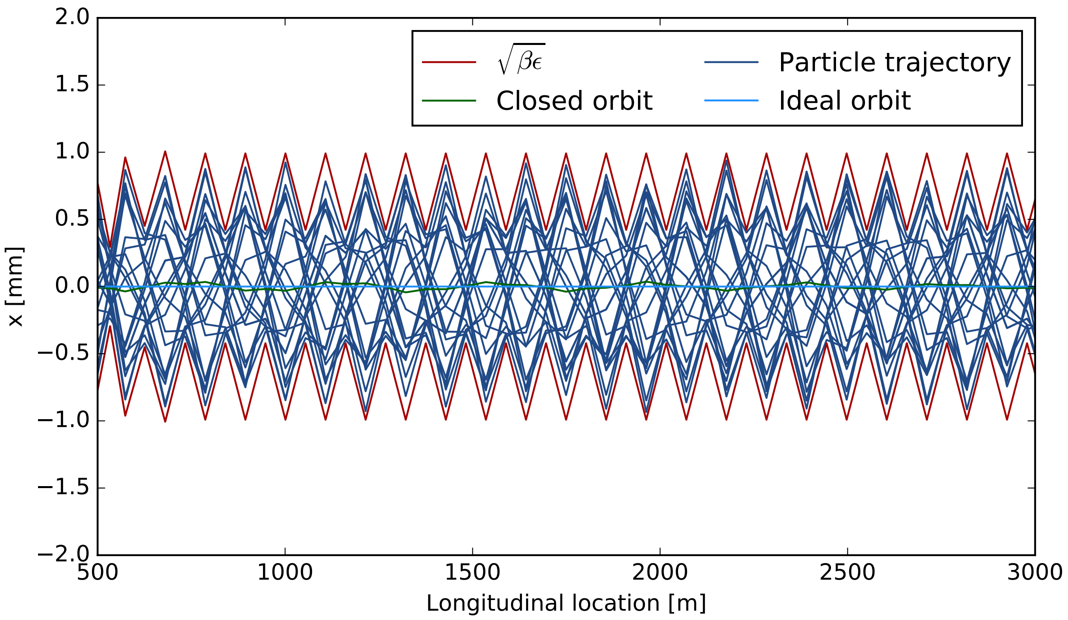

Figure 1.6: Tracking simulation in LHC Arc12 of a particle undergoing betatron oscillations.

$$\alpha_{x,y} = -\frac{1}{2}\frac{d\beta_{x,y}(s)}{ds} \tag{1.13}$$

$$\gamma_{x,y} = \frac{\alpha_{x,y}^2+1}{\beta_{x,y}} \tag{1.14}$$

Twiss parameters, $\alpha(s)$, $\beta(s)$ and $\gamma(s)$ at any position s can be obtained by knowing the transformation matrix and an initial set of values at the location s$_o$, E.g. in a drift, twiss parameters transform as:

$$\begin{bmatrix}\beta(s)\\ \alpha(s)\\ \gamma(s)\end{bmatrix} = \begin{bmatrix}1 & -2l & l^2\\ 0 & 1 & -l\\ 0 & 0 & 1\end{bmatrix} \cdot \begin{bmatrix}\beta(s_o)\\ \alpha(s_o)\\ \gamma(s_o)\end{bmatrix} \tag{1.15}$$

If this drift space of length L* -as the one shown in Fig. 1.7- is long enough, a convergent beam transform into a divergent beam while the angular envelop $x'_{max} = \sqrt{\epsilon\gamma}$ stays constant. The point ω where the beam reaches its minimum size (β^*) is determined by $\alpha(\omega)$, $\alpha(\omega) = 0$.

$$\beta(L) = \beta_o - 2L\alpha_o + L^2\gamma_o \tag{1.16}$$

It can also be described in terms of its minimum value β^* and its position ω as:

$$\beta(s) = \frac{(s-\omega)^2}{\beta^*} + \beta^* \tag{1.17}$$

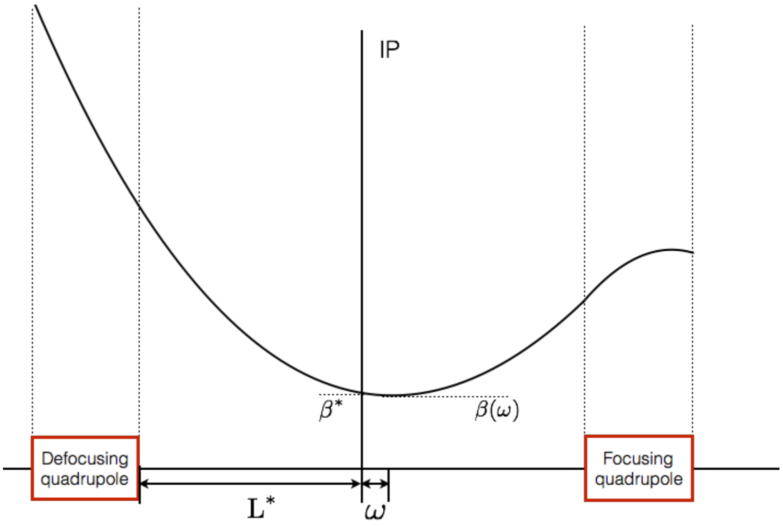

Figure 1.7: Schematic representation of a particle in a drift region placed between two quadrupoles: a focusing (left) and defocusing (right).

Real machines are not operated with single particles but with distributions composed by the order of 10^{11} particles per bunch. The distribution of that particle in phase-space defines an ellipse with area $\pi\epsilon$, being ϵ the beam emittance as seen in Fig 1.8. The equation of the phase space ellipse can be parameterized in terms of α, β,γ functions and the beam emittance, for an arbitrary plane z, can be written as:

$$\gamma_z z^2 + 2\alpha_z z z' + \beta_z z' = \epsilon. \tag{1.18}$$

On the other hand, a generic relation between the betatron phase advance and the β function is given by:

$$\phi(s) = \int_0^s \frac{dS}{\beta_s} + \phi_o. \tag{1.19}$$

It is possible to compute the number of betatron oscillations that the beam performs in one revolution by extending the integrals to the hole circumference. This quantity is known as tune as it is given by:

$$Q_{x,y} = \frac{1}{2\pi}\oint \frac{ds}{\beta(s)}. \tag{1.20}$$

1.2 Perturbations

Real dipolar and quadrupolar fields present deviations from the ideal field distribution that directly affect the beam dynamics. The existence of perturbations in the machine causes not only the tunes but also betatron functions to vary. The deviations of the β function for the ideal β value is called β-beating and have a frequency of twice the betatron frequency.

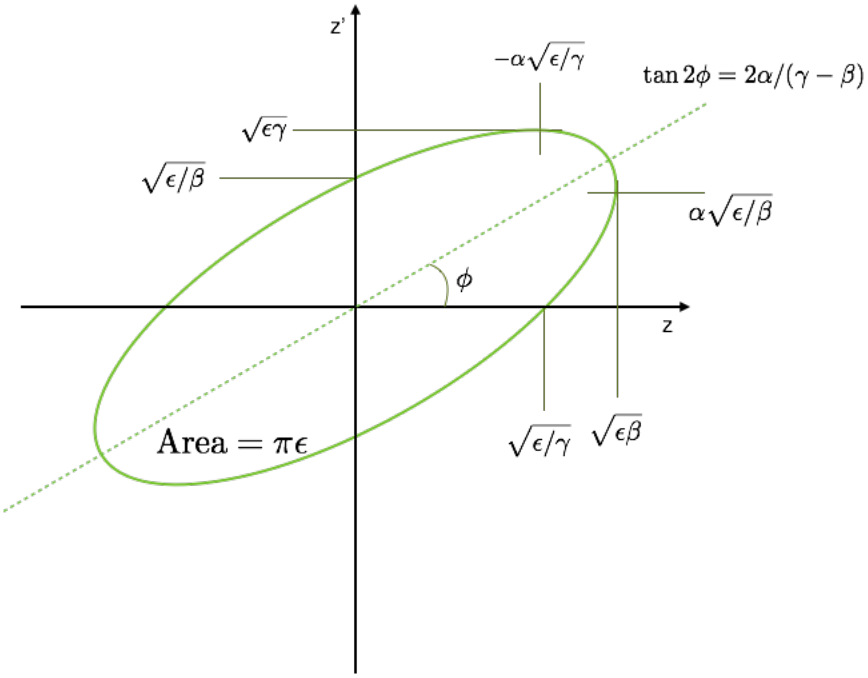

Figure 1.8: Phase space ellipse in the transverse z, z' plane. Where z represents either x or y.

Purely transverse magnetic fields can be described by:

$$B_y + iB_x = B_o \sum_{n=1}^{\infty} (b_n + ia_n)(x + iy)^{n-1} \tag{1.21}$$

where a_n refers to the skew multipole components and b_n refers to normal multipole components

$$a_n = \frac{1}{B_0(n-1)!} \frac{\partial^{(n-1)} B_x}{\partial \mathrm{x}^{n-1}} \quad b_n = \frac{1}{B_0(n-1)!} \frac{\partial^{(n-1)} B_y}{\partial \mathrm{x}^{n-1}} \tag{1.22}$$

where n corresponds to the order of the magnetic field, being n = 1 a dipole, n = 2 a quadrupole, n = 3 a sextupole, etc. If Eq. (1.21) is evaluated using Eq. (1.3), corresponding to the quadrupolar field, the only non-zero component is b_2. The a_2 component would become non-zero for 45° rotated quadrupoles as in this case the horizontal field depends additionally on the horizontal particle position. Due to imperfections of real magnets, higher-order multipoles occur in every accelerator and perturb the beam dynamics.

1.2.1 Dispersion

The curvature radius defined by the dipoles depends on the beam rigidity, as shown in Eq. (1.2). For a constant magnetic flux **B** particles with smaller momentum will present a larger curvature radius than the one with the ideal momentum, p_o. This deviation with respect to the ideal trajectory is defined by the Dispersion function, D(s), and its contribution to the particle orbit is given by:

$$\begin{aligned} x_{dispersion} &= D_x(s)\delta, \\ y_{dispersion} &= D_y(s)\delta, \end{aligned} \tag{1.23}$$

where $\delta = \frac{p-p_o}{p_o}$.

Moreover, under the presence of dispersive effects, the total orbit is given by:

$$x = x_{betatronic} + x_{closedorbit} + x_{dispersion}, \tag{1.24}$$

$$y = y_{betatronic} + y_{closedorbit} + y_{dispersion}, \tag{1.25}$$

1.2.2 Dipolar field perturbations

Dipole field errors also contribute to a change in the orbit, and their effect adds linearly to the dispersion function. The contribution of the dispersion perturbation to the orbit can be studied as a separate trajectory contribution due to the linearity of the equation of motion. The effect in the orbit at a position s of a given number of dipolar perturbations distributed across the accelerator is given by:

$$z(s) = \frac{\sqrt{\beta(s)}}{2\sin \pi \mathrm{Q}} \sum_k \sqrt{\beta_k}\theta_k \cos\left(\pi \mathrm{Q} - |\phi_s - \phi_k|\right) \tag{1.26}$$

where β_k and ϕ_k are the values of the β-function and phase-advance at the imperfection location respectively, and θ_k is the dipolar kick angle. The summation is over individual dipole error.

Primary sources of the dipole field errors are construction errors of the magnets, errors of magnets, power supplies, a tilt of the dipole magnets, and the feed-down effects of higher-order magnets.

1.2.3 Quadrupolar field perturbations

In a synchrotron, quadrupole field errors introduce deviations on the β-function due to fluctuations in the strength value, Δk. The effect of a thin gradient error can be described by the transformation M_p:

$$M_p(s_o) = \begin{bmatrix} 1 & 0 \\ -\Delta k & 1 \end{bmatrix} \tag{1.27}$$

where Δk $[m^{-1}]$ is the integrated gradient error at a given position s$_o$ This error will introduce β-beat given by the expression:

$$\Delta\beta(s) = \frac{\beta(s)\beta(s_o)}{2\sin(2\pi Q)}\Delta k(s_o)\cos(2|\phi_s - \phi_{s_o}| - 2\pi Q) \tag{1.28}$$

where $\beta(s_o)$ and $\phi(s_o)$ are the β function and the phase advance function at the position of the quadrupolar error and $\Delta\beta$ is the β-beating.

It is important to note that the term ($\sin 2\pi$Q) makes the β-beating diverge at the integer and half-integer resonances.

The sources of the quadrupole field errors are construction errors of the magnets, errors of magnets, power supplies, and the feed-down effects of higher-order magnets.

Higher order multipoles

Higher order magnets also affect the linear motion of the particle. When the closed-orbit passes of-centre through one of these magnetic elements, this can be reinterpreted as a combination of centred magnets of equal or lower order. For example, an offset in a sextupole generates a dipolar and a quadrupolar field.

1.2.4 Coupling

So far, the motion of the particles has been described separately for horizontal and vertical planes (x, x') and (y, y'). In a more realistic operational scenario, the motion in the horizontal and vertical plane are coupled. Skew-quadrupolar errors and solenoids the primary sources of the coupled motion.

In the presence of coupling in the machine, the motion can no longer be described by two independent 2x2 matrices. In this scenario, the transverse linear dynamics may be described by a 4x4 transfer matrix, M:

$$M = \begin{bmatrix} P & p \\ q & Q \end{bmatrix} \tag{1.29}$$

where P, p, Q, q are 2x2 matrices. If the motion is decoupled, then p and q vanish.

To first order, linear coupling drives two resonances (Q$_x$ + Q$_y$ = N) and (Q$_x$ - Q$_y$ = N). The magnitude of the transverse coupling is characterized by the coefficients C$^-$ and C$^+$ corresponding to the difference and sum resonances respectively.

1.2.5 Tune resonances

Equations (1.26) and (1.28) indicate that certain tune values need to be avoided. Beam will become unstable for the zeros of the denominator (($\sin \pi Q$) and ($\sin 2\pi Q$) respectively). Those conditions are fulfilled for $Q_{x,y} = n$ and $2Q_{x,y} = n$ with n $\in$ N.

In a more general case, further resonances can be excited if $m_1 Q_x + m_2 Q_y = n$ is fulfilled with (m_1,m_2, n) $\in$ N.

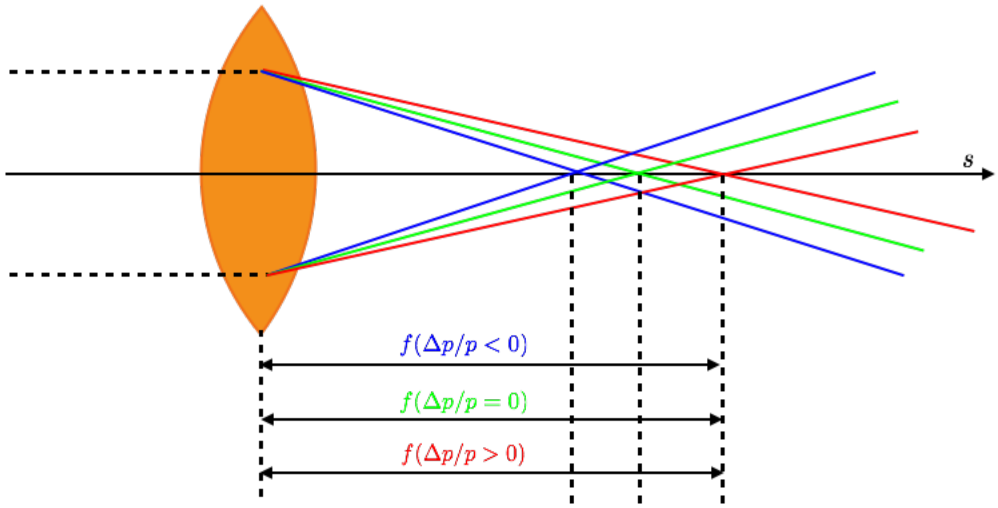

Figure 1.9: Chromatic aberrations induced by quadrupolar fields.

1.2.6 Chromatic effects

Chromaticity is defined as the change on the tune with the relative deviation from the ideal momentum. Figure 1.9 shows the variation of the focal length with the beam energy deviation with respect to the designed value.

$$Q_z\left(\frac{\Delta p}{p_o}\right) = Q_{zo} + Q_z^{'}\left(\frac{\Delta p}{p_o}\right) + \frac{1}{2!}Q_z^{''}\left(\frac{\Delta p}{p_o}\right)^2 + \frac{1}{3!}Q_z^{'''}\left(\frac{\Delta p}{p_o}\right)^3 + \ldots \tag{1.30}$$

where $Q^{'}$ is the first order variation of the tune with the relative momentum deviation, and is normally referred to as chromaticity. $Q^{''}$, $Q^{'''}$, and further higher order terms in the Taylor expansion are referred to as non-linear chromaticity.

The lowest order chromatic perturbation is caused by a combination of dipolar errors and the fluctuation of the focal length of the quadrupoles with energy. As in the case of geometric optics, the effective focal length is inversely proportional to the particle energy.

Chromaticity is corrected by adding a sextupolar magnetic element that compensates the effect of the quadrupole. These elements apply different focusing corrections depending on the energy of the particle, as shown in Fig. 1.10.

1.2.7 Luminosity

For particle physicists, one of the most important parameters is the interaction rate, i.e., the number of collisions that occur every time counter-rotating beams collide. The extremely low probability of finding a new high energy physics (HEP) phenomena after a beam collision, leads to a higher collision rate to increase the available statistics. The interaction rate is related to two parameters, the beam sizes (σ_x, σ_y) and the luminosity $\mathcal{L}$. Luminosity describes the probability that a collision between two particles, travelling in opposite directions, occur every time beams collide in the IRs [28]. A simplified equation for luminosity neglecting crossing angle and hourglass effects [26] is given by Eq. 1.31:

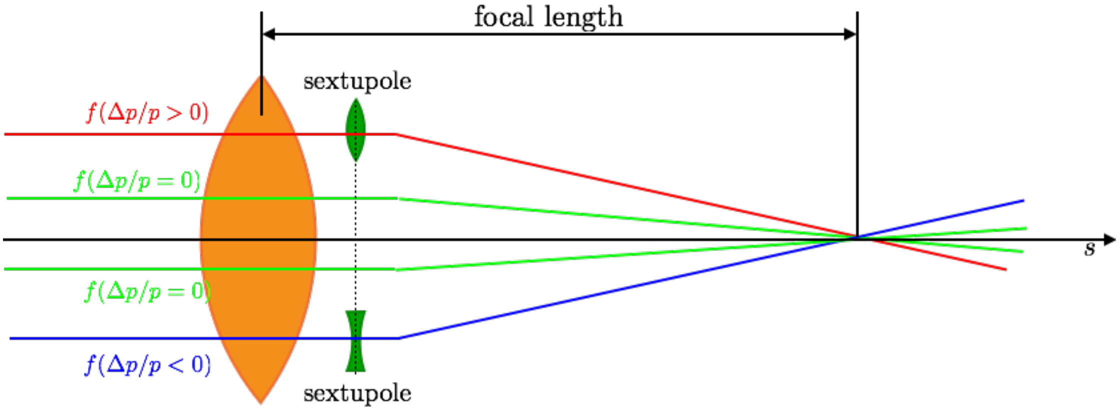

Figure 1.10: Correction of chromatic aberrations using sextupoles.

$$\mathcal{L} = \frac{1}{4\pi}\frac{N_1 N_2 f N_b}{\sigma_x \sigma_y} \tag{1.31}$$

where N_1 and N_2 are the number of particles per bunch and N_b are the number of bunches of the machine, f the revolution frequency and σ_x, σ_y and are the transverse beam dimensions. The luminosity is also the performance figure of merit used in colliders.

1.3 Optics measurements and corrections

Accurate measurements of optics functions- β, α, D- are essential for proper operation of a synchrotron both for machine protection and for the performance. β functions can be obtained from different observables: phase and amplitude of the transverse betatron oscillations and change of the tune by modulating the current of quadrupoles (K-modulation). Reconstruction of β function using the phase, in combination with K-modulation, have been the main approaches for obtaining the β function in the LHC. Nonetheless, challenges have appeared in the β calculation using these two approaches when aiming for smaller β^* in the LHC and the HL-LHC. The third β measurement technique, based on the amplitude [8], has not been used as widely in the LHC as the other methods since it requires accurate BPM gain calibration.

1.3.1 Optics measurements

Linear optics measurements and corrections are key elements in the operation of present and future colliders such as LHC [8, 30, 31, 32], its upgrades HL-LHC [33], HE-LHC [34] or the FCC [35, 36] and electron ligth sources [3, 6]. In the case of colliders, an increase in luminosity requirements moves the LHC into more challenging operational regimes with lower β^*. In LHC strong localized magnetic errors have to be corrected in order to achieve the design value of the β function at the interaction point (IP) to provide the designed luminosity within the 5% tolerance limits to the main experiments: ATLAS [37], ALICE [38], CMS [39] and LHCb [40]. These corrections are based on the analysis of turn-by-turn measurements from the beam position monitors (BPMs) [41, 42, 43, 44] and K-modulation [5, 7, 45, 46].

Excitation	**Observable**	**Analysis**	**Parameters**	**Limitations**
Betatron oscillations	Centroid position	FT SVD cleaning	ϕ ϕ, β^{ϕ}, β^{A}	ϕ values BPM calibration
Quadrupole gradient	Tune Fit	Fit	Average β at the quadrupole	Tune accuracy
Orbit measurements	Orbit	Fit parameters to the designed model		Model dependency

Table 1.1: Summary of the optics measurements techniques.

Different techniques can be used in order to measure optics functions in particle accelerators, depending on the magnets power supply configuration, their size and their instrumentation [47]. Table 1.1 summarizes some of the most common techniques used for Optics measurements.

Turn-by-turn measurements

Turn-by-turn (TbT) optics measurements are based on measuring betatron motion using the transverse beam centre of charge position for many consecutive turns at every beam position monitors BPMs. In order to perform betatron measurements, the beam is excited in the horizontal and vertical plane, displacing the beam centre of charge in phase space inducing betatron oscillations that can be recorded by the BPMs. Either external excitation can be performed one time per cycle, or it can be applied periodically within the same cycle. The latter has the advantage of adiabatically increasing and decreasing the excitation amplitude, which prevents to increase the beam emittance [48].

TbT data is then processed using single-value-decomposition techniques (SVD) in order to decrease the signal noise and then, is transformed into the frequency domain using advanced algorithms [49]. To clean TbT data, the data is converted into a matrix M with spatial information m row corresponding to the number of BPMs and n columns corresponding to the number of turns. This matrix is decomposed into U and V, describing the spatial and temporal modes respectively, and a matrix Σ. Σ is an m $\times$ n diagonal matrix of real positive elements, which are the singular values of M. Modes with small singular values, result of uncorrelated noise between the BPMs, are removed from the matrix. Turn-by-turn data is again reconstructed by multiplying the matrix U, Σ- after being filtered- and V.

Information contained in the frequency spectra, both phase and amplitude, is used for optics functions reconstruction around the ring. On the one hand, relative phase advances between a reference BPM and at least two other BPMs allow reconstructing the values of the β functions at the BPMs. This method, known as β from phase (β^{ϕ}), was first used in LEP [1] and has been further developed in LHC, ALBA and ESRF [2, 3, 4, 6]. On the other hand, the amplitude of the transverse motion at a given position is proportional to $\sqrt{\beta}$. β-function reconstruction approach, based on amplitude measurements, is known as β from amplitude (β^{A}). Nonetheless, this β-function reconstruction technique is biased by the calibration error of each BPM. The β from amplitude approach has been used in the past [1, 6, 50, 51], it is currently implemented as part of the OMC software [43], but it has not been as widely used as β^{ϕ} or $\beta^{\text{K-modulation}}$.

The main advantage of the TbT measurements is the speed, since the beam excitation combined

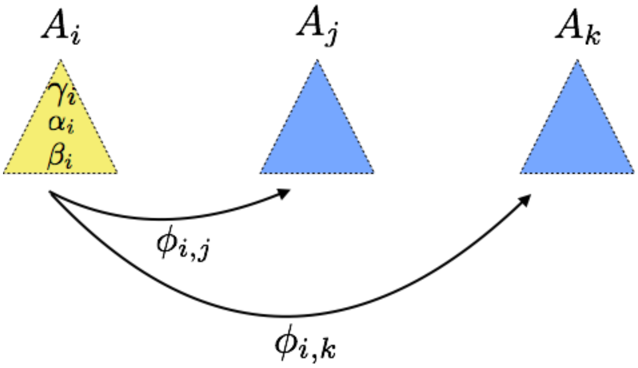

Figure 1.11: Schematic of β^{ϕ} and β^{A} reconstruction.

with data recording, takes only a few seconds for all the BPMs.

Equation 1.12 relates the amplitude of the transverse motion to the beam action $2J_{x,y}$ and $\beta_{x,y}$, and by combining the phase advance $\phi_{x,y}$ in different accelerator locations, it is possible to reconstruct both the β-function, α-function and γ-function.

Both phase and amplitude of the betatron oscillation can be derived by this harmonic analysis at every BPM position [6, 52]. Figure 1.11 shows a schematic of the reconstruction of optics functions based on the amplitude and phase of TbT data. On the one hand, relative phase advances between a probe BPM i at the location where the β-function is being calculated and two other BPMs, j and k. Using this approach, β function is obtained using:

$$\beta_i = \frac{\epsilon_{ijk} \cot \phi_{i,j} + \epsilon_{ikj} \cot \phi_{i,k}}{\epsilon_{ijk} \frac{M11(i,j)}{M12(i,j)} + \epsilon_{ikj} \frac{M11(i,k)}{M12(i,k)}} \tag{1.32}$$

where $\phi_{i,j}$ and $\phi_{i,j}$ is the phase advance between BPMs, ϵ_{ijk} is the Levi-Civita symbol and $Mmn(i,k)$ are the elements of model transfer matrix between the locations i and j. In [2] it has been proved that the measurement of the phase, $\phi_{i,j}$ and $\phi_{j,k}$, is not affected by an offset of the beam or a wrong excitation amplitude due to BPM calibration errors. The accuracy of the β^{ϕ} calculation depends on the value of the phase advance between a pair of BPMs. β^{ϕ} approach reaches its limitation for values of ϕ in the vicinity of $n\pi$ as the cotangent becomes infinite at those points. β^{ϕ} also presents limitations in the performance when $\phi_{i,j} = \phi_{i,k}$ [2].

One example of this limitation can be found in colliders where the β-function at the interaction points reach minimal values, i.e., $\beta^* < 40$ cm. In those scenarios, the amplitude of the transverse oscillations recorded in the BPMs closest to the IP increases as the β^* decreases, but phase advance between neighbour BPMs drops to small values. β^{ϕ} approach is very sensitive to errors for values of the BPMs phase advance close to nπ.

On the other hand, the amplitude of the transverse motion at a given position is proportional to$\sqrt{\beta}$, and this can be used for β measurements. The amplitude, A_i, can also be expressed in terms of the β-function, β_i, and a common observable for all BPMs, the driven action, *2J*,

$$A_{\mathrm{i}} = \sqrt{2J\beta_{\mathrm{i}}}. \tag{1.33}$$

So, therefore, the β^{A} can be obtained using:

$$\beta_i^A = \frac{A_i^2}{2J} \tag{1.34}$$

Where the action is being computed as the average over all the BPMs of the ratio of the amplitude at a given BPM and the β function at that position:

$$2J = \left\langle \frac{A^2}{\beta} \right\rangle \tag{1.35}$$

Nonetheless, the reconstruction of the β function using the amplitude is biased by the calibration error of each BPM. In [53] it has been proven that the BPM calibration is independent of the amplitude oscillations; therefore β^{A} approach does not presents further limitations in very-low β^* scenarios. This method can additionally be used also in the scenarios where the phase advance is constant around the accelerator $\phi_{i,j}$.

Knowledge of BPM calibration factors would allow to accurately measure β function in different machine operational scenarios where the performance of other approaches is limited. A more detailed study of the effects of the BPM calibration factors in the β function calculation is derived in Chapter 4.

A first attempt of measuring calibration factors was performed in [54]. Later in 2015 [55], a special LHC optics was studied in order to calculate the calibration of a set of LHC BPMs. This technique is summarized in Chapter 4 and has been further developed in 2016, 2017 and 2018. Another calibration technique has been developed as part of this thesis for measuring the calibration factors of the PSB BPMs. The methodology used to obtain the PSB calibration factors is summarized in Chapter 6.

K-modulation

K-modulation allows to obtain the value of the average β ($\beta^{\text{K-modulation}}$) at the quadrupoles placed closest to the interaction points (IPs). The suitability of this method for future accelerators has been studied in HL-LHC, FCC and SuperKEKB [7, 45, 46] where it has been found that foreseen tune stability might not be sufficient for the good performance of this approach.

K-modulation approach is based on the analysis of the tune change induced by a current modulation in individually powered quadrupoles that are generally the ones located left and right to the IP. The relation between these two observables allows obtaining the β function at the quadrupolar location [56]. The accuracy of this method depends on the power supplies control and natural tune stability . Accuracy of the β^* measurement for LHC and High Luminosity LHC using K-modulation has been previously studied in [45]. The study concludes that accuracy on the tune measurement of about 10^{-5} is crucial in order to control the β^* within the tolerance constraints given by the luminosity. Analysis of the tune stability [57] performed during the second run of the LHC shows that the tune jitter ranges between $2 \cdot 10^{-5}$ and 10^{-4} depending on the optics being analyzed. K-modulation is planned to be widely used both in future runs of LHC and in next-generation colliders [7].

1.3.2 Optics corrections

Optics corrections are a key element for the optimal operational in accelerators. Optics corrections can be divided into two groups according to the range of quadrupoles involved. Global corrections cover the most significant part of the accelerator while local corrections are focused on very strong and localized errors.

Global corrections

Global corrections are computed using a response matrix method. This response matrix, $\overrightarrow{R}$-matrix, relates the difference of the measured $\phi_{x,y}$, $\beta_{x,y}$, normalized horizontal dispersion [58], and tunes with respect to the MADX-model, to the strength of all quadrupoles circuits:

$$(\Delta\overrightarrow{\phi_x}, \Delta\overrightarrow{\phi_y}, \frac{\overrightarrow{\Delta\beta_x}}{\beta_x}, \frac{\overrightarrow{\Delta\beta_y}}{\beta_y}, \frac{\overrightarrow{\Delta D_x}}{\sqrt{\beta_x}}, \Delta Q_x, \Delta Q_y) = \overrightarrow{R}\Delta k \tag{1.36}$$

The required strength Δk is computed from the measured optics errors:

$$\Delta k = -\overrightarrow{R}(w_1\Delta\overrightarrow{\phi_x}, w_2\Delta\overrightarrow{\phi_y}, w_3\frac{\overrightarrow{\Delta\beta_x}}{\beta_x}, w_4\frac{\overrightarrow{\Delta\beta_y}}{\beta_y}, w_5\frac{\overrightarrow{\Delta D_x}}{\sqrt{\beta_x}}, w_6\Delta Q_x, w_6\Delta Q_y) \tag{1.37}$$

where w_i stands for the weights applied to correct the individual optical functions.

Skew quadrupolar corrections are used to correct coupling presented in the machine. In the case of correction using skew quadrupoles, the R-matrix relates the difference and sum resonance, and the vertical dispersion to the strength of all skew quadrupoles circuits. The required strength is computed from the measurement error with respect to the MADX-model:

$$\Delta\overrightarrow{k_s} = (w_1\Delta\,\mathrm{Re}\,\overrightarrow{f}_{1001}, w_2\Delta\,\mathrm{Im}\,\overrightarrow{f}_{1001}, w_3\Delta\,\mathrm{Re}\,\overrightarrow{f}_{1010}, w_4\Delta\,\mathrm{Im}\,\overrightarrow{f}_{1010}, w_5\Delta D_y) \tag{1.38}$$

where w_i stands for the weights applied to correct the coupling and vertical dispersion.

Local corrections

The segment-by-segment (SbS) technique was developed at the LHC for the computation of optics corrections for local, strong error sources. This method consists of modelling the optics in a part of the accelerator in between two BPM locations. Phase advance, β and α functions measured at the BPM locations are used as boundary conditions for solving Hill equation 1.5 using MADx [41, 42, 59]. The optics modelling tool in MADX aims to reproduce the behaviour of the measured functions in the segment by changing the strength of the quadrupoles located inside the segment.

Segment-by-segment technique has also been used for computing the optics functions in different machine locations, such as the interaction points, the wire scanners and collimators.

Chapter 2

The LHC complex

The Large Hadron Collider (LHC) complex is a chain of accelerators that allows accelerating particles in different steps from the source to the Large Hadron Collider (LHC), Fig. 2.1. Acceleration in different steps allows having very intense beams optimizing the collective effects that are dominant at the range of low energies [60]. LINAC4 (2018) [32] injects H^- ions with a energy of 160 MeV. Proton Synchroton Booster (PSB, 1972) [61] accelerate protons to an energy of 2 GeV and inject the beam in the proton synchrotron (PS, 1959) where the beam is accelerated to 26 GeV. The last step in the accelerator chain is the super proton synchrotron (PS, 1976), that accelerate the beam to 450 GeV just before the injection in the LHC [30, 31, 32].

2.1 The Large Hadron Collider

The Large Hadron Collider (LHC) is a 26.66 km twin ring synchrotron collider operated by the CERN laboratory. Two counter rotating hadron beams are circulated in the accelerator, and collide at four interaction points (IPs), to provide data for High Energy Physics (HEP) experimental apparatus: ATLAS [37], LHCf [62], Alice [38], CMS [39], TOTEM [63], LHCb [40], and MoEDAL [64]. The LHC can be divided into eight octants and consists of eight bending sections, the arcs, which are separated by eight straight sections. The straight sections also referred to as insertion regions (IRs), serve a specific purpose such as housing an experimental detector, beam acceleration, beam collimation and beam extraction. LHC consists of two beams, called Beam 1 and Beam 2 circulating in opposite directions in separate beam pipes in the arcs and is a common one in the IRs where they collide. Figure 2.2 shows the LHC lattice with the names and missions of the different arcs and IRs. The LHC machine is described in the LHC design report while the rest of the injectors are described in the LHC Injectors design report. LHC lattice, including the ARCS and the Insertion regions, are fully described in [30].

2.1.1 Operational cycle of LHC

The operational cycle of LHC has been slightly modified during the second run of the LHC. Before the beam is injected, the LHC magnets are pre-cycled in order to ensure the reproducibility of the magnetic fields. Once the set-up process is finished, the beam is injected from SPS at an

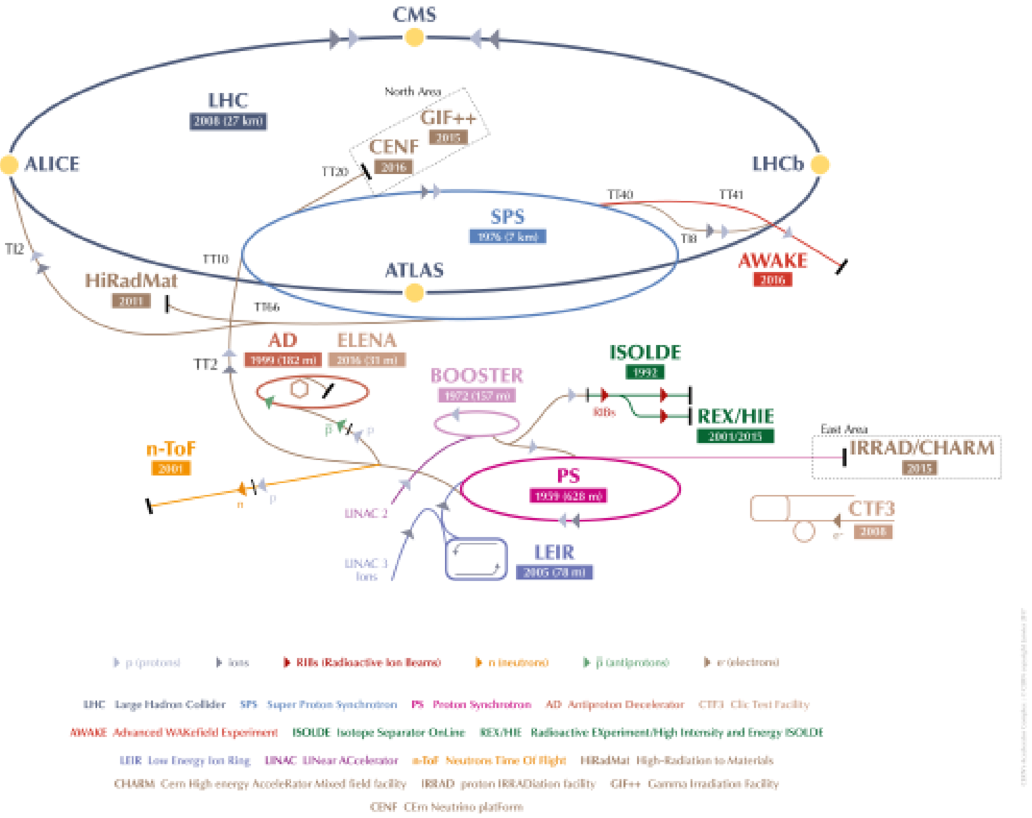

Figure 2.1: Schematic of LHC accelerator chain.

energy of 450 GeV. The number of bunches injected depends on the physics studies, fluctuating from 1 from machine studies to 2048 for runs dedicated to high energy physics. Once all the bunches are injected in the LHC, the dipoles start ramp-up until they reach the maximum magnetic field. The next step after reaching maximum energy (Flattop) is to decrease the β at the interaction points, β^*. At the beginning of the second run of the LHC (2015), the squeeze process started at the end of the ramp. Since 2017, this process starts at the beginning of the ramp [65].

Figure 2.3 shows an schematic of the LHC cycle.

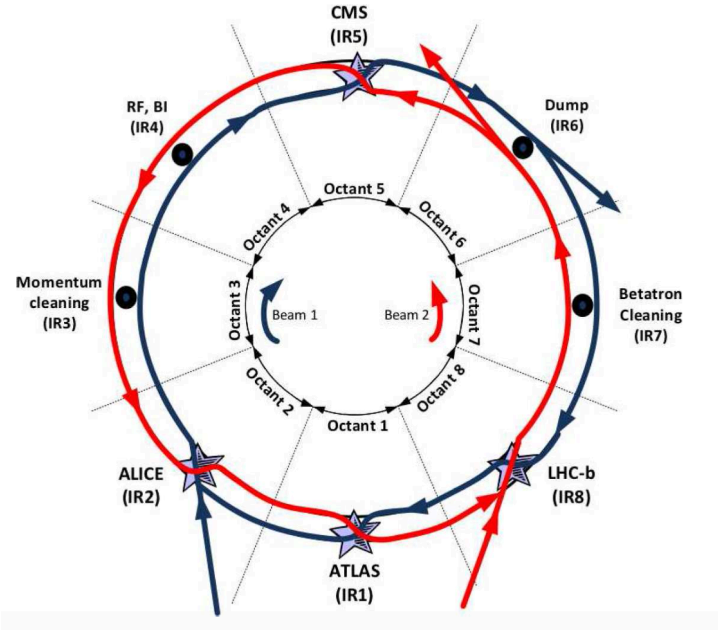

Figure 2.2: Layout of the LHC illustrating the eight octants. In each octant, the purpose of its IR is shown. The crossing of beam 1 (blue) and beam 2 (red) is indicated in the four experimental insertions.

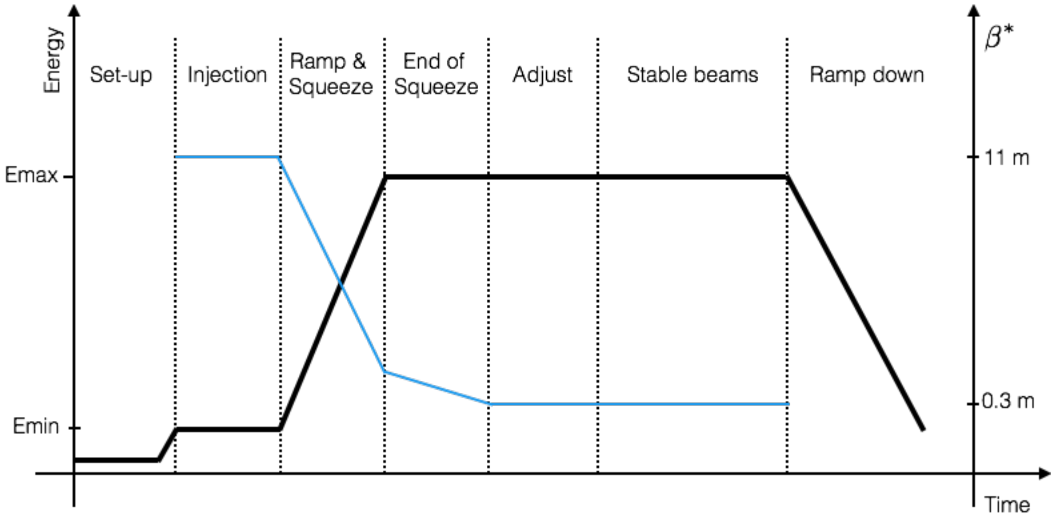

Figure 2.3: Schematic of the LHC cycle, including the energy and β^* as a function of time.

2.2 Protron Synchrotron Booster

PSB is a low energy accelerator made of 4 rings stacked on top of each other, allowing to reduce the space charge related effects [66]. PSB serves not only as PS injector but also delivers beams to the ISOLDE [67] experiment directly.

PSB was built in 1972 and currently is performing far beyond its original design specifications. Many improvements have been made throughout the years, allowing the machine to reach higher and higher intensities, and it now operates at about four times the design intensity. HL-LHC

[33] will require the intensity to be increased by a further factor of two while maintaining small beam size and keeping levels of beam loss low. In the frame of the LIU project, its injection energy will increase from 50 MeV to 160 MeV, which together with the new H^- injection will allow providing a higher intensity to PSB. PSB is expected to double the brightness with Linac4 and 160 MeV injection [61, 55, 68]. All proton beams for the PS are currently ejected at 1.4 GeV, that will be upgraded to 2 GeV in the third run of LHC [69].

The PSB has a circumference of 157 meters and is composed of sixteen nearly identical periods. The lattice structure is made up of separate bending magnets and focusing magnets, each period of the lattice contains two bending magnets and a triplet of focusing magnets in an F-D-F configuration. An overview of the PSB lattice is summarized in Figs. 2.4 and 2.5.

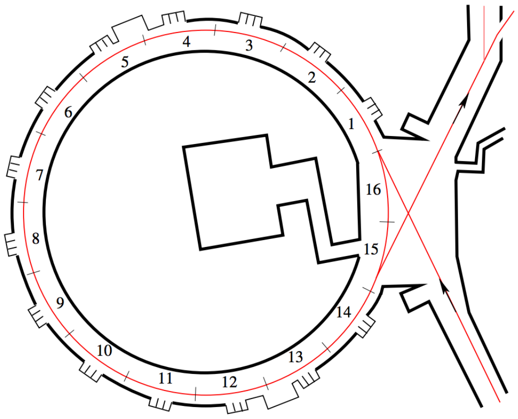

Figure 2.4: Schematic of PSB lattice.

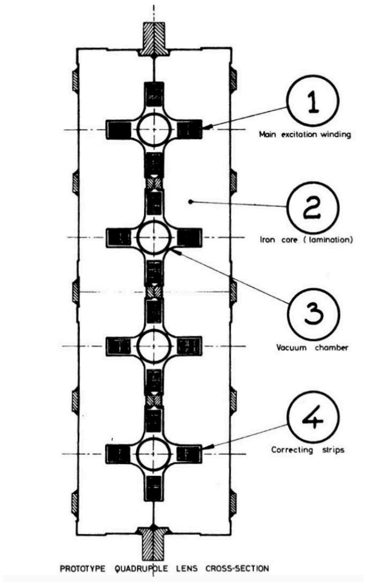

Figure 2.5: Drawing of a prototype for the focusing magnets in the CERN PSB. Image from [14].

PSB operates in a supercycle mode composed of several cycles that are repeated periodically. In each cycle, the beam is injected, ramped up and extracted. Each PSB cycle depends on whether the beam is delivered to PS, to ISOLDE or it is being used in order to perform beam dynamics studies. In case the beam is injected to ISOLDE or to PS the extraction is 1.4 GeV (2 GeV after the LIU upgrade), a more detailed overview of LHC beams in PSB can be found in [70]. For the optics measurements performed during this thesis, a specific cycle was created with a maximum energy of 160 MeV, Fig. 2.6. The main goal of this cycle is to have a plateau of constant energy sufficiently long to perform optics measurements.

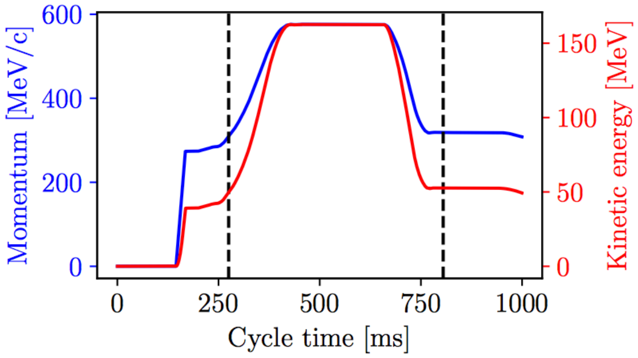

Figure 2.6: Schematic of the 160 MeV cycle used for the beam dynamics studies at PSB. Image from [15].

2.3 Instrumentation

Special instrumentation is required during optics measurements and corrections. This section summarises the instrumentation required for the performance of optics measurements both in LHC and PSB.

The section is divided into beam instrumentation (passive elements) that allows us to measure different beam properties and measurement instruments (active elements) that allow us to excite the beam.

2.4 Beam instrumentation

2.4.1 Beam Position Monitors

Beam position monitors (BPMs), or pick-ups, are one of the critical instrumentation elements in the operation of an accelerator. Electromagnetic pick-ups serve as a non-destructive diagnostic device for measuring the centre of charge of the beam. For each plane, two electrodes are placed face to face forming a monitor [71, 72, 73].

The operating principle of signal extraction can be either based on capacitive coupling (electric field) or based inductive coupling (magnetic field). This introduction is focused on capacitive coupling pick-ups since it is the one used in the LHC accelerator complex. In a capacitive-coupling based BPM, the position is obtained by measuring the difference voltage induced in the walls of the pick-up of opposite plates (horizontal and vertical). Voltage is then normalised by adding the voltage induced in both electrodes, in order to have a reading independent of the beam intensity. This method for obtaining the beam position, known as "difference over sum", reduces the non-linear effects that appear for large beam-offset.

The transformation from voltage to a position in the linear approximation is given by:

$$\mathrm{x} = \mathrm{S}_{\mathrm{horizontal}} \frac{\Delta U_{\mathrm{horizontal}}}{\Sigma U_{\mathrm{horizontal}}} + E \tag{2.1}$$

$$\mathrm{y} = \mathrm{S}_{\mathrm{vertical}} \frac{\Delta U_{\mathrm{vertical}}}{\Sigma U_{\mathrm{vertical}}} + E \tag{2.2}$$

where S is a scaling factor derived from the BPM geometry and the properties of its analogue signal conditioning electronics, E is an error correction accounting for mechanical misalignment and electrical offsets, ΔU is the voltage difference induced in opposite electrodes and ΣU the voltage sum.

Different BPM geometries are used for different beam conditions. The two most widely used BPMs at LHC and its injectors are:

1. **Button BPMs.** This kind of pick-ups, illustrated in Fig. 2.7 are the most common BPMs at LHC. They are placed in the arcs where only one beam circulates in the pipe and measure the beam position with a resolution that depends on beam intensity. In the case of LHC, the maximum resolution is 50 μm while in case of PSB maximum resolution is 30 μm.
2. **Stripline BPMs.** . This kind of pick-ups (illustrated in Fig. 2.8) are needed in case the travelling direction of the beam also has to be measured.

Beam position monitors operate in two different modes depending on the measurement integration time. If the BPM read-out is synchronised with the revolution frequency of the beam, then the BPMS works in turn-by-turn or trajectory mode [74]. Otherwise, if the position is averaged over a certain amount of time, then the BPM operates in trajectory mode. Operating in trajectory mode is exceptionally challenging for analogue electronics. The limitation factor, in terms of speed, are the analogue to digital converter that gets the beam position from the BPMs [75].

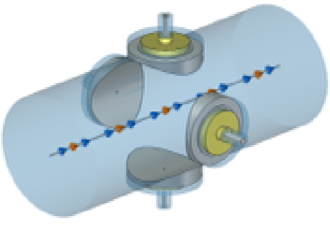

Figure 2.7: LHC Button BPM.

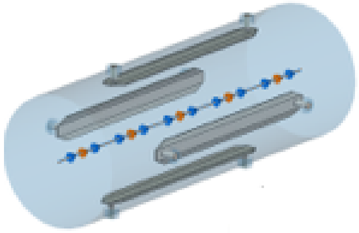

Figure 2.8: LHC Stripline BPM.

2.4.2 Base Band Tune (BBQ)

Continuous, passive monitoring of tune and linear coupling in the LHC is provided by the Base Band Tune (BBQ) system [76, 77]. BBQ is also used in PSB for continuous monitoring of the tune. The traditional BBQ is based on the independent filtering of the signal recorded by the opposite BPMs plates. By filtering the data, using analogue RC circuits, it is possible to keep the signal frequencies associated with the betatron motion. An improved version of this principle uses diodes in the filtering process [78, 79]. The signal recorded by each of the electrodes is directly converted into a saw waveform by a combination of a diode and an RC circuit, as shown in Fig. (2.9). The resulting signal conserves the betatron modulations. A DC filter removes the DC component of the signal, related to the beam amplitude. The two output, coming from the opposite electrodes, signals are there used as an input of a differential amplifier in charge of removing the signal component associated with the average beam position. Finally, the output signal is filtered to attenuate the revolution frequency and its harmonics. The component of the signal related to the beam amplitude is filtered with the help of a DC-filter.

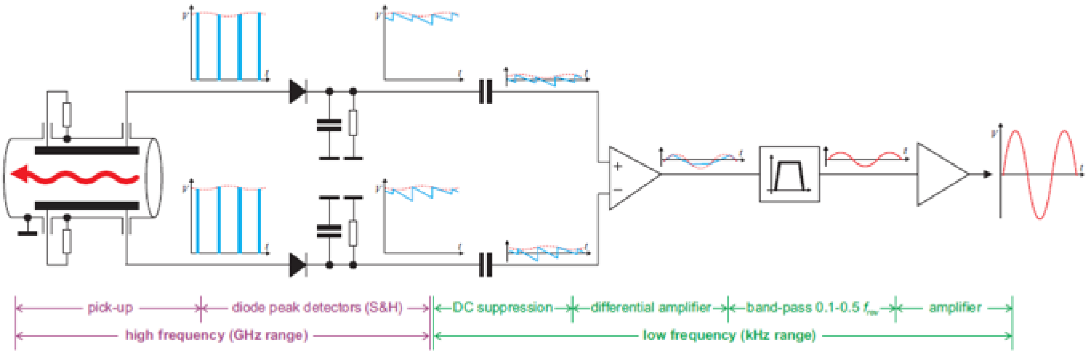

Figure 2.9: Working principle of BBQ measurements

The dedicated BPMs implemented used for the continuous tune monitoring are located in IR4 in case the LHC and section 3L1 (next to the BR.QNO3L1) in the case of PSB. A sample of the signal recorded by the BBQ is shown in Fig. (2.10) for LHC and in Fig. (2.11) for PSB.

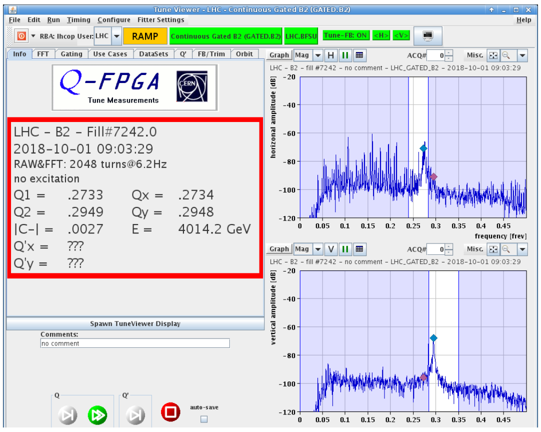

LHC - B2 - Fill#7242.0
2018-10-01 09:03:29
RAW&FFT: 2048 turns@6.2Hz
no excitation
Q1 = .2733 Qx = .2734
Q2 = .2949 Qy = .2948
|C-| = .0027 E = 4014.2 GeV
Q'x = ???
Q'y = ???

LHC - B2 - fill #7242 - no comment - LHC_GATED_B2 - 2018-10-01 09:03:29

LHC - B2 - fill #7242 - no comment - LHC_GATED_B2 - 2018-10-01 09:03:29

Comments: no comment

Figure 2.10: LHC BBQ Measurements.

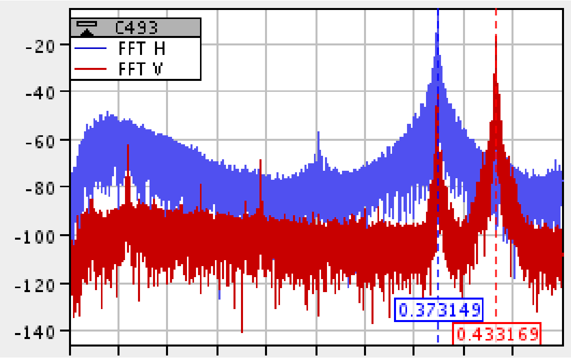

Figure 2.11: PSB BBQ measurements

Figure 2.12: Spectra recorded by the BBQ for LHC and PSB.

2.4.3 Beam Loss Monitors

Beam loss monitors (BLM) are one of the critical systems for machine protection due to the high energy stored in the beams travelling around the accelerator. The energy stored in the nominal LHC beams is 362 MJ/beam. At 7 TeV, a deposited energy density of 1 mJ/cm^3 could quench a magnet or could cause magnet damage. BLMs are also crucial elements while performing optics measurements and are used continuously during the accelerator operation [80, 81].

BLM consists of ionisation chambers, located outside the beam chamber, as shown in Fig. 2.14. BLMs measure the energy deposition of secondary showers of particles generated by particles losses inside the vacuum chamber. This measurement allows estimating the amount of beam that has been lost while performing the excitation.

The losses are integrated with 12-time intervals ranging from 40 μs to 84 s and compared to threshold values defined in 32 energy ranges (Fig. (2.13)). Radiation tolerances changes within the accelerator, from one component to other depending on the specifications.

If the BLM detects a certain level of radiation (a trigger), the beam is dumped to prevent damages in the machine. The beam dumps are the only places to dispose of the beam safely.

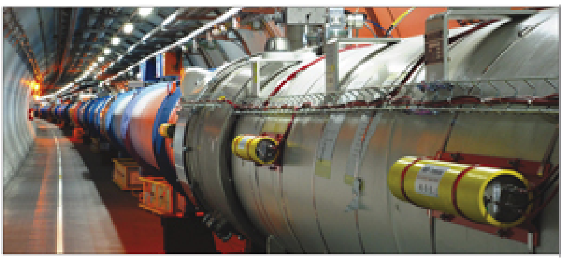

Figure 2.13: LHC BLM.

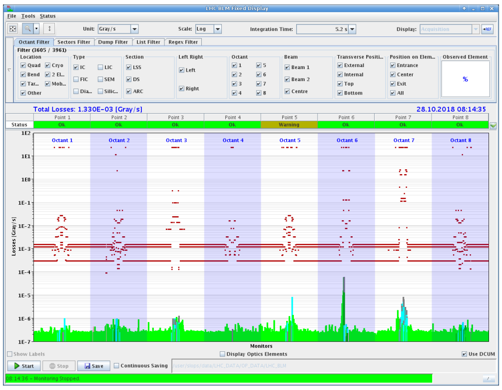

LHC BLM Fixed Display

Unit: Gray/s
Scale: Log
Integration Time: 5.2 s
Display: Acquisition

Filter (3605 / 3961)

Total Losses: 1.330E-03 [Gray/s]
28.10.2018 08:14:35

	Point 1	Point 2	Point 3	Point 4	Point 5	Point 6	Point 7	Point 8
Status	Ok	Ok	Ok	Ok	Warning	Ok	Ok	Ok

/user/slops/data/LHC_DATA/OP_DATA/LHC_BLM

08:14:36 - Monitoring Stopped.

Figure 2.14: Radiation recorded by Beam Losses Monitors.

2.4.4 Beam current monitors

Beam intensity is continuously monitored during the performance of the optics measurements, and it has great importance, especially while using the AC-dipole as an external excitation source. Specific configurations of the AC-dipole- driven voltage set too high or if the driven frequency is too close to the beam tune - could lead to beam losses.

Beam current monitors are one possible instrument for measuring the beam intensity (BCT) [82]. The principle is based on a transformer where the beam acts as the primary winding (1 turn) and the BCT as a secondary (n turns).

2.4.5 Emittance measurements

Measuring the emittance of the beam is a key element both for LHC and for PSB [17, 83]. In the case of the LHC, emittance is required for measuring and control the luminosity delivered to the experiments. In case of PSB, the primary motivations for measuring the emittance are: to identify sources of blow-up along the cycle, study the current limitations of the beam instrumentation and validate different measurements and data analysis methods.

2.4.6 Roman pots

The Roman Pot is an experimental technique introduced at the Intersecting Storage Ring (ISR) for the detection of forward protons from elastic or diffractive scattering [84]. It has been successfully employed in other machines like the SPS, TEVATRON, RHIC and DESY. Roman pots are placed both in the horizontal plane and in the vertical plane. The vertical pots are needed for the total cross-section measurement and the elastics scattering, while the horizontal one is a complement to study the diffractive physics. The detectors in the horizontal pot overlap with the two vertical detectors, helping in the alignment with tracks.

2.5 Measurements Instruments

2.5.1 Experimental kickers

The experimental kickers apply a transverse momentum kick that displaces the beam to larger amplitudes in phase space. This kick induces larger transverse oscillations that can be recorded by the BPMs.

Different elements can be used as external kickers. One possible option is normal conducting dipoles formed from a single turn solid copper that can provide swift response kicks. This kind of excitation is used both in LHC and PSB. In the case of LHC, kickers are located in IR4 while in PSB they are placed in 12L1.

In the case of the PSB, a new excitation system has been used, the transverse feedback [85, 86]. In regular operation, the main goal of the transverse feedback is to correct possible beam instabilities. Nonetheless, it can also be used to kick the beam periodically. The system consists of a BPM that it is in charge of measuring the position of the beam, a feedback loop that compares the position measured to a reference value and a deflector consisted in four 50 Ω stripline electrodes opposed in each plane. The pick-up signal and the feedback loop have to be disconnected from the deflector. In replacement, a function generator is added to the system to control the deflector. The same configuration can be implemented using the dipolar kicker, such as in the case of LHC. This operation mode of the kickers will generate forced or driven oscillations. If the function generator is modulated in time, ramping the voltage from 0 to its maximum and lately, it is ramped down, the emittance increase will be smaller than in the single kick case. This mode of operation of the dipolar kicker is known as AC-dipole [87, 88, 48]. The external frequency generator works with a frequency different to the tune in order to avoid driving the beam to possible resonances. The driven tune is defined as the ratio of the external generator frequency and the beam revolution frequency. The driven frequency it is set to the closest possible to the natural tune avoiding raising resonances. The beam can be driven to a steady coherent oscillation by slowly ramping up the amplitude of an AC dipole oscillating field at a frequency in the vicinity of the beam betatron frequency [48, 89, 90, 91, 92]

Chapter 3

LHC Optics measurements and corrections

Optics measurements and corrections in LHC are performed with mainly two different goals. In the first place, as part of the commissioning of a new optics configuration. In the second place, optics measurements are also performed, aiming to have a better understanding of the beam dynamics in the LHC, allowing to improve the operation of the machine.

3.1 Optics measurement procedure in LHC

Optics measurements in LHC are based on two main techniques: turn-by-turn measurements and K-modulation. A schematic of the measurements procedure is summarised in Fig. 3.1.

Turn-by-turn measurements are performed in first place in order to evaluate the optics in the machine in the entire accelerator. K-modulation completes the knowledge of the lattice by measuring the β at the interaction point. Turn-by-turn measurement (approximately five acquisitions) are performed in order to consider all the possible fluctuations of the machine over time. On the other hand, K-modulation is performed over many times in order to acquire several periods of the current modulation. Most common excitation source used when performing optics measurements is the AC-dipole. It is operated in the following way: voltage applied to the excitation source is ramped-up from 0 to the maximum voltage in a period equivalent to 2000 turns of the beam in the accelerator. AC-Voltage is then kept constant during approximately 6600 turns and then it is slowly ramped down to 0. In this way, the adiabaticity of the process is assured. Optics measurements are performed during the AC-dipole plateau where the voltage is constant. The effect of the AC-dipole in the transverse beam dynamics has been studied in detail in [93]; it depends on the voltage, the difference between the beam tune and the excitation frequency. In the case of LHC 6600 turns are acquired and analysed, constrained by the length of the AC-dipole plateau.

The analysis process of optics measurements starts with noise removal using Single Value Decomposition (SVD) technique (reduce the noise in the measured BPM TbT)[49]. Only the 12 strongest singular modes were kept, since simulations show only marginal improvements for smaller cuts. Then, cleaned TbT measurements are analysed using advanced Fourier algorithms

[6, 52]. Fourier analysis provides information about the phase and the amplitude measured at each BPM in the frequency spectrum of TbT data [41, 42, 43, 94]. Amplitude and phase values of the main spectrum line measured at each BPM location allows computing β and coupling using the methodology described in Ch.1.

Turn-by-turn BPM data is also used for dispersion measurements, performed by shifting the frequency of the Radio Frequency (RF) systems in a range of ± 100 Hz for the LHC. Closed orbit shift is then measured using the zero frequency spectral line of the Fourier analysis, and then it is normalized by the momentum variation, Δp/p in order to obtain the dispersion function

Dispersion function is measured by performing off-momentum measurements that consist of changing the frequency of the radio-frequency with respect to the nominal value. The same procedure is followed when analysing off-momentum measurements.

K-modulation measurements are performed, in parallel to the turn-by-turn analysis, in the required interaction points (usually IP 1 and IP 5 but occasionally also in IP 2 and 8) [7, 45, 56, 46].

Once the analysis of K-modulation is completed, β (β^{ϕ} and $\beta^{\text{K-mod}}$), coupling and dispersion measurements are then compared to the values computed using MADX, obtaining the ϕ-beating, β-beating, D_x-beating and coupling. If the discrepancy between the measurement and the model is larger than the tolerances, the optics corrections (coupling, local and global corrections) are implemented in the machine. This process is repeated until reaching the β-beating, dispersion-beating and coupling tolerances.

Measurement procedure has been slightly modified during the last years to improve the accuracy and to speed up the acquisitions. Both in LHC and its injectors analysis of optics measurements is performed using python software that has been continuously developed since the first run of LHC [43, 95].

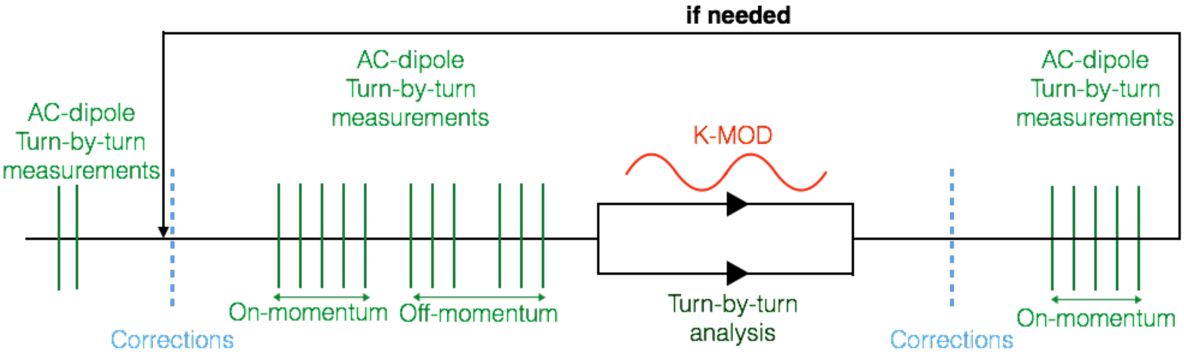

Figure 3.1: Schematic of optics measurements and corrections performed in LHC

3.2 Optics corrections in LHC

In LHC, strong localised magnetic errors have to be corrected in order to achieve the design value of the β function at the interaction point (IP) to provide, the designed luminosity within the 5% tolerance limits to the main experiments: ATLAS [37], ALICE [38], CMS [39] and LHCb

[40]. Strong and very localised source of errors, such as the triplet quadrupoles (MQXA and MQXB), are corrected using the local corrections technique while distributed errors around the ring are corrected using global corrections. Coupling corrections are also performed in parallel with the normal quadrupolar corrections based on measured coupling in the entire accelerator [96, 97].

On the other hand, global corrections are based on the analysis of the response matrix. They are used in order to correct, separately, the errors in both beams.

Optics corrections are implemented in the machine by modifying quadrupolar strengths associated with different power supplies. The set of all the quadrupolar strengths values is known as a knob. The value of the change in the quadrupolar strength is computed using measurements and MADX. Optics corrections are implemented by trimming the knobs in the machine in iterative steps using the LHC Software Architecture LSA, a LHC software that allows controlling the different hardware parameters.

3.3 LHC 2015 commissioning

During 2013 and 2014 beam was not circulating at the LHC and improvements in several parts of the hardware were performed during that time. The most relevant upgrade from an optics point of view was the increase in the length of the AC-dipole excitation that directly affects the precision of the Fourier transformation. The optics measurements and correction (OMC) team profit these two years gap to develop the existing software designed both for optics measurements and for optics corrections [2, 43, 42].

Optics measurements and corrections at injection energy were part of the 2015 LHC commissioning and during part of the machine development studies. These measurements were performed over several shifts during commissioning: 08/04/15, 09/04/15, 10/04/15, 23/04/15 and during machine studies the 28/08/15.

Commissioning at injection consisted of evaluating the latest hardware upgrades that had a potential effect on the LHC lattice properties and to correct the possible optics errors presented in the machine.

This process has first been performed at injection energy in order to minimise the risk of possible damage induced by the beam. The optics measurements and corrections process have been performed using the tools developed during the shutdown that also needed to be validated.

3.3.1 Optics measurements at injection

First optics measurements

Some hardware and software issues were found while trying to measuring the LHC lattice properties for the first time after the end of the long period of inactivity. During the first attempts to measure the optics more than 50% of the BPMs were malfunctioning. Figure 3.2 shows an example of bad turn-by-turn (TbT) data in both horizontal and vertical planes. Moreover, the

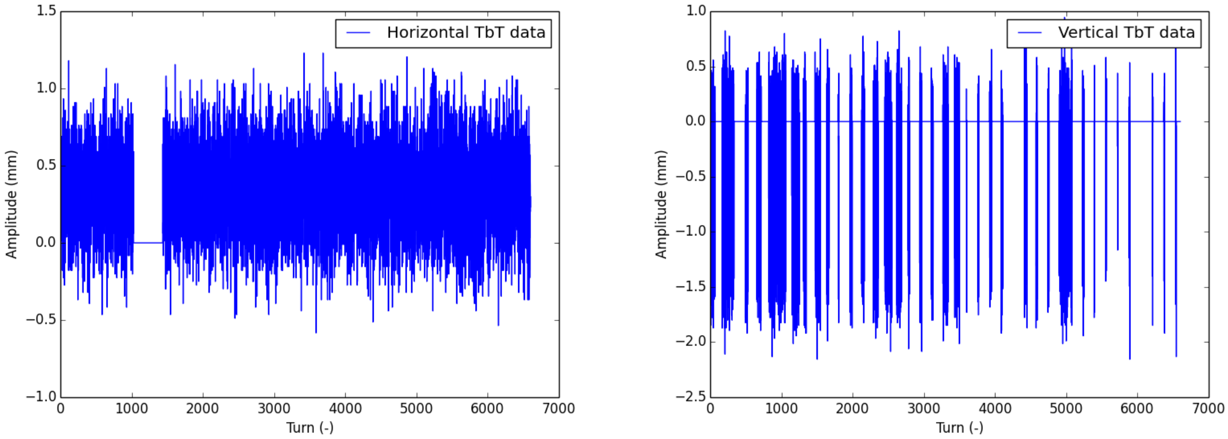

Figure 3.2: Bad TbT data acquired horizontal at the beginning of the commissioning.

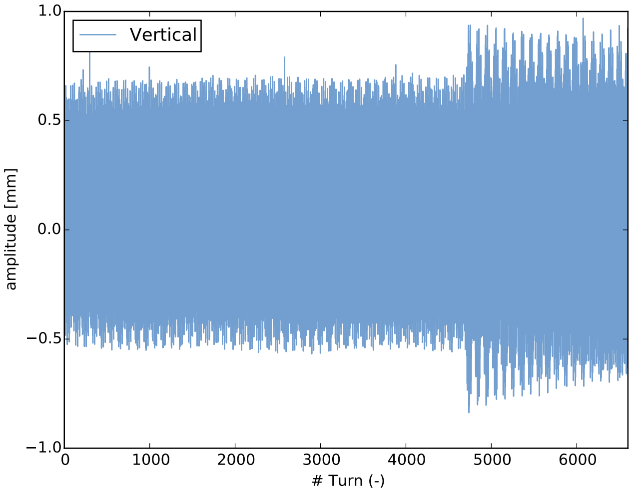

Figure 3.3: Bad TbT data acquired.

beam intensity was not high enough, and the AC-dipole amplitude had to be increased during the measurements causing some beam losses (especially in Beam 1) and limiting the resolution of optics measurements.

The problems with BPM acquisition combined with the poor β-beating and coupling resolution, did not allow us to calculate either β-beating or coupling corrections.

Second beta-beating measurements

During the second day of measurements, some issues were observed when exciting the beam with the AC-dipole. The vertical TbT data amplitude suddenly increased at turn= 4500, as can be observed in Figure 3.3. When analysing the data using the FFT (Fast Fourier transformation), unexpected shifts in the vertical natural tunes were observed.

Later, it was found that the presence of those jumps was related to a bad electrical connection that probably was leading to an irregular ramp during the AC-dipole cycle that can be observed in Fig. 3.4 [98, 89].

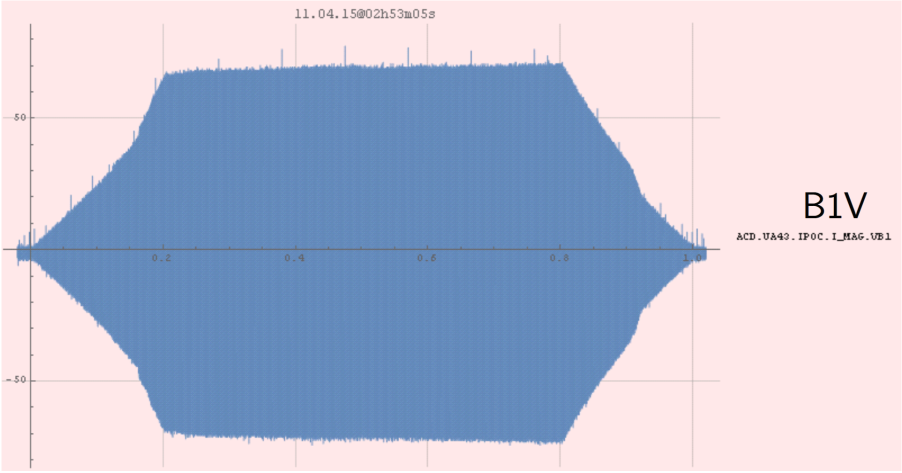

Figure 3.4: AC-dipole waveform showing deviations from ideal shape.

Additionally, some TbT data recorded by several BPMs were presenting amplitude spikes recording values larger than 20 mm when the average amplitude oscillation is below 2 mm. The BPMs that were recording bad TbT data were rejected for the analysis. Two main patterns were found when analysing the data: on the one hand, the number of BPMs with spikes increased linearly with the number of turns and, on the other hand, it seemed to be random which BPMs were affected for a particular measurement. Finally, after some studies, this problem was identified as an incompatibility between the two possible modes of operation of the BPM: TbT mode and the average orbit acquisition. The issue was solved by disabling the orbit mode during the performance of the optics measurements.

3.3.2 Global optics corrections

The goals of this measurement session were to analyse the β-beating measurements using the AC-dipole as an external excitation source and to implement optics corrections. Driven turn-by-turn measurements were analysed in order to obtain the β-functions both from ϕ-advance and from amplitude. Later, measured β^{ϕ}-function together with dispersion was used in order to compute global corrections parameters. Corrections were implemented following an iterative process in order to reduce the large β-beating around the accelerator. Global corrections implemented in the machine in 2012 were used as a guideline for computing the corrections in 2015.

A comparison of the change in the quadrupolar strength applied to a different set of quadrupoles is shown in Figures 3.5 and 3.6 both for 2012 and 2015. In these plots, quadrupoles are divided into three categories: the insertion region quadrupoles (MQMs), the tunning quadrupole corrector in arc short straight section (MQTs) and the insertion wide aperture quadrupole (MQYs).

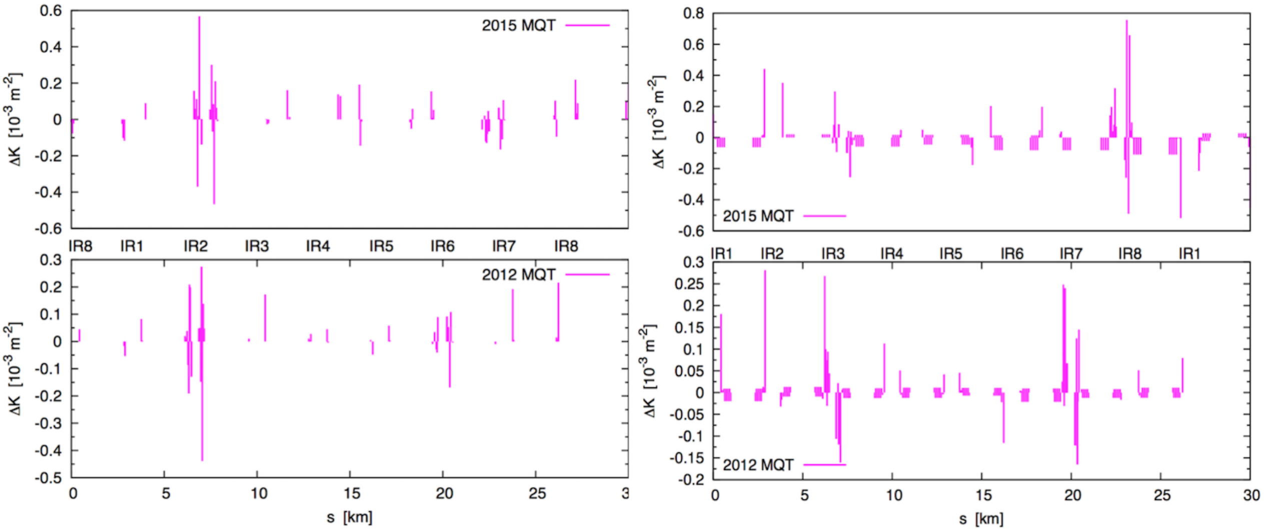

Figure 3.5: Corrections applied to the MQTs in 2012 and 2015 (Beam 1 left and Beam 2 right).

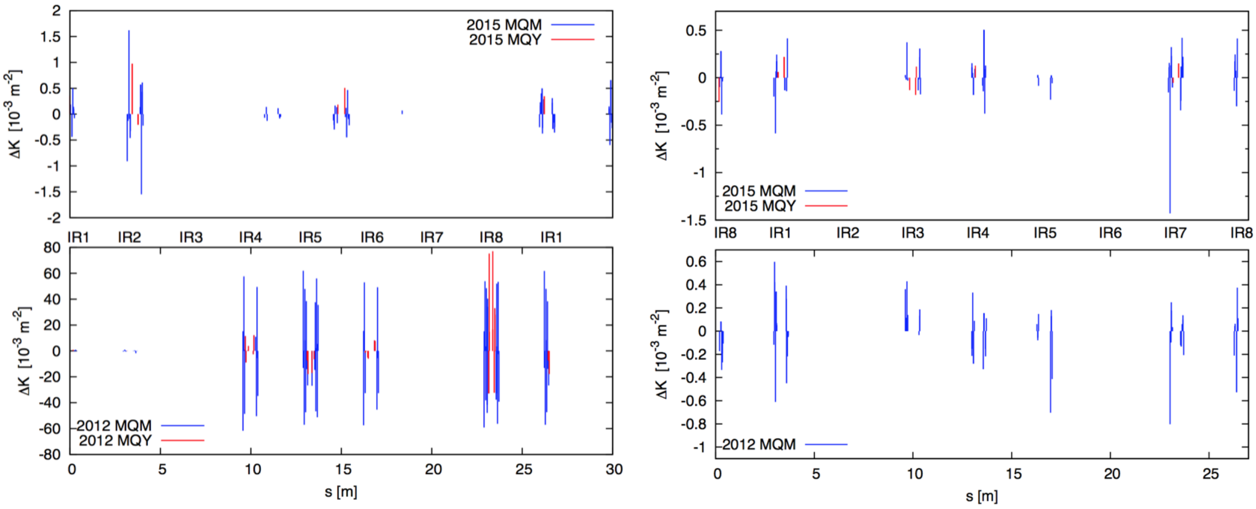

Figure 3.6: Corrections applied to the MQMs and MQYs in 2012 and 2015 (Beam 1 left and Beam 2 right).

The effectiveness of the corrections is then evaluated by repeating on-momentum optics measurements. Figures 3.7 and 3.8 show a comparison between measurements before and after corrections.

β-function measured in 2012 was used as a reference value for the process of iterative corrections. Figures 3.9 and 3.10 show a comparison between data from 2015 and data from 2012 before the corrections were applied. Finally, comparisons between data from 2015 and 2012 with corrections applied are shown in Figures 3.11 and 3.12. The phase method used during this commissioning was an improved version of the three BPM phase-advance method [1] (used during the 2012 commissioning). The new method N-BPM is a more sophisticated algorithm that takes into account both the statistical and systematic errors involved in this measurement

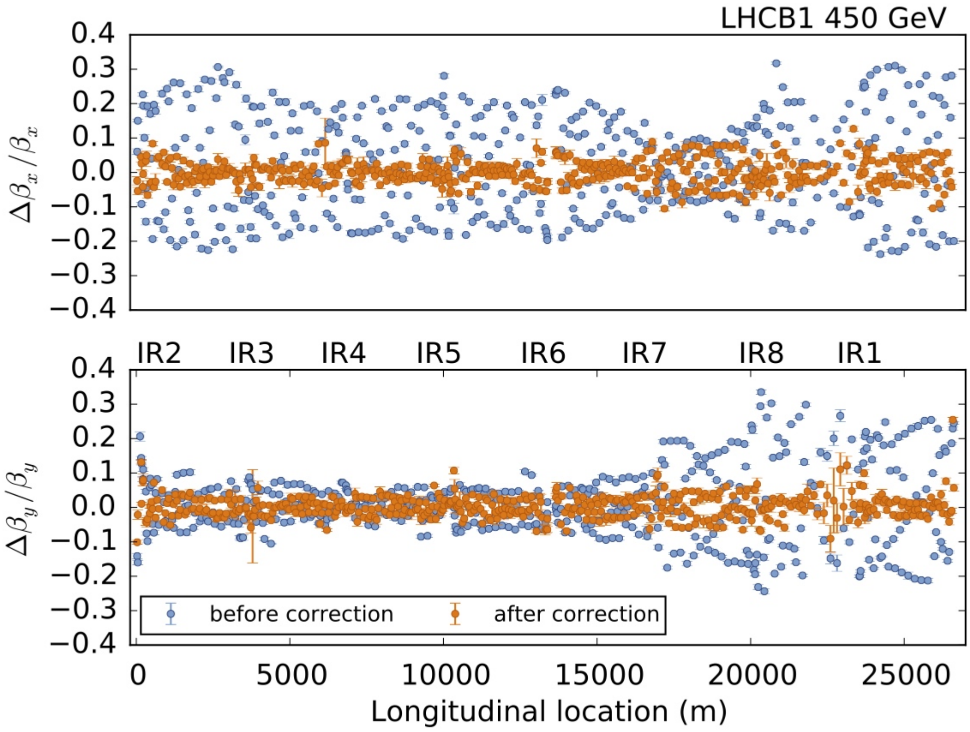

Figure 3.7: β-beating before and after corrections were applied (2015 Beam 1).

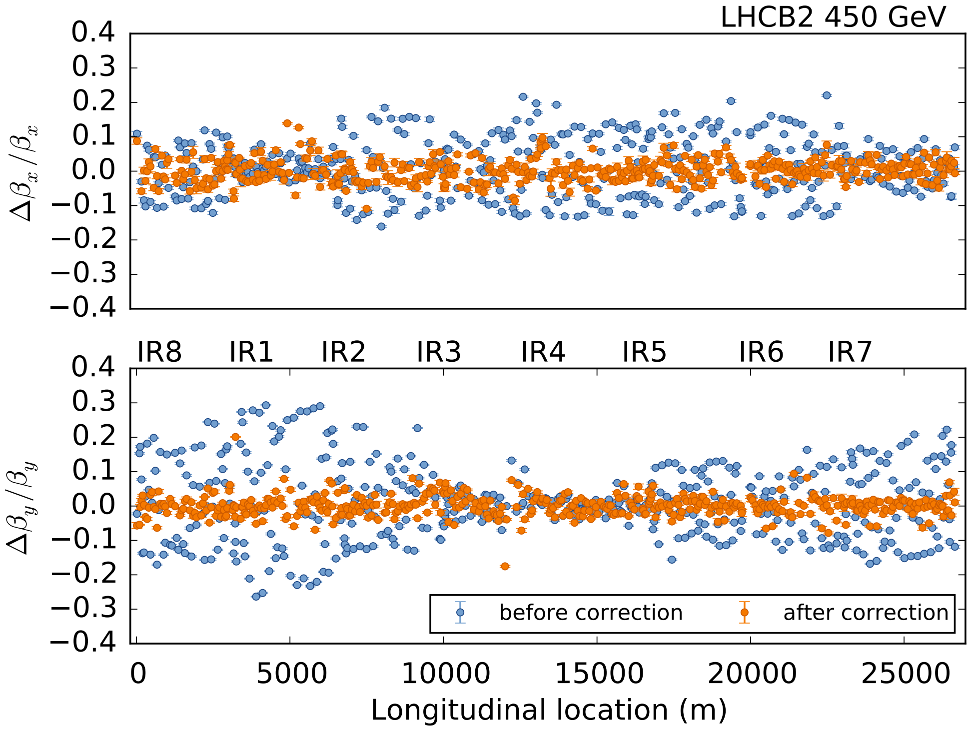

Figure 3.8: β-beating before and after corrections were applied (2015 Beam 2).

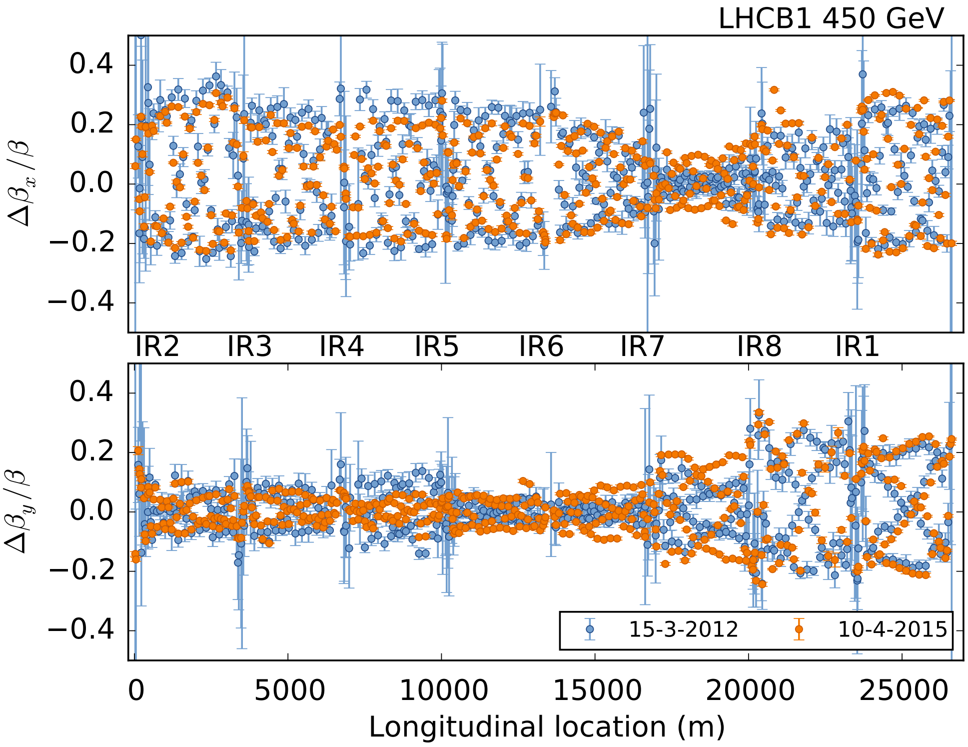

Figure 3.9: β-beating from 2012 and 2015 before corrections were applied (Beam 1).

[2]. The implementation of the new approach makes it possible to combine more beam position monitor measurements for deriving the optical parameters and, demonstrates to improve the accuracy and precision significantly. It can be observed how the implementation of the new β^{ϕ} approach improves the precision of the β-function in overall and especially in the IRS.

Although β^{A} was not used for computing the global corrections, a comparison of the β-function obtained both β^{ϕ} and β^{A} was performed in order to observe the discrepancies between these two approaches and the impact of the BPM calibration factors in the measurements. Figures 3.13 and 3.14 show the β-function measured using β^{A} and β^{ϕ}. Two conclusions can be drawn from these figures: a systematic lower discrepancy between the two approaches is observed at particular locations of the accelerator coinciding with the location of the interaction points, and a larger spread of the β-beating is observed when using the β^{A}. Both observations have been studied in-depth as part of the studies presented in this thesis and are introduced in Ch. 4 and in Appendix A.

3.3.3 β-beating measurements during machine development studies

During the second block of the machine development studies [99] some optics measurements were made with the primary goal to review the optics measurements at injection. β-beating measurements performed for both beams are shown in Figures 3.15 and 3.16 observing that the quality of the optics had not been degraded with time.

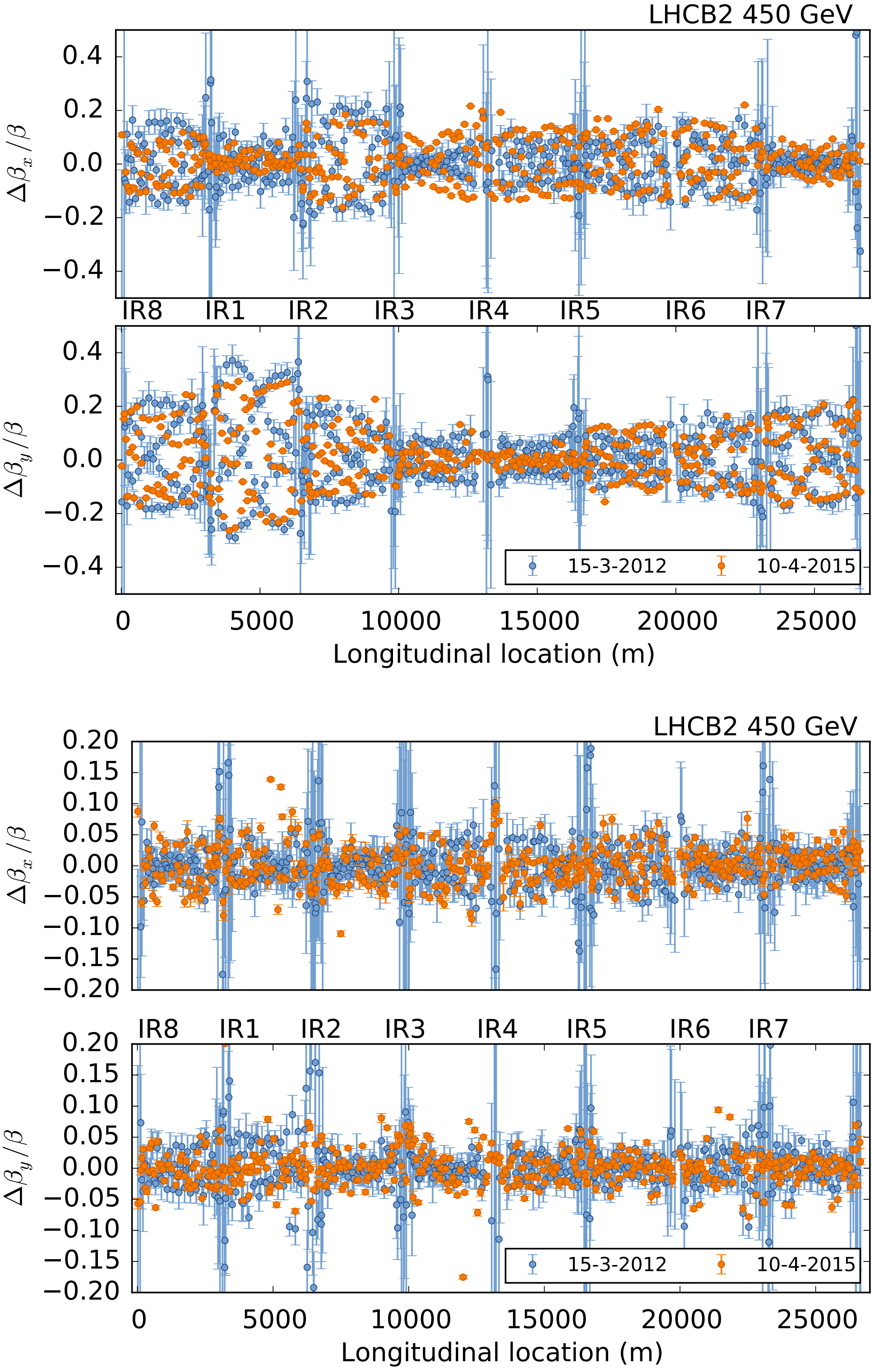

Figure 3.10: β-beating from 2012 and 2015 before corrections were applied (Beam 2).

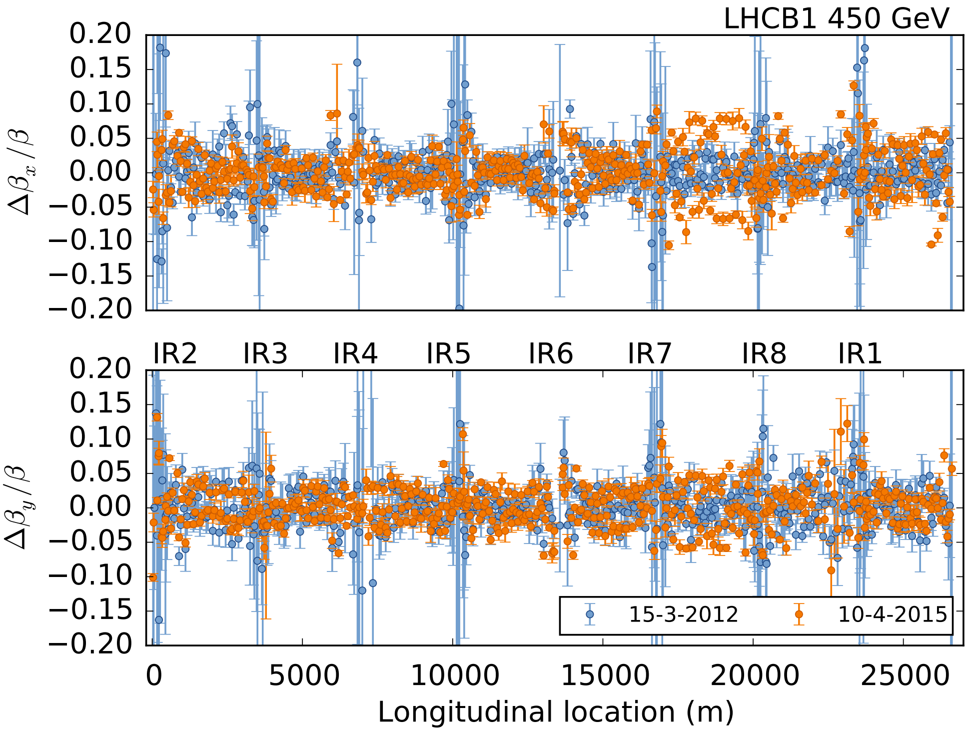

Figure 3.11: β-beating from 2012 and 2015 after corrections were applied (Beam 1).

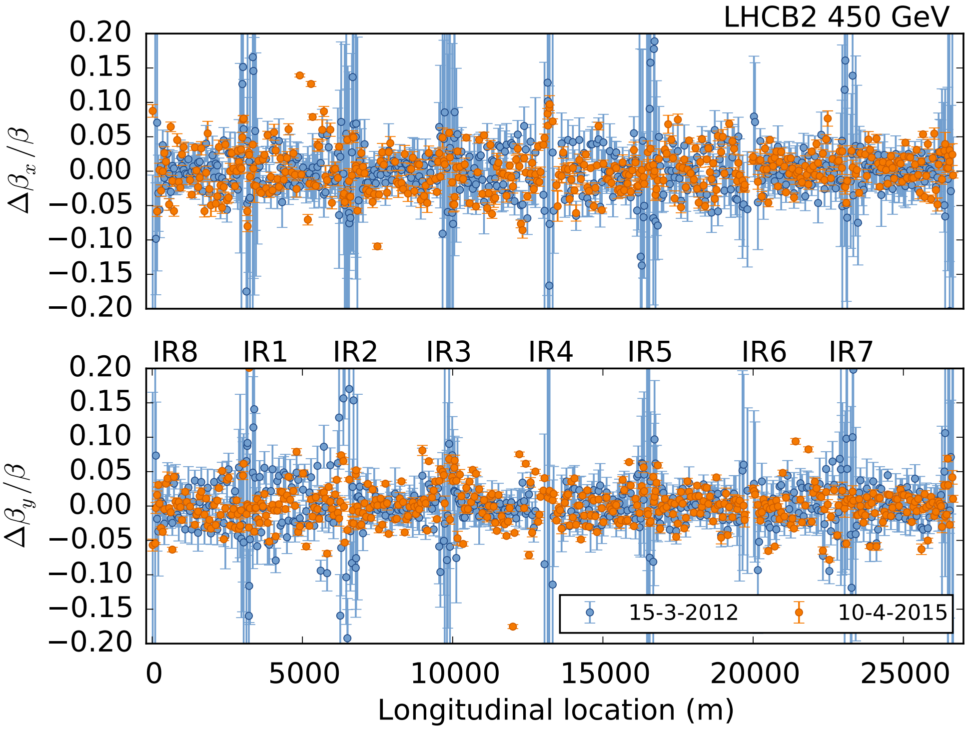

Figure 3.12: β-beating from 2012 and 2015 after corrections were applied (Beam 2).

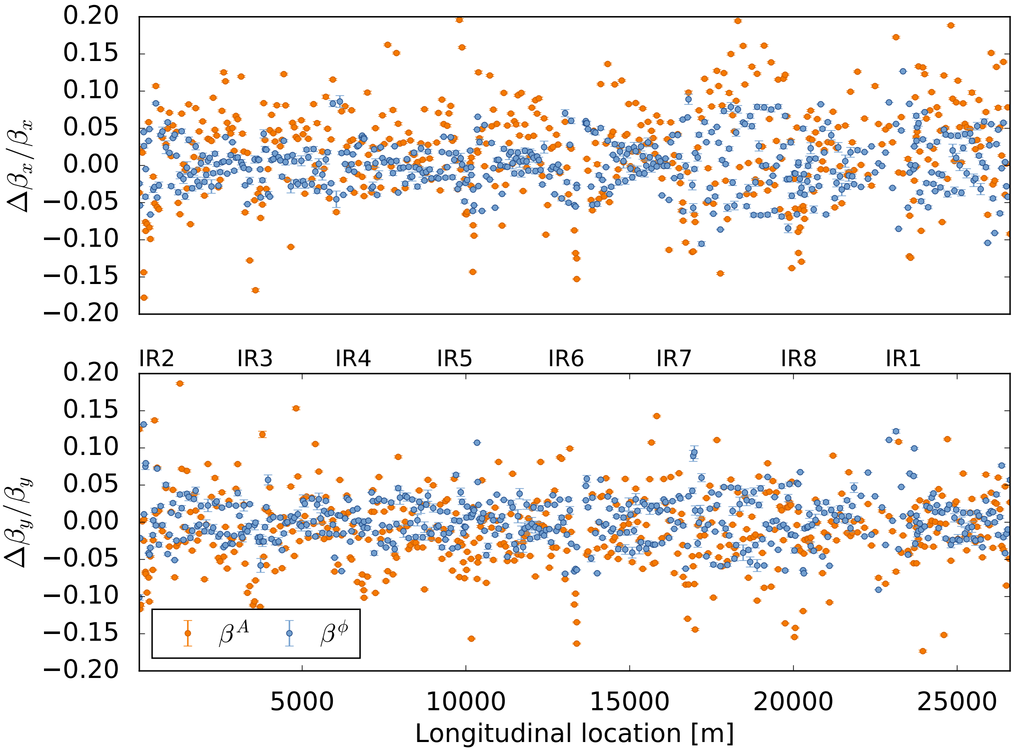

Figure 3.13: β-beating after corrections were applied using β^ϕ and β^A (2015 Beam 1).

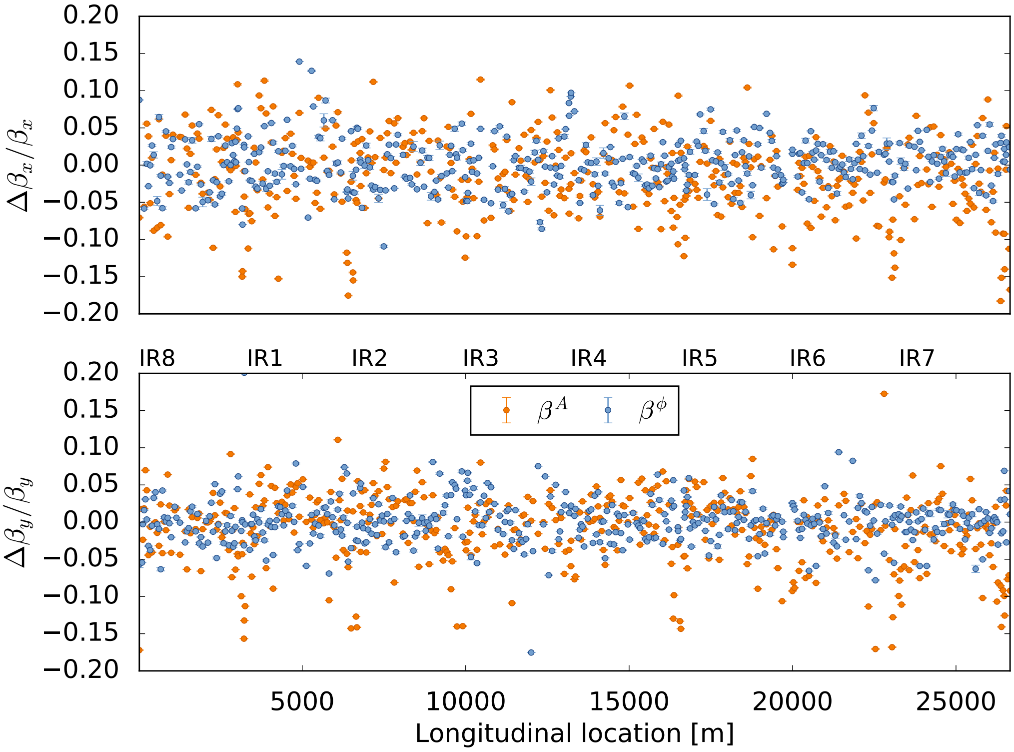

Figure 3.14: β-beating after corrections were applied using β^ϕ and β^A (2015 Beam 2).

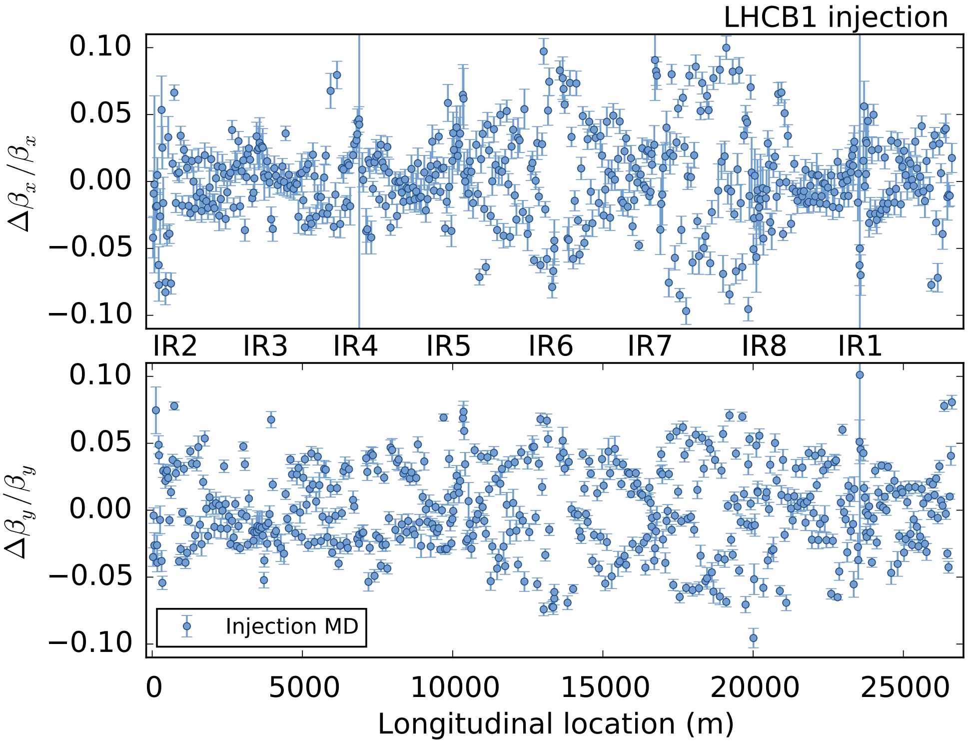

Figure 3.15: β-beating from 2015 MD (Beam 1).

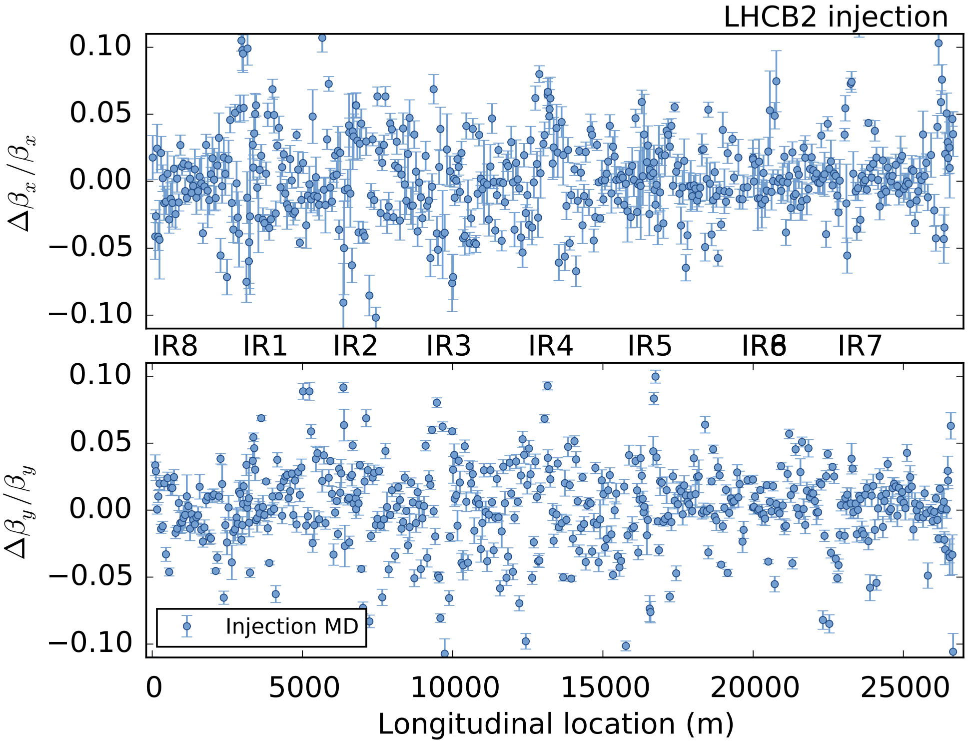

Figure 3.16: β-beating from 2015 MD (Beam 2).

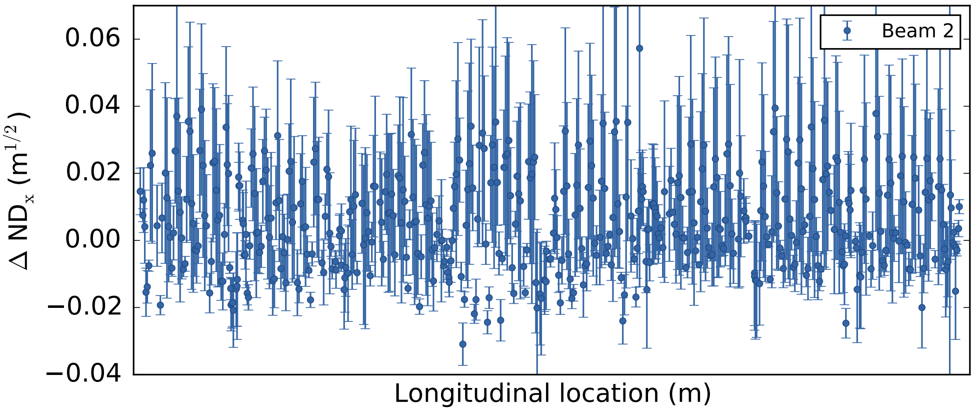

Figure 3.17: Normalised dispersion for Beam 2 (commissioning 23/04/2015).

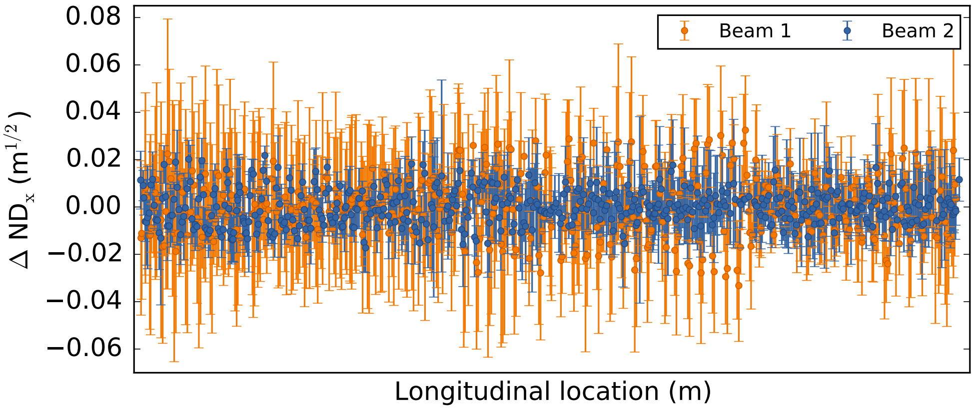

Figure 3.18: Normalised dispersion for Beam 1 and Beam 2 (MD 28/08/2015).

3.3.4 Dispersion

Figures 3.17 and 3.18 show the normalised dispersion measured during the commissioning and the MD, respectively. Normalised dispersion aims to replace dispersion function when measuring the dispersive effects of the optics. It is an observable introduced in [58] that is not affected by the calibration factors, and that is explained in detail in Ch. 4. As it can be seen in Fig.3.17 the normalised dispersion of Beam 1 was not measured during the commissioning. The dispersion measured during the MD shows large uncertainties values for Beam 1.

A considerable decrease in the error bars amplitude can be observed in Figure 3.18 in Beam 2. Nevertheless, the measured dispersion of Beam 1 was still showing significant uncertainties.

The large values of the error bars were caused by a movement on the IR8 triplets, which resulted in drifts of the beam orbit. The large error bars are a direct effect of the orbit drifts. The quadrupole movements were found to be caused by a problem with a regulation valve of the cryogenic system. After this issue has been fixed, reliable dispersion measurements and corrections were possible again in 2016.

3.4 Conclusions

The injection commissioning has allowed detecting several problems in hardware devices: BPMs and AC-dipole and also in the analysis software. This process led to a more stable framework (software and hardware). The software upgrades in the β-beating calculations together with a sizeable AC-dipole excitation have led to more precise results. A significant decrease in the values of the β-beating error bars have been observed implemented the new methodology of β^{ϕ}. Results of optics measurements at injection energy have been shown in this report. β-beating has been successfully corrected using global corrections. Comparison of β-functions using two approaches, β^{ϕ} and β^{A} has triggered a detailed analysis of the BPM calibration factors that are introduced in Ch. 4. Finally, issues in dispersion measurements were spotted during the LHC commissioning and they were investigated during 2015, allowing to obtain accurate measurements of dispersion from 2016.

Chapter 4

Optics-measurements-based BPM calibrations and β^{A} error-bar calculation

Knowledge of BPM calibration factors would allow to accurately measure β function with β from amplitude (β^{A}) where the performance of other approaches is limited. In low β^* runs, the resolution required in the IR phase advance measurement is below the resolution that can be provided by the BPMs placed in the IR. In those scenarios, the amplitude of the transverse oscillations recorded in the BPMs closest to the IP increases as the β^* decreases, but phase advance between neighbour BPMs drops to small values. β^{ϕ} approach is very sensitive to errors for values of the BPMs phase advance close to nπ. In order to obtain the required β accuracy, the BPM resolution should be ten times smaller than the best resolution achievable by the LHC BPMs [100]. Therefore, with the current resolution and reconstruction techniques, the β^* obtained using phase advance method in the interaction regions (IRs) during the squeeze will provide unaccurate values that cannot be used as reference values for local corrections [101].

Turn-by-turn BPM data is also used for dispersion measurements, performed by shifting the frequency of the Radio Frequency (RF) systems in a range of ± 100 Hz for the LHC. Closed orbit shift is then measured using the zero frequency spectral line of the Fourier analysis, and then it is normalized by the momentum variation, Δp/p in order to obtain the dispersion function. Dispersion calculation is as well biased by the BPM calibration factors. In [58], normalized dispersion $ND_x = \frac{D_x}{\sqrt{\beta^{\mathrm{x}}}}$ is introduced as a calibration independent observable. Since it is calculated as a ratio between two calibration-dependent quantities the effect of the calibration factor is canceled and therefore, the resultant quantity is calibration-independent.

This chapter introduces two optics-based-BPM-calibration methods using β function and dispersion measurements: using the ratio between two β functions ($\sqrt{\beta^{\phi}/\beta^{\mathrm{A}}}$) and the ratio between horizontal normalized dispersion function times the $\sqrt{\beta_x^{\phi}}$ and the dispersion function $\left(D_x/ND_x\sqrt{\beta_x^{\phi}}\right)$. Calibration factors are calculated in an optics configuration where the lattice systematic errors affect as less as possible the β^{ϕ} and dispersion measurements. An optics that is suitable for this method is the Ballistic or Alignment optics, characterized by having the triplets switched off [102]. This optics configuration was first designed for alignment of the

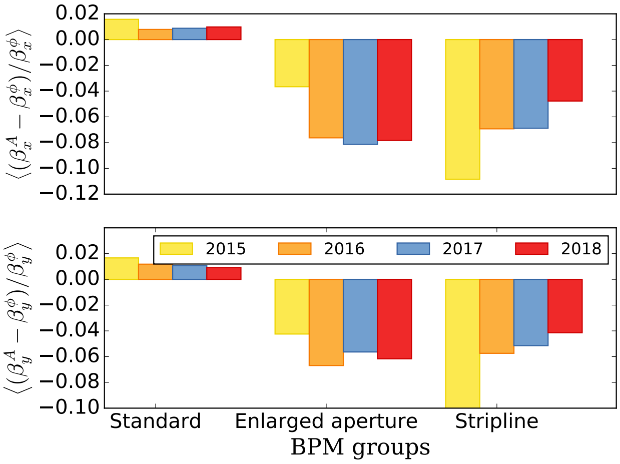

Figure 4.1: Top: Average horizontal amplitude β-beating with respect to β^ϕ, Bottom: Average vertical amplitude β-beating with respect to β^ϕ. The optics analyzed include injection optics for four consecutive years. The BPMs have been divided in groups depending on their geometry according to Tab. 4.1.

magnets placed in the triplet area, the Q1, Q2 and Q3 quadrupoles. An extended version of this optics, designed in 2017 specifically for BPM calibration studies, has Q4 quadrupoles also switched off and the dispersion in the IRs 1 and 5 was not matched to zero [103].

The calibration analysis has been focused on the IRs because during the annual LHC commissioning [104, 105] a systematic difference between the results obtained using β^ϕ and β^A was observed in this region. An illustration of this systematic deviation is quantified in Fig. 4.1, horizontal in the top and vertical in the bottom as a function of the BPM type. Different types of BPMs are installed in LHC with different aims. They have been grouped according to the geometry of the pick-ups in the following categories: standard, enlarged aperture and stripline as shown in Tab. 4.1 [106]. Standard or cold BPMs are button BPMs, and they are the most widely used type of pick-ups installed in the LHC arcs. Enlarged aperture BPMs are also button BPMs with a larger aperture and are placed close to the recombination dipoles. Stripline or directional BPMs, able to measure the beam direction, are placed in the common areas where both beams circulate in one vacuum pipe. The average β-beating, $\left\langle(\beta^\mathrm{A}-\beta^\phi)/\beta^\phi\right\rangle$ between the two techniques, illustrates that a systematic lower value is obtained in the β^A with respect to the β^ϕ in the case of stripline and enlarged aperture BPMs.

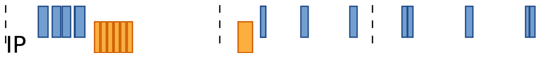

Name	Stripline		Enlarged Aperture	Standard
Geometry	Strip-line		Button	Button
LHC prefix	BPMS	BPMSX	BPMW	BPM
Aperture	61 mm	81 mm	61 mm	49 mm

Table 4.1: Summary of BPM characteristics and location shown schematically on the top.

Figure 4.2 shows the histogram of the ratio $\sqrt{\beta^\mathrm{A}/\beta^\phi}$ measured for several optics: Injection, Flattop, Ballistic [11] a and High-β^* [107] for stripline BPMs.

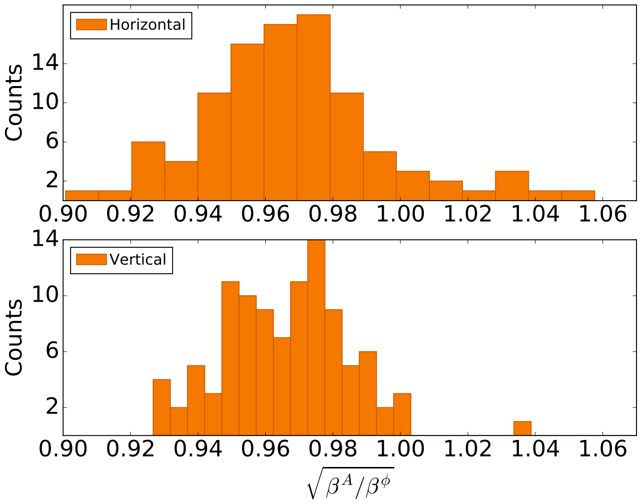

Figure 4.2: Histogram of the ratio $\sqrt{\beta^{\mathrm{A}}/\beta^{\phi}}$ in the stripline BPMs measured in 2017 using different optics configurations: Injection [16], Flattop, High-β^* and Ballistic.

This chapter is structured as follows. Section 4.1 presents a detailed analysis of β^{A} method together with the study of MADX simulations that estimate the systematic error-bar of the β^{A} approach. A description of the Ballistic optics together with the calibration factors obtained using both β function and dispersion are presented in section 4.2. Section 4.3 compares the β^* calculated for different optics configurations with and without applying the calibration factors and compares these results to the results obtained with the β^{ϕ} and the $\beta^{\text{K-modulation}}$ approaches.

4.1 Optics measurements in LHC: Methods and limitations.

4.1.1 β-from amplitude analysis

LHC turn-by-turn optics measurements are based on the analysis of AC-dipole driven oscillations which can be observed in the BPMs [93]. This data is post-processed using Fourier transformation methods in order to obtain the amplitude and phase of each spectral line [108]. These values are later analyzed for the reconstruction of the different optics parameters. Linear optics studies are especially focused on the analysis of amplitude and phase corresponding to the main line of the spectrum, associated to the driven tune. For the i$^{\mathrm{th}}$ BPM, ideal amplitude and phase are related to the beam position, $\beta_i^{\mathrm{A,D}}$ through:

$$x_i, y_i(N)^{\mathrm{D}} = A^{\mathrm{D}}_{x,y,i}\sin(\mu^{\mathrm{D}}_{\mathrm{x,y,i}} + 2\pi Q^{\mathrm{D}}_{\mathrm{x,y}}N), \tag{4.1}$$

where $A^{\mathrm{D}}_{x,y,i}$, $\mu^{\mathrm{D}}_{x,y,i}$ and $Q^{D}_{x,y}$ are the amplitude, the phase and the tune of the driven motion respectively. The amplitude, $A^{\mathrm{D}}_{x,y,i}$, can also be expressed in terms of the driven β function, $\beta^{\mathrm{D}}_{x,y,i}$, and a common observable for all BPMs, the driven action, $2J^{\mathrm{D}}_{x,y}$,

$$A^{\mathrm{D}}_{x,y,i} = \sqrt{2J^{\mathrm{D}}_{x,y}\beta^{\mathrm{D}}_{x,y,i}}. \tag{4.2}$$

In order to simplify the equations, the subindex x and y are omitted in the following. Since measurement of the oscillation amplitude is biased by the individual BPM calibration factors, C_i, measured amplitude, $\mathrm{A}_i^{\mathrm{D,meas}}$, deviates from Eq. (4.2) as:

$$A_i^{D,\mathrm{meas}} = C_i^{\mathrm{A}}\sqrt{2J^{\mathrm{D}}\beta_i^{\mathrm{D}}}. \tag{4.3}$$

The amplitude of the driven transverse excitations, $\mathrm{A}_i^{\mathrm{D,meas}}$, is a direct measurement obtained from the Fourier analysis of the transverse oscillations and is the basis for the β^{A} analysis.

In order to obtain the value of the action induced by the AC-dipole, it is necessary to normalize the square of the amplitude of the transversal excitations, $(\mathrm{A}_i^{\mathrm{D,meas}})^2$, by the β_i^{D} function. This value can be obtained in two ways, using either the measured $\beta_i^{\phi,\mathrm{D}}$ or the model $\beta_i^{\mathrm{model,D}}$ given by MADX [109]. The average of the product of the action times the square of the individual calibration factors can be expressed regrouping the terms in Eq. (4.2) as:

$$\frac{1}{\mathrm{N}}\sum_{i=1}^{\mathrm{N}}\left(C_i^{\mathrm{A}}\right)^2 2J^{\mathrm{D}} = \frac{1}{\mathrm{N}}\sum_{i=1}^{\mathrm{N}}\frac{\left(A_{\mathrm{i}}^{\mathrm{D,meas}}\right)^2}{\beta_i^{\mathrm{D}}}, \tag{4.4}$$

where N is the number of BPMs.

From Fig. 4.1 it can be seen that the discrepancies between the two approaches - β^{ϕ} and β^{A}- is different for the BPMs placed in the arcs than for the BPMs placed in the IRs, especially the stripline BPMs. In order to minimize the effects of the calibration factors, the summation is restricted to a subest of N' BPMs corresponding to the LHC standard BPMs. Equation (4.4) can be rewritten as:

$$\frac{1}{\mathrm{N}'}\sum_{i=1}^{\mathrm{N}'}\left(C_i^{\mathrm{A}}\right)^2 2J^{\mathrm{D}} = \frac{1}{\mathrm{N}'}\sum_{i=1}^{\mathrm{N}'}\frac{\left(A_{\mathrm{i}}^{\mathrm{D,meas}}\right)^2}{\beta_i^{\mathrm{D}}}. \tag{4.5}$$

In order to simplify the notation, the average of the product of the action times the individual calibration factors square will be denoted as calibration weighted action given by:

$$2J_C^{\mathrm{D}} = \overline{(C_i^{\mathrm{A}})^2}2J^{\mathrm{D}} = \frac{1}{\mathrm{N}'}\sum_{i=1}^{\mathrm{N}'}\frac{\left(\mathrm{A}_{\mathrm{i}}^{\mathrm{D,meas.}}\right)^2}{\beta_i^{D}}. \tag{4.6}$$

Once the calibration weighted action is calculated, the driven β-function at a given BPM, $\beta_i^{\mathrm{A,D}}$, can be computed by normalizing the amplitude by the driven action

$$\beta_i^{\mathrm{A,D}} = \frac{(A_i^{\mathrm{D,meas}})^2}{\overline{(C_i^{\mathrm{A}})^2}2J^{\mathrm{D}}} = \frac{(A_i^{\mathrm{D,meas}})^2}{2J_C^{\mathrm{D}}}. \tag{4.7}$$

Equation (4.7) can be expressed in terms of the ideal unknown $\beta_i^{\mathrm{A,D}}$ function as:

$$\beta_i^{\mathrm{A,D}} = \frac{(C_i^{\mathrm{A}})^2 \beta_i^{\mathrm{D}}}{\overline{(C^{\mathrm{A}})^2}} \tag{4.8}$$

which shows that the $\beta_i^{\mathrm{A,D}}$ calculation is affected by a factor $(C_i^{\mathrm{A}})^2/\overline{(C^{\mathrm{A}})^2}$, i.e, the standard BPMs calibration factors also have an impact in the $\beta_i^{\mathrm{A,D}}$ function calculation.

In order to obtain the lattice β function, β_i^{A}, the effect induced by the AC-dipole in the measured amplitude has to be compensated. This compensation is based on the phase advance, $\phi_{i\Rightarrow\text{AC-dipole}}$, between the AC-dipole and the i^{th} BPM as:

$$\beta_i^{\mathrm{A}} = \frac{(C_i^{\mathrm{A}} A_i^{\mathrm{D}})^2}{2J_C^{\mathrm{D}}} \frac{1 + \lambda^2 + 2\lambda \cos(\phi_{i\Rightarrow\text{AC-dipole}})}{1 - \lambda^2} \tag{4.9}$$

where λ is given by the tune separation, $\lambda = \frac{\sin[\pi(\mathrm{Q_d} - \mathrm{Q})]}{\sin[\pi(\mathrm{Q_d} + \mathrm{Q}))]}$ and $\phi_{i\Rightarrow\text{AC-dipole}}$ is the phase advance between the BPM i and the AC-dipole [93]. The following section studies the β_i^{A} uncertainties, $\sigma_{\beta_i^{\mathrm{A}}}$.

Action uncertainty analysis $\sigma_{2J_C^{\mathrm{D}}}$ for β^{A} calculation

The action calculation, $2J_C^{\mathrm{D},\phi}$, using a previously computed β function, $\beta_i^{\mathrm{D},\phi}$, based on the measured phase advance between two BPMs, $\Delta\phi_{i,j}$, at the position i, is given by:

$$2J_C^{\mathrm{D},\phi} = \frac{1}{\mathrm{N}'} \sum_{i=1}^{\mathrm{N}'} \frac{\left(C_i^{\mathrm{A}} \mathrm{A}_{\mathrm{i}}^{\mathrm{D}}\right)^2}{\beta_i^{D,\phi}}. \tag{4.10}$$

In the past, action calculation $2J_C^{\mathrm{D}}$ was computed using a model value provided by MAD-X -$\beta_i^{\mathrm{D,model}}$- instead of $\beta_i^{D,\phi}$. A study of the error introduced when using $\beta_i^{\mathrm{D,model}}$ as reference value is introduced in Appendix A.1. This study includes both analytical studies and simulations and concludes that the average β-beating, defined as the relative difference between the $\beta_i^{D,\phi}$ and $\beta_i^{\mathrm{D,model}}$, increases quadratically with the lattice magnetic errors. Because of that, $\beta_i^{D,\phi}$ has been chosen as the reference value for the action calculation in the LHC. On the other hand, in accelerators where the $\beta_i^{\mathrm{D},\phi}$ cannot be accurately measured, such as in the PSB, $\beta_i^{\mathrm{D,model}}$ replaces $\beta_i^{D,\phi}$ in the action calculation.

Calibration factors are a source of error present in the action calculation, and they are a challenging limitation for the β^{A} method. This section focuses on the calibration factors associated with the button BPMs since the action calculation is averaged only over this kind of BPMs. Figure 4.3 shows that the calibration factors, estimated using the ratio $\sqrt{\beta^{\mathrm{A}}/\beta^{\phi}}$, follow a Gaussian distribution for two optics- Flattop and Ballistic- with a spread $\sigma(C^{\mathrm{A}})$.

The effect of the individual calibrations in the action calculation can be further studied splitting the calibration factors C_i^{A} in two terms: an average term $\overline{C^{\mathrm{A}}}$ and an individual spread term $\widetilde{C_i^{\mathrm{A}}}$ as $C_i^{\mathrm{A}} = \overline{C^{\mathrm{A}}} + \widetilde{C_i^{\mathrm{A}}}$.

Equation (4.10) can be simplified by denoting $2J_i^{\mathrm{D},\phi} = \frac{\left(A_{\mathrm{i}}^{\mathrm{D}}\right)^2}{\beta_i^{\mathrm{D},\phi}}$.

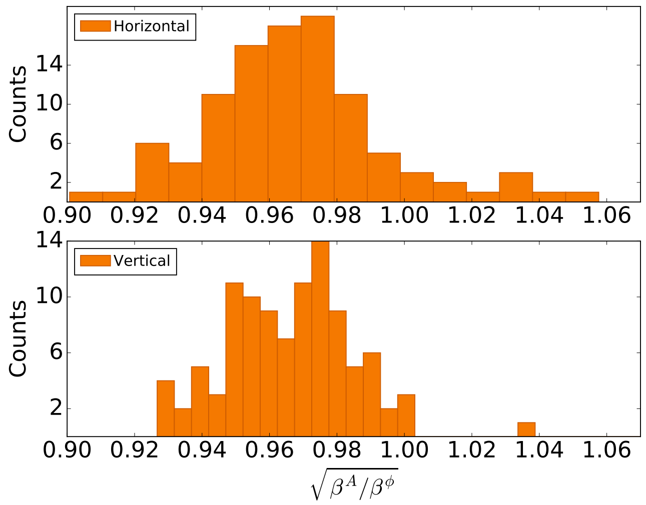

Figure 4.3: Histogram of the ratio $\sqrt{\beta^{\mathrm{A}}/\beta^{\phi}}$ in the ARC BPMs measured in different optics configurations.

$$\begin{aligned} 2J_C^{\mathrm{D},\phi} &\approx \frac{1}{\mathrm{N}'}\sum_{i=1}^{\mathrm{N}'}\left(\overline{C^{\mathrm{A}}}+\widetilde{C_i^{\mathrm{A}}}\right)^2 2J_i^D \approx \\ &\approx \overline{2J_C}^{\mathrm{D},\phi}+\widetilde{2J_C}^{\mathrm{D},\phi} \end{aligned} \tag{4.11}$$

Additionally, Eq. (4.11) has been regrouped in two terms: a term $\overline{2J_C}^{\mathrm{D},\phi}$ representing the average value of the action over all the button BPMs and a second term $\widetilde{2J_C}^{\mathrm{D},\phi}$ that express the spread introduced in the action calculation calibration factors:

$$\begin{aligned} \overline{2J_C}^{\mathrm{D},\phi} &= \frac{\overline{C^{\mathrm{A}}}^2}{\mathrm{N}'}\sum_{i=1}^{\mathrm{N}'}2J_i^{D,\phi}+\frac{1}{\mathrm{N}'}\sum_{i=1}^{\mathrm{N}'}2J_i^D\widetilde{C_i^{\mathrm{A}}}^2 \\ &\approx \frac{\overline{C^{\mathrm{A}}}^2}{\mathrm{N}'}\sum_{i=1}^{\mathrm{N}'}2J_i^{D,\phi}+\frac{\sigma^2(C^{\mathrm{A}})}{\mathrm{N}'}\sum_{i=1}^{\mathrm{N}'}2J_i^{D,\phi} \\ &\approx \left(\overline{C^{\mathrm{A}}}^2+\sigma^2(C^{\mathrm{A}})\right)\frac{1}{\mathrm{N}'}\sum_{i=1}^{\mathrm{N}'}2J_i^{D,\phi} \end{aligned} \tag{4.12}$$

$$\widetilde{2J_C}^{\mathrm{D},\phi} = \frac{2\overline{C^{\mathrm{A}}}}{\mathrm{N}'}\sum_{i=1}^{\mathrm{N}'}2J_i^{D,\phi}\widetilde{C_i^{\mathrm{A}}} \tag{4.13}$$

$\overline{2J_C}^{\mathrm{D},\phi}$ is affected by the average calibration factor, $\overline{C^{\mathrm{A}}}^2$ and the square of this spread. An estimation of the upper limit of the standard BPM calibration factors spread can be obtained computing the standard deviation of the ratio $\sqrt{\frac{\beta^{\mathrm{A}}}{\beta^{\phi}}}$. Figure 4.3 illustrates the distribution of the measured ratio $\sqrt{\frac{\beta^{\mathrm{A}}}{\beta^{\phi}}}$ for all the standard BPMs. The relative spread of the action, $\frac{\sigma(2J_C^{\mathrm{D},\phi})}{2J_C^{\mathrm{D},\phi}}$, can be estimated by Eq. 4.13.

$$\frac{\sigma(2J_{\mathrm{C}}^{\mathrm{D},\phi})}{2J^{\mathrm{D},\phi}} \approx 2\sigma(C^{\mathrm{A}}). \tag{4.14}$$

The relative error-bar, $\sigma(2J_{\mathrm{C}}^{\mathrm{D},\phi})/2J_{\mathrm{C}}^{\mathrm{D},\phi}$, of the action computed averaging over the N′ button BPMs is given by the error of the average:

$$\frac{\sigma(2J_{\mathrm{C}}^{\mathrm{D},\phi})}{2J_{\mathrm{C}}^{\mathrm{D},\phi}} = \frac{\sigma(2J_{\mathrm{C}}^{\mathrm{D},\phi})}{\sqrt{\mathrm{N}'-1}} \approx \frac{2\sigma(C^{\mathrm{A}})}{\sqrt{\mathrm{N}'-1}} \approx 0.2\%. \tag{4.15}$$

β^{A} uncertainties analysis

Reconstruction of β function using the amplitude of the transverse oscillations is affected by uncertainties on different parameters: natural tunes ($\mathrm{Q_{x,y}}$), driven tunes ($\mathrm{Q^{D}_{x,y}}$), phase advance between the AC-dipole and the ith BPM, $\phi_{i\Rightarrow\mathrm{AC}}$, amplitude fluctuations between BPMs due to the calibration factor spread and the action calculation $2J_{\mathrm{C}}^{\mathrm{D},\phi}$.

The natural tune uncertainty is given by a combination of the BBQ [110] system accuracy and by its stability as a function of time. This stability has been analyzed for several different optics in [57] concluding that in average the natural shift observed during the measurements fluctuates in a range between 2 $\times 10^{-5}$ and 10^{-4}. Tune stability directly affects the compensation of the driven motion, since the difference between the driven tune and the natural tune is assumed to be constant within a set of measurements. The analytic calculation of the tune error propagation in the β function can be found in Appendix A.2. In the case of Ballistic, the fractional part of the tunes are $\mathrm{Q_x} = 0.28$ and $\mathrm{Q_{x,D}} = 0.268$ and $\mathrm{Q_y} = 0.31$ and $\mathrm{Q_{y,D}} = 0.325$, the relative β-uncertainty is given by:

$$\sigma_{\beta^{\mathrm{A}}_{\mathrm{x}}}\bigg|_{\sigma_Q} \approx \beta^{\mathrm{A,D}}_{\mathrm{x,i}} \times 9.4\sigma_{\mathrm{Q}_x}, \tag{4.16}$$

$$\sigma_{\beta^{\mathrm{A}}_{\mathrm{y}}}\bigg|_{\sigma_Q} \approx \beta^{\mathrm{A,D}}_{\mathrm{y,i}} \times 9.1\sigma_{\mathrm{Q}_y}. \tag{4.17}$$

Equations (4.16) and (4.17) allow to estimate a systematic effect of the tune uncertainty in the β^{A}-error ($\sigma_{\beta^{\mathrm{A}}}$). It can be seen that the tune error $\sigma_{Q_{x,y}}$ gets amplified approximately 9 times in the β^{A}-calculation.

On the other hand, the phase advance and the amplitude uncertainty are estimated during the turn-by-turn measurement analysis, by using single-value-decomposition (SVD) technique. It has been found that for amplitude excitation of approximately a maximum 2 mm peak to peak and for 6600 turns, the error introduced by the ϕ-advance between the AC-dipole and the BPM location, $\phi_{i\Rightarrow\mathrm{AC}}$ in Eq. (4.9), and the amplitude error in the β-function calculation is approximately 0.05% and therefore, these two error-sources have been neglected.

The error introduced by the action calculation $2J_{\mathrm{C}}^{\mathrm{D},\phi}$ will propagate to the β^{A}:

$$\left.\frac{\sigma_{\beta_{x,i}}}{\beta_{x,i}}\right|_{\sigma_{2J_{\mathrm{C}}^{\mathrm{D},\phi}}} = \frac{\sigma_{2J_{\mathrm{C}}^{\mathrm{D},\phi}}}{2J_{\mathrm{C}}^{\mathrm{D},\phi}} + 9.4\sigma_{\mathrm{Q}_x}, \tag{4.18}$$

$$\left.\frac{\sigma_{\beta_{y,i}}}{\beta_{y,i}}\right|_{\sigma_{2J_{\mathrm{C}}^{\mathrm{D},\phi}}} = \frac{\sigma_{2J_{\mathrm{C}}^{\mathrm{D},\phi}}}{2J_{\mathrm{C}}^{\mathrm{D},\phi}} + 9.1\sigma_{\mathrm{Q}_y}. \tag{4.19}$$

The number of turns available for the Fourier analysis is limited by the length of the external excitation. Since the AC-dipole cannot produce longer excitations, the amount of data is increased by exciting the beam a number of times, $\mathrm{N}^{\mathrm{acq.}}$, and by combining the different acquisitions in order to obtain a single β-value per BPM. In case of the β^{A} method, the final β_i^{A} value at a given BPM is calculated as an average over the number of measurements acquired, $\mathrm{N}_{acq.}$:

$$\langle \beta_i^{\mathrm{A}} \rangle = \frac{1}{\mathrm{N}_{\mathrm{acq.}}} \sum_{j=1}^{\mathrm{N}_{\mathrm{acq.}}} \beta_{i,j}^{\mathrm{A}}. \tag{4.20}$$

In this case, the error introduced by the machine fluctuation is given by the standard deviation of the acquisitions β_i^{A}. This standard deviation also cover the random component associated to the tune fluctuations.

$$\sigma_{\beta_i^{\mathrm{A}}}|_{\mathrm{acq}} = \frac{1}{\mathrm{N}_{\mathrm{acq}}} \sqrt{\sum_{j=1}^{\mathrm{N}_{\mathrm{acq}}} (\beta_{i,j}^{\mathrm{A}} - \langle \beta_i^{\mathrm{A}} \rangle)^2}. \tag{4.21}$$

The total β^{A}-error, $\sigma_{\beta_i^{\mathrm{A}}}$, will be therefore given by the combination of two sources of errors:

$$\sigma_{\beta_i^{\mathrm{A}}}|_{\mathrm{tot}} = \sqrt{(\sigma_{\beta_i^{\mathrm{A}}}|_{2J_C^{\mathrm{D},\phi}})^2 + (\sigma_{\beta_i^{\mathrm{A}}}|_{\mathrm{Q}})^2 + (\sigma_{\beta_i^{\mathrm{A}}}|_{\mathrm{acq}})^2}. \tag{4.22}$$

4.1.2 Dispersion measurements

Another optics function that can be used for optics-based-BPM-calibration is the dispersion. The dispersion is measured by taking the average orbit of the turn-by-turn data at each BPM position. Changing the radial steering, results in a change of the closed orbit due to dispersion, $\Delta CO_{x,i}$:

$$\Delta CO_{x,i} = \frac{\Delta p}{p} D_{x,i}. \tag{4.23}$$

Dispersion is then calculated at every BPM by a polynomial fit of the measured closed orbit over various momentum values of $\Delta p/p$. On the other hand, the momentum deviation $\frac{\Delta p}{p}$ is computed by using the dispersion predicted by the MADX model and the closed orbit affected by the calibration factor C_i^{A} as

$$\frac{\Delta p}{p}^{\mathrm{meas}} = \frac{\overline{D^{\mathrm{model}}_{x,i} C^{A}_{x,i} \Delta CO_{x,i}}}{\overline{(D^{\mathrm{model}}_{x,i})^2}} = \overline{C^{\mathrm{A}}} \frac{\Delta p}{p}. \tag{4.24}$$

The $\Delta p/p$ calculation is based on the assumption that the average of the product of the dispersion predicted by the MADX model, times the dispersion-beating ΔD is 0, independently, of the rms β-beating present in the machine. MADX simulations, including different quadrupolar errors, have been performed using Ballistic configuration, obtaining an average value that fluctuates around zero, as shown in Fig. 4.4.

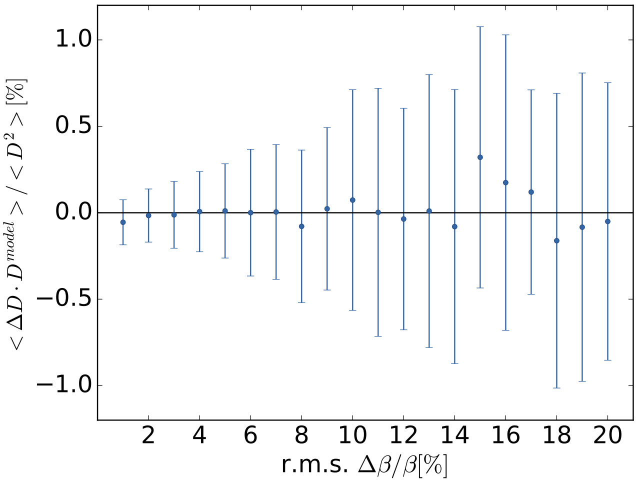

Figure 4.4: Average dispersion-beating times model dispersion as a function of the rms β-beating.

Closed orbit measurement is also affected by the individual BPM calibration factors biasing the dispersion calculation:

$$D^{\mathrm{meas}}_{x,i} = \frac{C^{\mathrm{A}}_{x,i} \Delta CO_{x,i}}{\Delta p/p^{\mathrm{meas}}} \approx \frac{C^{\mathrm{A}}_{i} \Delta CO_{x,i}}{\overline{C^{A}} \Delta p/p}. \tag{4.25}$$

In [58] normalized dispersion is introduced as a calibration independent observable, defined as the ratio $ND_x = \frac{D_x}{\sqrt{\beta_x}}$. The normalized dispersion value can be computed using the weighted arithmetic mean of the ratio $CO^{\mathrm{meas.}}_{x,i}/A^{\mathrm{meas.}}_{x,i}$ over the number of acquisitions, using the relative momentum deviation $\Delta p/p$ as individual weights. The behaviour of the ratio between the ideal average normalized dispersion over the BPMs and measured average normalized dispersion over BPMS, $R_{ND} = \overline{ND^{\mathrm{model}}_{x}}/\overline{ND_x}$, versus the rms beta-beating for many machines with random errors is also studied in [58] concluding that there is no dependency between these two quantities. The maximum deviation of the average ND_x from the design value is below the 1% level. Therefore, it allows to accurately restore unknown global factors in the measurements of ND_x. The horizontal normalized dispersion at a BPM i

$$ND_{x,i} = \frac{1}{\left\langle C^{A}_{x,i} A_{x,i} \right\rangle} \frac{\left\langle R_{ND} |\Delta p/p| C^{\mathrm{A}}_{x,i} \Delta CO_{x,i} \right\rangle}{\langle |\Delta p/p| \rangle}, \tag{4.26}$$

where the average is performed over the number of acquisitions $\mathrm{N_{acq}}$, note that the average normalized dispersion in the vertical plane, $\overline{ND_y}$, is 0 and therefore this measurement is only done in the horizontal plane.

4.1.3 Optics based calibration factors

Optics based calibration factors are computed as the ratio between two different optics measurements, β_i^{ϕ} and β_i^{A} and dispersion D_x and ND_x,

$$C_{\beta,i}^{\mathrm{A}} = \sqrt{\frac{\beta_i^{\mathrm{A}}}{\beta_i^{\phi}}} = \frac{C_i^{\mathrm{A}}}{\sqrt{\overline{(C_{i,\mathrm{ARCS}}^{\mathrm{A}})^2}}}. \tag{4.27}$$

$$C_{D,x,i}^{A} = \frac{D_{x,i}^{\mathrm{meas}}}{ND_{x,i}^{\mathrm{meas}}\sqrt{\beta_i^{\phi}}} = \frac{C_{x,i}^{A}}{\overline{C_x^{A}}}. \tag{4.28}$$

The main limitation of the dispersion method comes from the fact that only the calibration factors in the horizontal plane can be computed since normalized dispersion is only computed in the horizontal plane.

4.2 Ballistic optics

Ballistic optics, the optics used for measuring the BPM calibration factors, is described in this section. In this special optics configuration, the triplet is switched off. This set of magnets located in IR1 and IR5 are common to both beams. Switching off the focusing system presents some challenges for the machine operation that have to be taken into account. The main limitation comes from the large drift generated in the segment between the quadrupoles, leading to large values of the β function in the interaction regions (IR1 and IR5).

Figure 4.5 shows the quadrupolar strength of 2016 (top) and 2017 (bottom) Ballistic optics. Magnets placed to the left of the dotted lines in Fig. 4.5 corresponds to the magnets that are switched off (triplet and Q4). By switching off the quadrupole Q4, the drift region is extended and so, the region of calibration. These extra BPMs that have been calibrated using the latest Ballistic configuration will be useful for the future measurements in HL-LHC since they will be close to the crab cavities [111], which also require tight optics control. In the latest configuration, designed explicitly for optics-based-calibration calculations, the value of the dispersion is not zero in the IR1 and IR5, and therefore can be used as an alternative method for computing the BPM optics-based calibration factors.

Figures 4.6 and 4.7 show the design β function in horizontal and in vertical plane as well as the dispersion in the horizontal plane used in 2016 (top) and 2017 (bottom) in IR1 and IR5.

A specific preparation is required before the start of the optics measurements. In order to minimize the remanent magnetic field in the triplet, a process called degaussing is usually used.

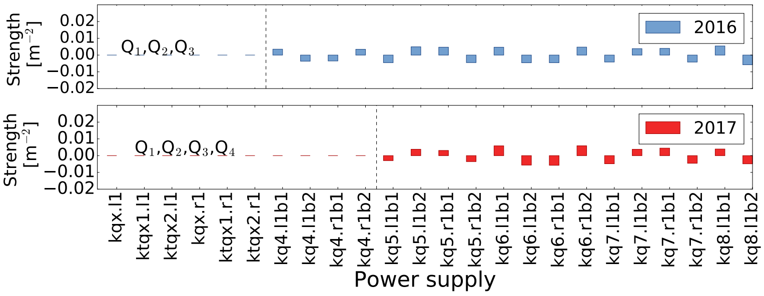

Figure 4.5: Power supplies strength in the IR1 in 2016 (top) and in 2017 (bottom). The IR5 is equivalent.

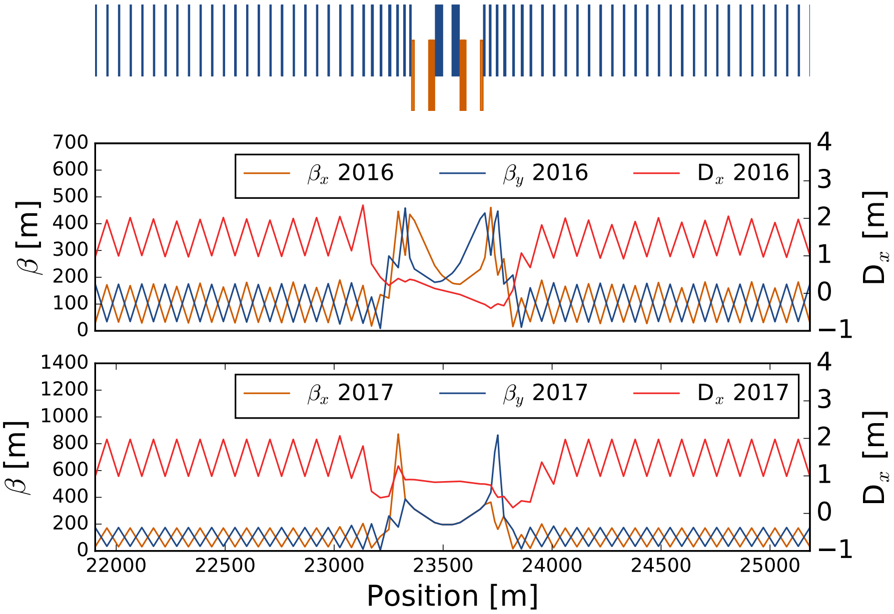

Figure 4.6: Comparison of the horizontal model β, vertical model β function and dispersion for the IR1: top 2016 and bottom 2017 (Beam 1).

This consists of excitation to a very high positive value, followed by progressively decreasing magnitude of the field, while alternating its sign. This procedure was applied to the triplet magnets at the beginning of the measurements to reduce the remaining field, with two limitations. As the primary power converters are single-polarity, the current cycle was only performed on the positive sign and a compromised was found reducing the number of cycles to three, due to the long-time needed for ramping up and down the magnets [11].

Ballistic optics measurements have been performed in three consecutive years: 2015, 2016, 2017. The optics configuration was not the same for all the years. In 2015, due to technical issues, measurements were only performed at injection energy (450 GeV) [11]. Thanks to the promising results obtained in 2015, optics measurements were repeated in 2016 using the same Ballistic configuration, this time at flattop energy.

The main reason for measuring the BPM calibration factors in consecutive years was to evaluate the improvements performed in the BPMs during the yearly shutdown and to have the most recent value of the calibration factors commissioning. During the extended end of the year stop in 2016, several improvements were performed in the BPM electronics regarding minor software

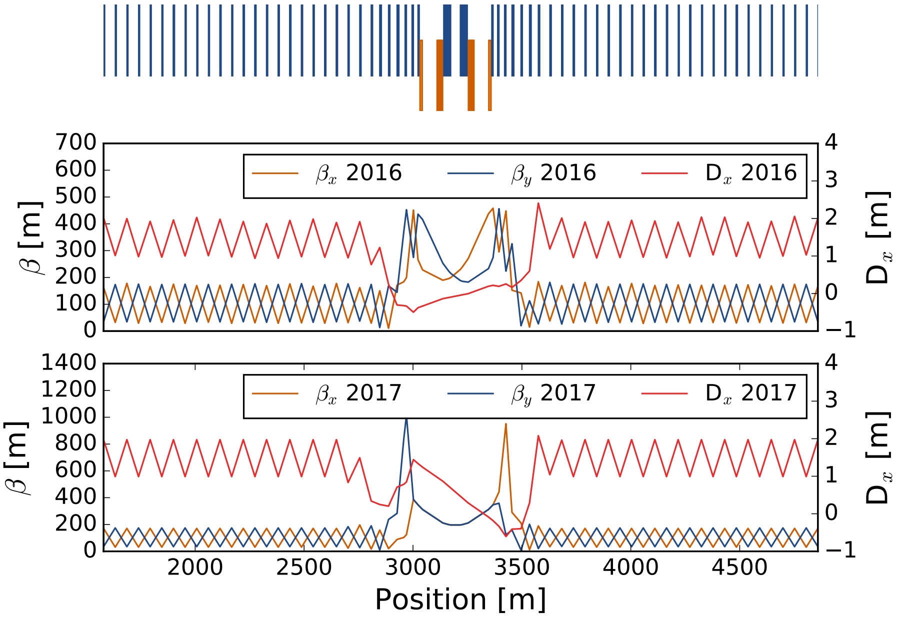

Figure 4.7: Comparison of the horizontal model β, vertical model β function and dispersion for the IR1: top 2016 and bottom 2017 (Beam 2).

and several hardware problems, such as comparator thresholds [112].

Studies presented in this chapter are focused on the calibration factors measured at high-energy in 2016 and 2017 and their application to several different optics measurements during 2017 and 2018.

4.2.1 Ballistic optics corrections

During the last set of measurements performed in 2017, the rms β-beating in the arcs was kept bellow 5% for both planes and beams. On the other hand, it is essential to correct β-beating in the IR in order to have the most accurate values of β^{ϕ} and therefore, accurate values of the calibration factors. Local corrections are based on the analysis of the phase advance propagation in the IR [41]. If a significant deviation is observed in the phase with respect to the model, i.e. phase-beating, the strength of the IR quadrupoles (in this case Q5, Q6 and Q7) are modified in order to compensate this phase advance deviation. Figures 4.8 and 4.9 show the phase advance measured in the IR1 before (blue) and after the corrections (orange) for Beam 1 and Beam 2 respectively.

During normal optics measurement procedure, β function is measured several times for both beams. To compute local or global corrections and secondly to validate the effectiveness of the corrections. After the first measurements, local corrections were implemented in the machine by changing the strength of the quadrupoles Q5 and Q6 in the interaction region 1 with the main aim to decrease local errors of the IR1. Table 4.2 summarizes the local corrections performed in IR1. The effectiveness of the local corrections have been summarized in Tabs. 4.3 and 4.4 RMS β-beating in the interaction region was decreased in IR1 in both beams while β-beating in the arcs remained similar.

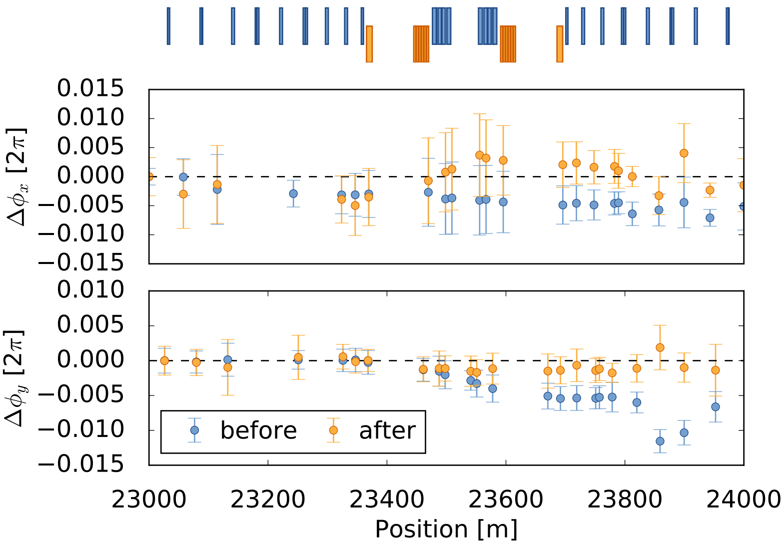

Figure 4.8: Comparison of the phase ($\Delta\phi$) in IR1 measured in 2017 for Beam 1: Horizontal plane (horizontal) and vertical plane (bottom).

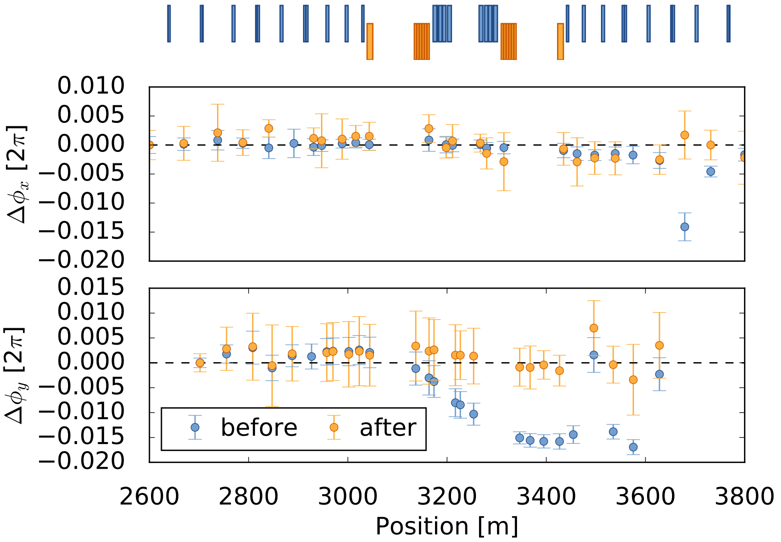

Figure 4.9: Comparison of the phase ($\Delta\phi$) in the IR1 measured in 2017 for Beam 2: Horizontal plane (horizontal) and vertical plane (bottom).

4.2.2 Ballistic optics measurements

Figure 4.10 shows the β function measured using the β^{ϕ} and β^{A} approaches. The schematic of the lattice of the IR is placed in the top of both plots while measurements performed in 2016 and 2017 are shown in the top and bottom figures respectively. A comparison of the horizontal and vertical β function obtained using β^{ϕ} and β^{A} approaches for IR1 and IR5 is shown in Figs. 4.10 and 4.11 respectively. These comparisons are focused on the IR area in between the two Q4 (left and right) in order to see the difference between the two β approaches.

The quadrupolar components due to magnetic imperfections of the MBXW dipoles could also affect the β-function in the interaction region. These errors have been simulated using the measured values from WISE [113] obtaining a negligible deviation of a 0.005%.

Circuit	Δ k (10^{-5} m^{-2})	k nominal (10^{-3} m^{-2})	Correction (%)
kq5.l1b1	-2.3	-2.97	0.77
kq5.l1b2	3.4	3.8	0.90
kq5.r1b1	3.1	3.1	1.0
kq5.r1b2	-2.5	-3.6	0.70
kq6.l1b1	2.0	5.8	0.34
kq6.r1b1	-3.4	-5.7	0.60
kq6.r1b2	3.5	5.9	0.60

Table 4.2: Local corrections implemented in IR1.

	Beam 1		Beam 2	
	Horizontal	Vertical	Horizontal	Vertical
rms $\frac{\Delta\beta}{\beta}$(%)	4.1	4.3	5.1	3.9

Table 4.3: Rms β-beating before local corrections.

As can be seen in Figs. 4.10 and 4.11 the values given by the β^{A} approach are systematically lower than the values given by β^{ϕ}. The discrepancy between the two methods is attributed to a miss-calibration of the BPMs. Beam 1 has been used as an illustrative sample since β^{ϕ} and β^{A} measured in Beam 2 follow the same behaviour

Figure 4.12 shows the measurement of the dispersion function in IR1 in 2017 using calibrated-dependent approach (D_x) and the calibrated-independent method ($ND_x\sqrt{\beta^{\phi}}$). Red dots show the dispersion measurement biased by the calibration factors Eq. (4.25), while blue dots show the calculation of the dispersion function based of the normalized dispersion, Eq. (4.26). Dispersion functions have only been used for computing the calibration factors in Beam 1 since the dispersion function in Beam 2 reaches minimal values inside the IR1 and IR5. For values of dispersion in the vicinity of 0, their associated error-bar fluctuates between 10% and 40%.

Dispersion function in a drift shows a linear dependence with the longitudinal position. A first-order polynomial equation can be fit to measured horizontal dispersion in the BPMs placed within the drift region that is not affected by dipolar fields. The results of a linear fit are illustrated in Figs. 4.12 and 4.13 corresponding to the IR1 and IR5, respectively.

The error bars of the dispersion measurements are dominated by the statistical errors showing that the current accuracy in the dispersion calculation is poorer than the one obtained in the β reconstruction.

	Beam 1		Beam 2	
	Horizontal	Vertical	Horizontal	Vertical
rms $\frac{\Delta\beta}{\beta}$(%)	4.3	3.5	4.8	3.5

Table 4.4: Rms β-beating after local corrections.

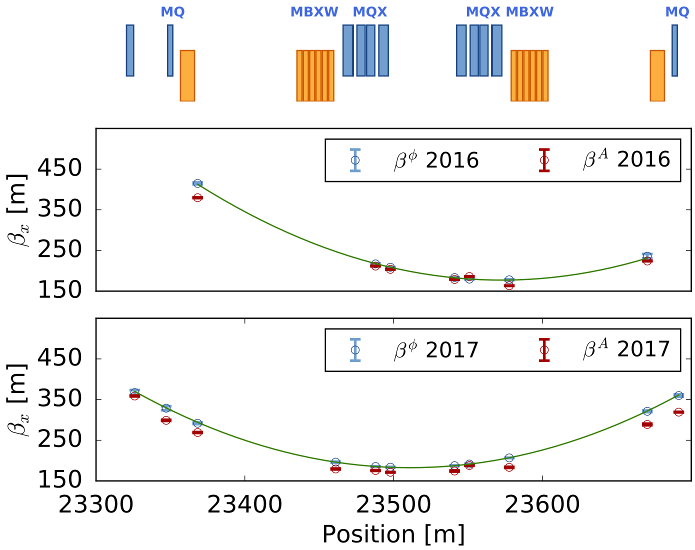

Figure 4.10: Parabolic fit of β^{ϕ} measured in 2016 (top) and 2017 (bottom) in horizontal plane in IR1 Beam 1.

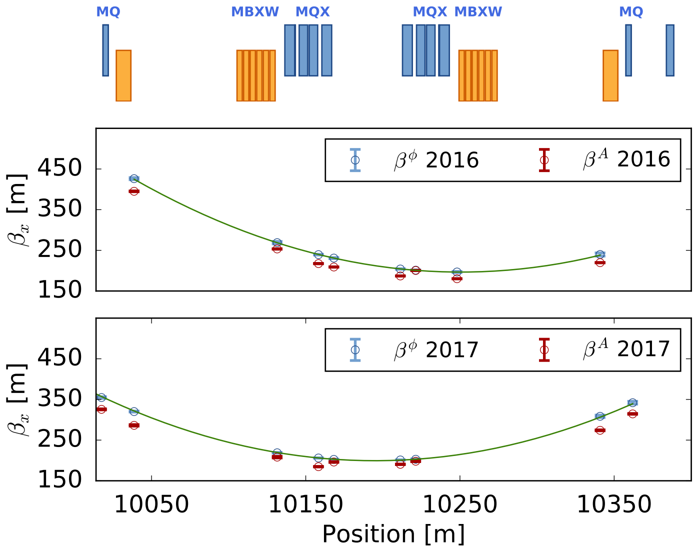

Figure 4.11: Parabolic fit of β^{ϕ} measured in 2016 (top) and 2017 (bottom) in horizontal plane in IR5 Beam 1

4.2.3 Calibration factors 2016 vs 2017

A comparison between the calibration factors calculated in 2016 and 2017 is introduced in this section. This comparison has been separated by IR and plane and it is shown in Figs. 4.14 and 4.15. This comparison is merely illustrative since the improvements performed in the BPMs involving both software and hardware do not allow to have a direct comparison of both measurements. Additionally, a histogram of the calibration factors and their uncertainties for both beams is shown in Figs. 4.16 and 4.17. From Fig. 4.17 it can be observed that the average calibration factor uncertainty is approximately 0.5%.

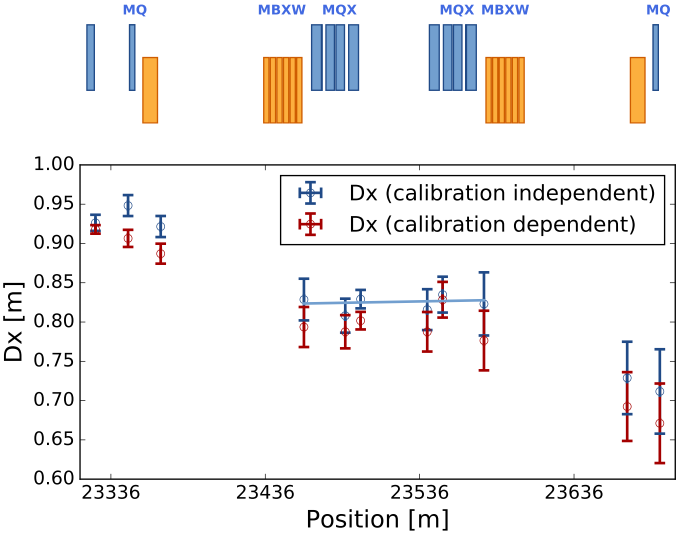

Figure 4.12: Dispersion calculated in 2017 using calibration dependent vs calibration independent approach (IR1, Beam 1).

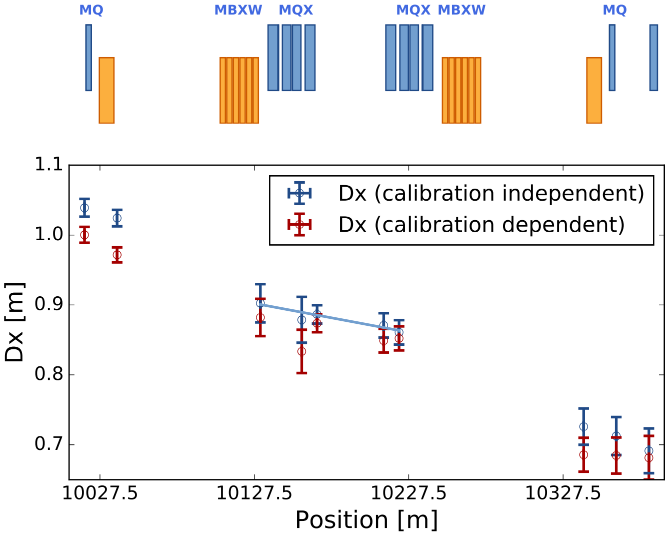

Figure 4.13: Dispersion calculated in 2017 using calibration dependent vs calibration independent approach (IR5, Beam 1).

4.2.4 Calibration factors 2017: β and dispersion.

Figure 4.18 compares the horizontal calibrations factors obtained using the two methods previously described. Each point represents the calibration factor measured at a given BPM using the β method and the dispersion approaches. A linear fit of the calibration factors $C^{\mathrm{A}}_{\beta_x}$ as a function $C^{\mathrm{A}}_{D_x}$, with equation $y = (0.998 \pm 0.002)x$, shows that the values are compatible. Calibration factors $C^{\mathrm{A}}_{\mathrm{D,i}}$ accuracy, fluctuates between 2% and 10% for both planes in Beam 1 while for Beam 2 it reaches values up to 80 % for BPMs placed in areas where the dispersion is close to 0 and therefore they have not been studied in detail. The accuracy of the calibration factors based C^{A}_{β} fluctuates between 0.3% and 1%.

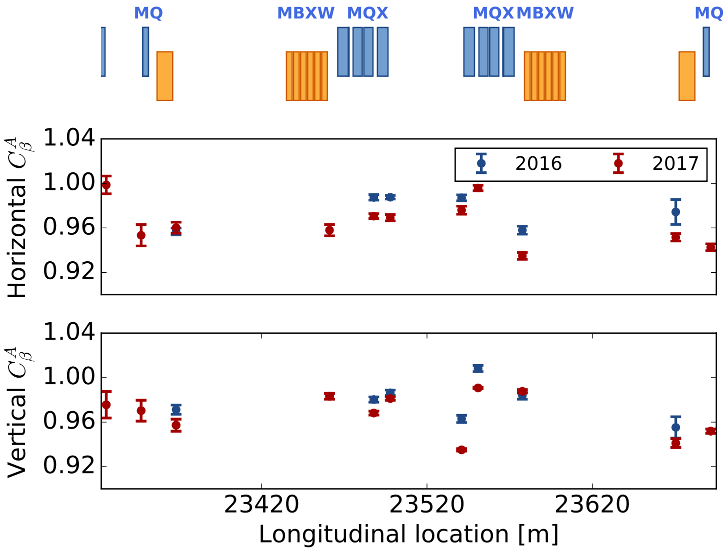

Figure 4.14: Comparison of calibration factors measured at 6.5 TeV in 2016 and 2017 (IP 1, Beam 1).

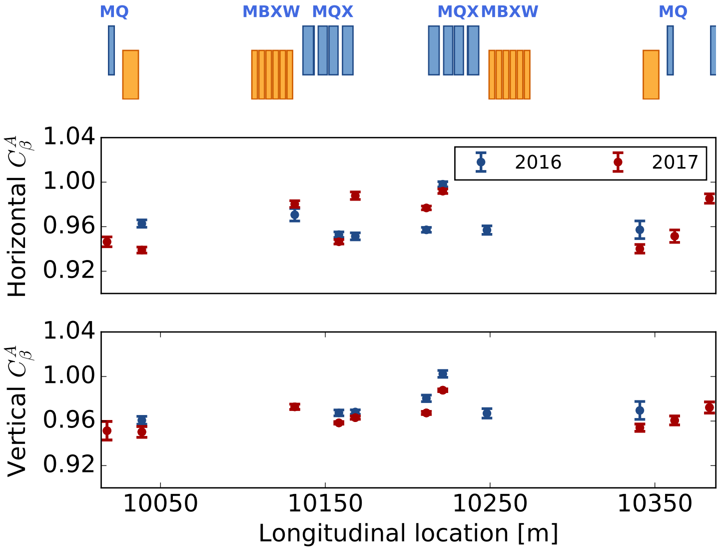

Figure 4.15: Comparison of calibration factors measured at 6.5 TeV in 2016 and 2017 (IP 5, Beam 1) for horizontal (top) and vertical (bottom) planes.

4.3 Applications of the calibration factors to other optics.

Calibrated BPMs could allow obtaining accurate β^* measurements and, in general, the β-function in the interaction regions in the scenarios where the other methods present limitations. Inverse calibration factors are directly applied to the main spectrum line of the turn-by-turn measurements in the frequency domain.

This section summarizes a comparison of the values obtained using the β from amplitude method before and after re-calibrating the BPMs. Different optics configurations that have

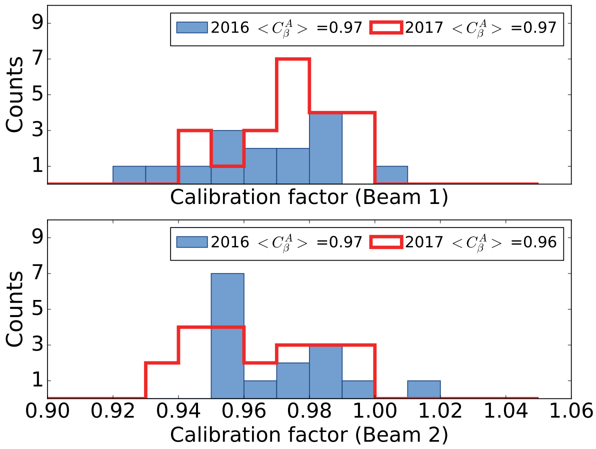

Figure 4.16: Histogram of the calibration factor for Beam 1 and Beam 2 in 2016 and 2017 for horizontal and vertical planes.

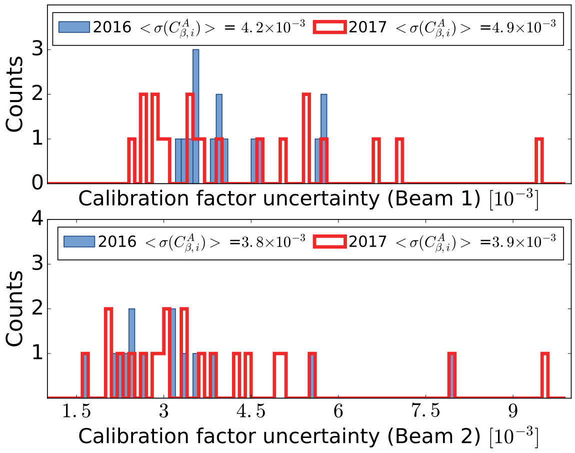

Figure 4.17: Histogram of the calibration factor uncertainty for Beam 1 and Beam 2 in 2016 and 2017 for horizontal (top) and vertical (bottom) planes.

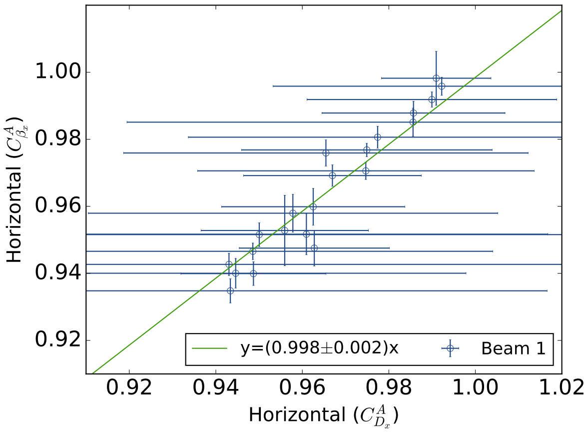

Figure 4.18: Calibration factors using β from amplitude vs calibration factors obtained using dispersion (Beam 1)

been used in order to validate the re-calibration process are listed below, grouped according to the reference value, β^{ϕ} or $\beta^{\text{K-modulation}}$:

- Optics with large β^* ($\beta^* > 1$ m) where β^ϕ can be used as a reference value. These optics are: Flattop, Injection and High-β^* run. Figures 4.19 and 4.20 show a comparison of the β-beating of the β^ϕ and β^{A} measured at the stripline BPMs placed in the IRs 1 and 5 before and after compensated the calibration factors. A summary of the properties of these distributions is presented in Tab. 4.5 average $\left((\beta^{\mathrm{A}} - \beta^\phi)/\beta^\phi\right)$ and its associated spread. From both Figs. 4.19 and 4.20 and Tab. 4.5 it can be observed that the average of the calibration effects has been compensating when applying the calibration factors. Additionally, the spread of the distribution has been slightly reduced after calibrating the BPMs using the calibration factors computed with the Ballistic optics. The theoretical spread of the $\beta^{\mathrm{A}}/\beta^\phi$ ratio has been analytically deduced in Appendix A.4. A larger spread is expected in the non-calibrated ratio since the contribution of the calibration factors in the stripline BPMs is larger than the relative error-bar of the calibration factors computed in Ballistic optics. Additionally, the contribution of the β^ϕ error to the spread affects both the ratio β^A/β^ϕ and $\beta^{\mathrm{A,calibrated}}/\beta^\phi$.

- Low β^* runs where $\beta^{\mathrm{K\text{-}modulation}}$ can be used as a reference value. Several runs of low β^* have been performed in the last two years: β^*= 30 cm and β^*= 40cm in 2017 and β^*= 25 cm and β^*= 30 cm in 2018 [114], [115]. Figures 4.21 and 4.22 show a comparison of the β-beating of the $\beta^{\mathrm{K\text{-}modulation}}$ and β^{A} measured at the stripline BPMs placed in the IRs 1 and 5 before and after compensated the calibration factors. A summary of the properties of these distributions is presented in Tab. 4.6, including the average $\left((\beta^{\mathrm{A}} - \beta^{\mathrm{K\text{-}modulation}})/\beta^{\mathrm{K\text{-}modulation}}\right)$ and its associated spread. In this case the analysis of the spread of the β-beating distribution over the BPMs has not been analytically studied due to the low number of samples. A shift in the average β-beating has also been observed after compensating the calibration factors. Calibration factors has been successfully implemented in Beam 1 where the average β-beating between the two approaches is -0.9 %. Nonetheless, a remaining -4.7% is observed in Beam 2 and will required further investigation.

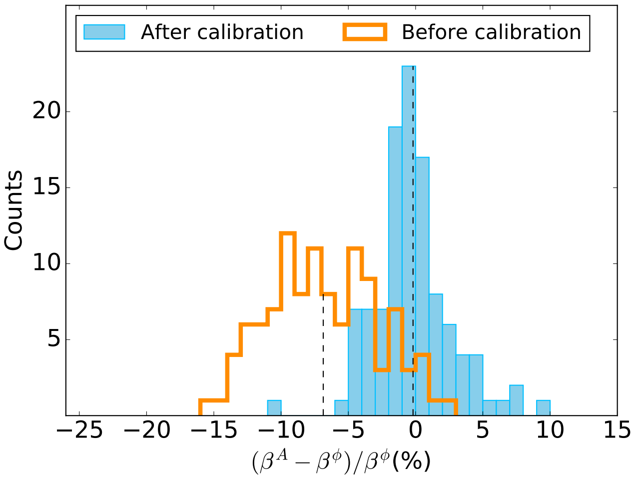

Figure 4.19: Histogram of β-beating before and after calibration using β^ϕ as reference values in horizontal and vertical plane measured in several optics: Injection and Flattop during 2017 and 2018 (Beam 1, horizontal and vertical plane, IR1 and IR5).

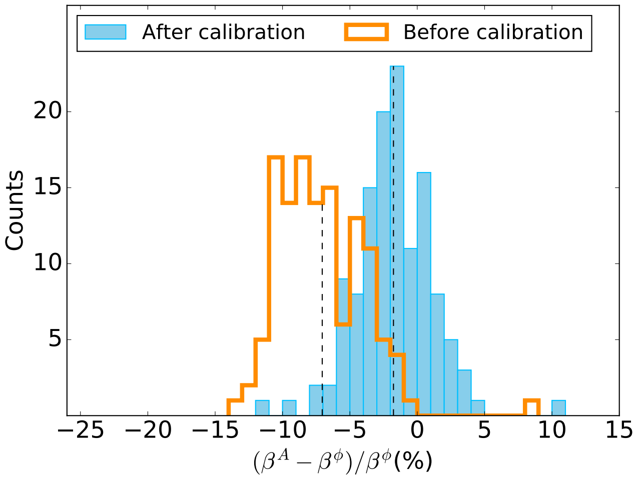

Figure 4.20: Histogram of β-beating before and after calibration before using β^ϕ as reference values in horizontal and vertical plane measured in several optics: Injection and Flattop during 2017 and 2018 (Beam 2, horizontal and vertical plane, IR1 and IR5).

Table 4.5: Summary of the main parameters associated to the distributions $\left(\beta^{\rm A} - \beta^\phi\right)/\beta^\phi$ and $\left(\beta^{\rm A,cal} - \beta^\phi\right)/\beta^\phi$.

	Not calibrated		Calibrated	
	Beam 1	Beam 2	Beam 1	Beam 2
$\overline{\left(\beta^{\rm A,cal} - \beta^\phi\right)/\beta^\phi}$ (%)	-6.9	-7.1	-0.2	-1.8
$\sigma\left(\beta^{\rm A,cal} - \beta^\phi\right)/\beta^\phi$ (%)	4.0	3.1	2.9	2.9

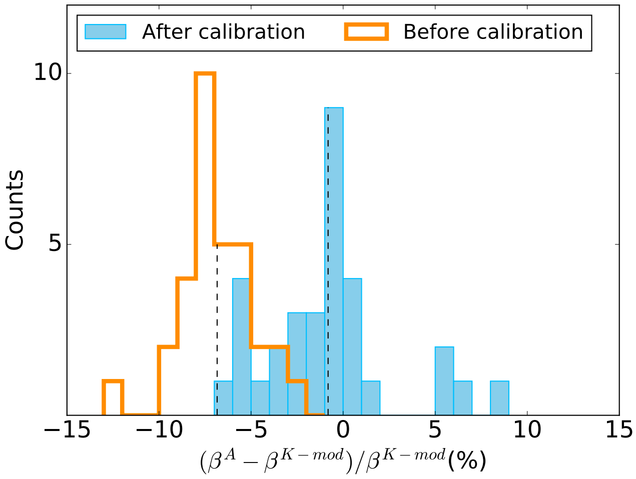

Figure 4.21: Histogram of β-beating before and after calibration before using $\beta^{\text{K-modulation}}$ as reference values (Beam 1).

4.4 Conclusions

BPM calibration factors have been computed for the first time using measured optics functions. This method, denoted as optics-measurement-based BPM calibration, is based on the analysis of two different optics functions: β-function and dispersion. A dedicated optics configuration, known as Ballistic optics, has been developed for these studies. In this optics, a drift space

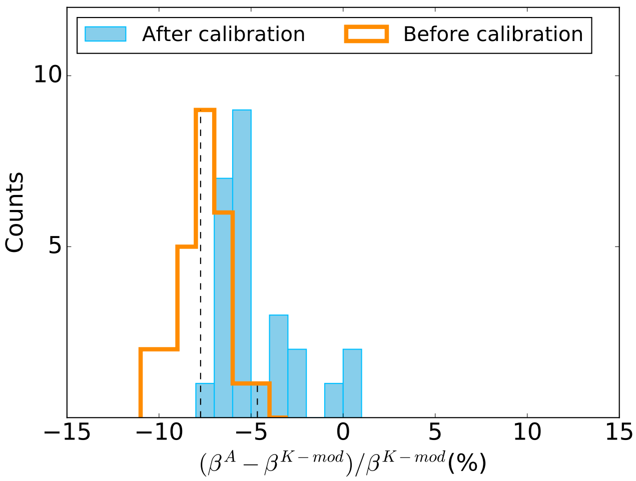

Figure 4.22: Histogram of β-beating before and after calibration before using $\beta^{\text{K-modulation}}$ as reference values (Beam 2).

Table 4.6: Summary of the main parameters associated to the distributions $\left(\beta^{\text{A}} - \beta^{\text{K-mod}}\right)/\beta^{\text{K-mod}}$ and $\left(\beta^{\text{A,cal}} - \beta^{\text{K-mod}}\right)/\beta^{\text{K-mod}}$.

	Not calibrated		Calibrated	
	Beam 1	Beam 2	Beam 1	Beam 2
$\left(\beta^{\text{A,cal}} - \beta^{\text{K-mod}}\right)/\beta^{\text{K-mod}}$ (%)	-6.8	-7.8	-0.9	-4.7
$\sigma\left(\beta^{\text{A,cal}} - \beta^{\text{K-mod}}\right)/\beta^{\text{K-mod}}$ (%)	1.9	1.4	3.5	2.2

is generated in the vicinity of the IP, allowing to measure the β-function from phase with a precision of about 0.5%. This achieved precision on β-function has allowed computing the BPM calibration factors by comparing β^{A} to β^{ϕ} with an average uncertainty in the sub-per cent level. The promising results obtained in 2016, in terms of BPM accuracy and uncertainty achieved, motivated the further development of the Ballistic configuration. In 2017, the drift space was extended by switching off the Q4 quadrupoles and, at the same time, by not matching the dipsersion function to zero in the IR1 and IR5. These two developments allowed to increase the range of BPMs being calibrated and to incorporate dispersion function in the optics-measurement-based calibration approach.

Several optics configurations have been analyzed in order to estimate the impact of BPM recalibration on the β^{A} approach. The main characteristic of the selected optics is the accuracy of the β-function in some stripline BPMs placed in IR1 and IR5; measured either using β^{ϕ} or $\beta^{\text{K-modulation}}$ approach. It has been observed that the β-beating with respect to the β from phase, $(\beta^{\text{A}} - \beta^{\phi})/\beta^{\phi}$, is reduced on average a 6% when BPMs are re-calibrated using the optics-measurement-based approach. If $\beta^{\text{K-modulation}}$ is used as a reference value, the measured β-beating $(\beta^{\text{A}} - \beta^{\text{K-modulation}})/\beta^{\text{K-modulation}}$ decreases on 6% for Beam 1, and a 3% for Beam 2.

Additionally, calibration factors have also been computed using the ratio $\sqrt{\beta^{\text{A}}/\beta^{\phi}}$ for different optics and then averaging over them, aiming to justify the development of an optics configuration dedicated exclusively to the calibration factors calculation. The associated error-bar has been computed as the standard deviation of the calibration factors over the optics measured. It can be observed in Figs. 4.23 and 4.24 that the error-bar obtained using a dedicated optics for the computation of the calibration factors is on average three times smaller than averaging the calibration factors over a set of optics.

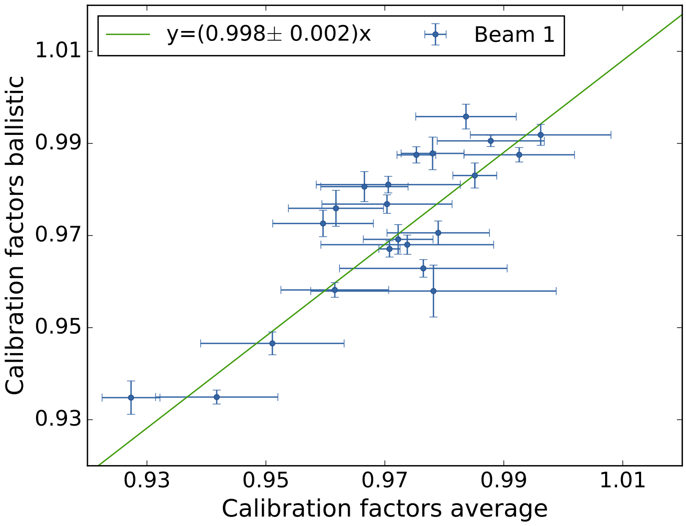

Figure 4.23: Average calibration factor measured for different optics vs calibration factors measured using Ballistic optics (Horizontal and vertical planes, Beam 1).

.

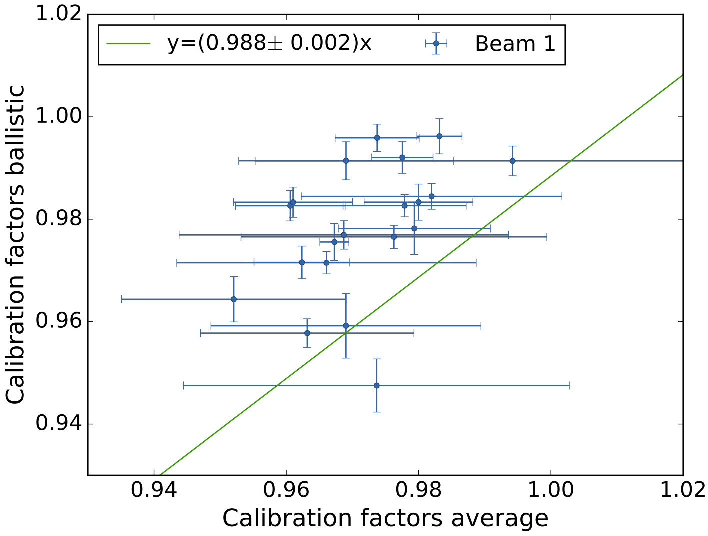

Figure 4.24: Average calibration factor measured for different optics vs calibration factors measured using Ballistic optics (Horizontal and vertical planes, Beam 2).

.

This proves that the β^{ϕ} precision is the main limitation in the calibration factor calculation. Nonetheless, currently, the possible dependency of the calibration factors overtime is not included in the Ballistic error-bar. This will be addressed on LHC run 3 and on view of the Hl-LHC. The large error-bars associated with the dispersion measurements -in contrast to the sub-per cent error-bars associated to the β-function- propagate directly to the calibration factor calculations affecting the accuracy of the measurements. Yet the agreement between the calibration factors obtained using β-function has been used as a validation for the optics-measurement-based calibration approach. A more in-depth study of the dispersion error-bar should be further performed before re-calibrating the BPMs using this technique.

Chapter 5

High-β^* runs in LHC as test-bench of the calibration factors calculation

5.1 LHC special optics studies as test bed of β^{A} approach.

To be able to validate the effectiveness of compensating the optics measurements based BPM recalibration, it is necessary to have an accurate and precise β^{ϕ} function.

Nonetheless, not all optics can be used to evaluate the mitigation of the calibration factors and optics configuration where β-function can be accurately measured in the IRs using β^{ϕ} are required. A comparison of the different relative β^{ϕ} error-bars at different [4] β^*-values is shown in Fig. 5.1 both for the button BPMs placed in the arcs and for the stripline BPMs placed in the IRs. Button BPMs show an β^{ϕ} average error-bar of 0.9% with small differences between the different optics analyzed. On the other hand, the β^{ϕ} errorbar measured at the stripline BPM location fluctuates between 2% and 10%.

Alternatively, $\beta^{\text{K-modulation}}$ could be used, but this approach will only provide information about the BPMs placed near the IPs.

During the second run of the LHC, dedicated time was allocated for machine development studies. These studies covered a broad range of different topics, including the commissioning of new optics developed with different aims.

In 2016, two optics with unusual β^* values, designed for specific physics purposes were commissioned: Van der Meer optics used for wire scanners calibration and High-β^* [116] used for forward high energy physics studies. In 2017, forward physics studies were further developed and a new optics configuration was designed and commissioned at a lower energy, 450 GeV and with a smaller β^* value. It was found that in those optics, β-function could be measured with less than 3% error-bar in the IRs, while in optics dedicated to high energy physics studies, characterized for their low β^* values, the β^{ϕ} measured relative error-bar at the IP can reach values up to 18%. This chapter summarizes the optics measurements performed in 2016 and 2017 as part of the commissioning of the high-β^* optics. Van-der-Meer optics has also been

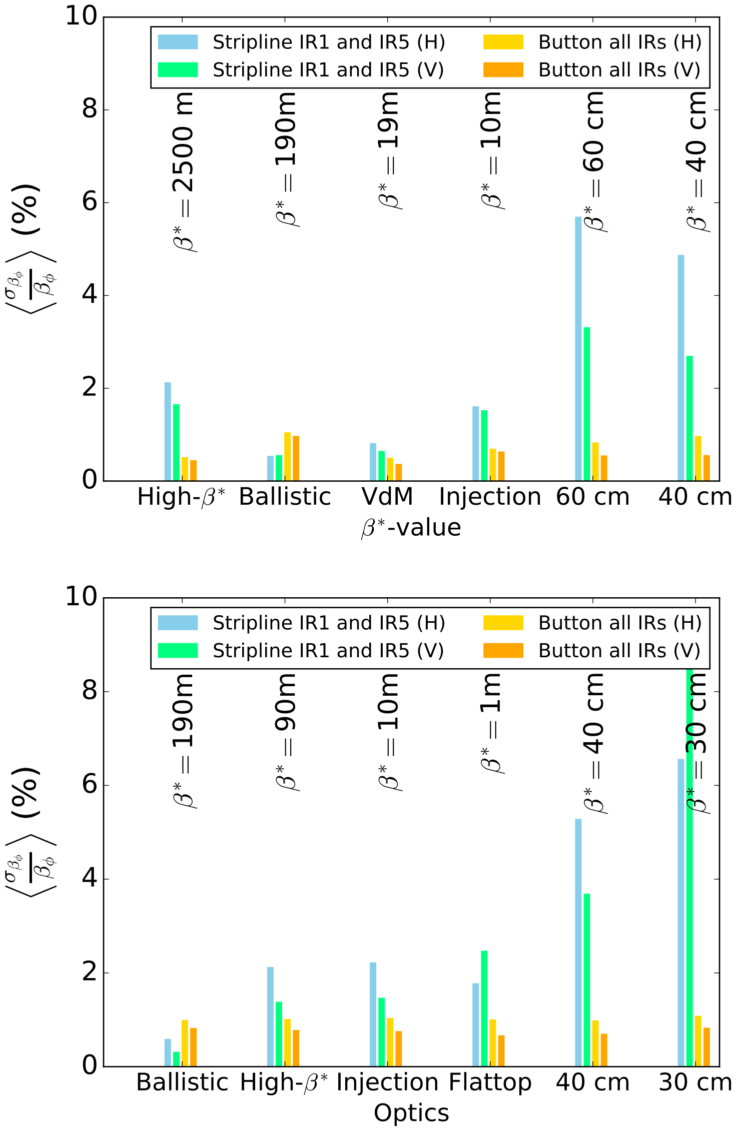

Figure 5.1: Relative β^ϕ error bar measured for different optics in Beam 1: 2016 (top), 2017 (bottom).

used for validation of the calibration factors, results obtained during the commissioning of this optics are described in detail in [117].

5.2 High-β^* optics at 6.5 TeV

5.2.1 Introduction

The β^* determines the physics reach of the experiment; runs with high β^* (from 90 meters to 2.5 km) are characterized by low beam divergence at the IP allowing for precise scattering angle measurements [63, 118]. The main goal of high-β^* is to determine the absolute luminosity in ATLAS and CMS, but also other physics studies are foreseen, such as measuring the total proton-proton cross-section, measuring elastic scattering parameters and diffractive studies.

Roman pot (RP) are near-beam telescopes in charge of the tracks reconstruction of scattered protons, and they are key elements in the high-β^* physics run. Figure 5.2 illustrates the different elements placed on the right side of IR1. As can be seen, an RP station is composed of two units per beam separated by a distance of about 5 meters. Considering Beam1 direction as a reference, RPs are placed right of IPs (IP1 and IP5) for Beam1 and left of IPs for Beam2.

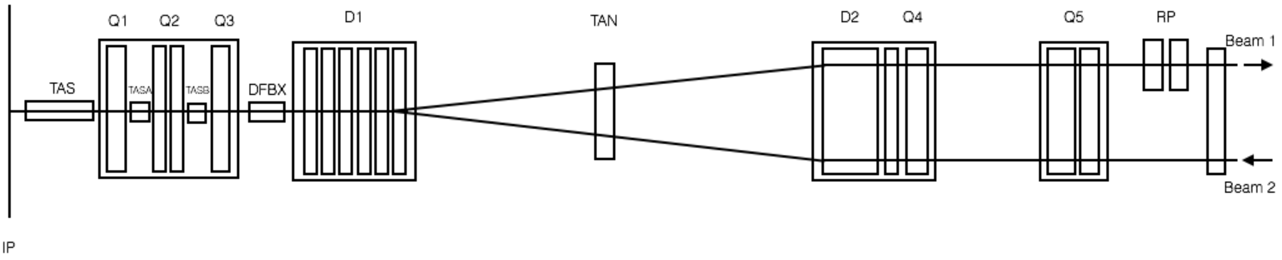

Figure 5.2: Schematic layout of an interaction region.

Proton kinematics at IPs can be reconstructed from position and angles measured by the RP detectors.

Before being detected, the protons' trajectories between the IP and the RP are influenced by the magnetic field of the accelerator lattice. The trajectory of protons produced with transverse positions (x*, y*) and angles (Θ_x^*, Θ_y^*) at the interaction point is described approximately by: $\vec{d}(s) = T(s) \cdot \vec{d^*}$ where $\vec{d} = (x, \Theta_x, y, \Theta_y, \Delta p/p)^T$, $\vec{d^*}$ is the initial coordinates at the IP and T is the transport matrix, which describes the proton transport,

$$T = \begin{bmatrix} v_\mathrm{x} & L_\mathrm{x} & 0 & 0 & D_\mathrm{x} \\ \frac{dv_\mathrm{x}}{ds} & \frac{dL_\mathrm{x}}{ds} & 0 & 0 & \frac{dD_\mathrm{x}}{ds} \\ 0 & 0 & v_\mathrm{y} & L_\mathrm{y} & D_\mathrm{y} \\ 0 & 0 & \frac{dv_\mathrm{y}}{ds} & \frac{dL_\mathrm{y}}{ds} & \frac{dD_\mathrm{y}}{ds} \end{bmatrix}$$

This matrix is defined by the optical functions. The horizontal and vertical magnifications are given by $v_{x,y} = \sqrt{\beta_{x,y}/\beta^*_{x,y}} \cos \Delta\mu_{x,y}$ and the effective lengths $L_{x,y} = \sqrt{\beta_{x,y}/\beta^*_{x,y}} \sin \Delta\mu_{x,y}$

Transfer matrix also depends on horizontal and vertical dispersion (D$_x$ and D$_y$). In order to precisely reconstruct the scattering kinematics, an accurate model of proton transport is indispensable. The LHC is subject to additional imperfections, which alter the transport matrix. These imperfections lead to changes in different parameters: phase advance between the elements μ, β function, dispersion and tune errors, and consequently in the transport matrix T. Therefore, the kinematics of elastically scattered protons in the IR can be reconstructed by measuring the phase advance between the IP and the RP, the $\beta_\mathrm{x,y}$ at the RP and the $\beta_\mathrm{x,y}$ at the IP (β^*). If the phase advance $\mu_{x,\mathrm{IP}\rightarrow\mathrm{RP}}$ is equal to π in the horizontal plane particles will pass through the RP without being detected. This limitation can also be observed in the effective lengths calculations since the sinusoidal term vanishes, giving $L_{x,y} = 0$. A small change in the phase advance, a consequence of quadrupolar strength modifications, can be crucial for the kinetic measurements as can be seen in Fig. 5.3.

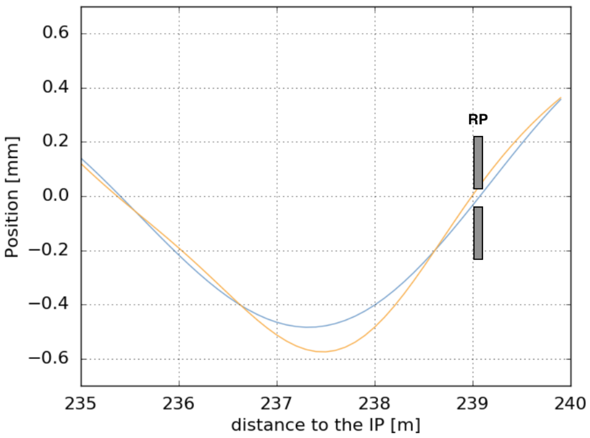

Figure 5.3: Particle trajectory between IP and RP with different phase advance.

High β^* optics have been developed since many years [119], to measure proton-proton scattering angles down to the microradian level. During the high β^* run in 2016 a maximum value of β^* equal to 2500 meters was reached. From an operational point of view, the de-squeezing process can be subdivided into two regions: high-β^* (60, 90 and 500 m) physics and very high β^* ($>$ 1000 m) [120]. De-squeeze has to be done by making several steps during the process. High-β^* runs were already done in previous years: in 2015, the maximum β^* reached was 90 m while in 2012, a β^* of 1000 m was used [121, 119]. The quality of the optics was assessed during the first session of measurements where the conditions imposed by the ALFA and TOTEM experiments were verified. After analyzing the first of measurements, some modifications were done in the quadrupolar configurations. The purpose of this change in the phase is to avoid a phase advance $\mu_{x,\mathrm{IP}\to\mathrm{RP}}$ of 180°, illustrated in Fig.5.3. This modification makes Eq. (5.2.1) different from zero, leading to a better reconstruction of the position and angle and the IP. The goal of the measurements performed during the second session was, therefore, to evaluate the phase advance modification between the interaction point and the roman pots. Section 5.2.4 presents the procedure followed when performing the AC-dipole measurements, as well as an issue with the AC-Dipole power supply when measuring at $\beta^* = 60$ m. Section 5.2.5 presents the optics measurements performed at different β^* values: 60, 90 and 500 m. Section 5.2.6 presents the optics measurements performed during the de-squeezing process, as well as the corrections made at $\beta^* = 1.7$ km. In Section 5.2.7 the results of the implementation of global corrections at maximum β^* are shown. This section also covers the observations from off-momentum measurements. Section 5.2.9 analyzes the measured β-function across the accelerator obtained using β^{ϕ},β^{A} and β^{A} after BPM re-calibration. Finally, conclusions drawn from those two set of measurements are presented in Section 5.2.12.

5.2.2 Summary of optics measurements and corrections

The de-squeeze process started at $\beta^* = 11$ m and ended at β^*= 2500 m, taking some additional measurements at different β^*: 60 m, 90 m, 500 m and 1700 m to control the β-beating evolution during the de-squeeze. During the first steps, β-beating evolution was well controlled without applying corrections. At $\beta^* = 1700$ m coupling and normal quadrupole corrections were cal-

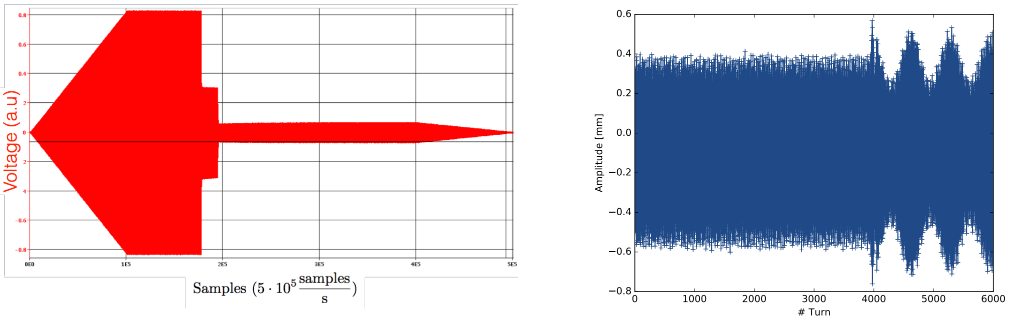

(a) AC-Dipole powering function vs time

(b) Analysis of TbT excitation using AC-dipole with different number of turns

Figure 5.4: AC-dipole failure detected during measurements performed at $\beta^* = 60$ m.

culated and implemented in the interaction regions (IRs) 1 and 5. Finally, global corrections were calculated and applied at $\beta^* = 2500$ m.

5.2.3 Optics measurements and corrections during the de-squeezing

5.2.4 AC-dipole Security switching off system

For optics measurements, the beam is usually excited using an external periodic excitation source, the AC-dipole. Turn-by-turn measurements give the evolution of the beam centroid position recorded at the (BPM). Turn-by-turn position data of excited motion allows prompt measurements of optical parameters. The beam can be driven to a steady coherent oscillation by slowly ramping up the amplitude of an AC dipole oscillating field at a frequency in the vicinity of the beam betatron frequency [48, 89, 90, 91, 92]. All measurements, in both sessions, were performed using the AC dipole system to excite oscillations of the beams [122]. The amplitude of the driven oscillations depends on the AC-dipole voltage, frequency and strength. The amplitude of kicks applied during beam dynamics measurements are typically increased gradually to a sufficient magnitude while monitoring the beam losses. The magnitude of the AC dipole kicks is normalized by the maximum voltage. Relative value of the kick strength depends on the beam energy and has to be adjusted while increasing the energy. When measuring at top energy, the starting voltage is around a 25% of the maximum voltage, and it is increased until the peak to peak value of the oscillations reaches a value of approximately 2 mm in the arc. This amplitude is reached usually at a 70% of the maximum voltage for a tune separation of -0.012 in the horizontal plane and +0.015 units in the vertical plane. During the first optics measurements at $\beta^* = 60$ m, an abrupt drop in kick amplitude during AC-dipole flattop was shown when kicking above 50%, Fig. 5.4a. That problem caused a substantial blowup of the horizontal Beam 1 emittance, as the motion became free and it was not adiabatically ramped down [98]. In order to avoid this power drop in the middle of the measurements, the AC-dipole maximum voltage was reduced. Trying to compensate the drop in the amplitude oscillations horizontal AC-dipole tune in Beam 1 was moved closer to the natural tunes, $\Delta Q_x = -0.009$. Figure 5.4b illustrates the impact of the AC dipole on the turn-by-turn data.

5.2.5 Optics measurements at 60 m, 90 m and 500 m

Three optics measurements were performed in the first part of the de-squeeze in order to evaluate the evolution of the optics errors, and therefore avoid a possible increase of the β-beating. Table 5.1 summarizes the $\frac{\Delta\beta}{\beta}$ rms, in horizontal and vertical planes, at the different steps of the de-squeeze process. Figures 5.5a and 5.5b show the β-beating as a function of the position for Beam 1 and Beam 2 respectively.

	Beam 1						**Beam 2**					
	Horizontal			**Vertical**			**Horizontal**			**Vertical**		
β^* [m]	60	90	500	60	90	500	60	90	500	60	90	500
$\frac{\Delta\beta}{\beta}$ rms (%)	3.4	2.7	3.7	6.0	5.6	2.4	2.8	1.2	1.8	5.5	5.1	5.0

Table 5.1: $\frac{\Delta\beta}{\beta}$ rms values at different steps of the de-squeeze process for Beam 1 and Beam 2, before corrections.

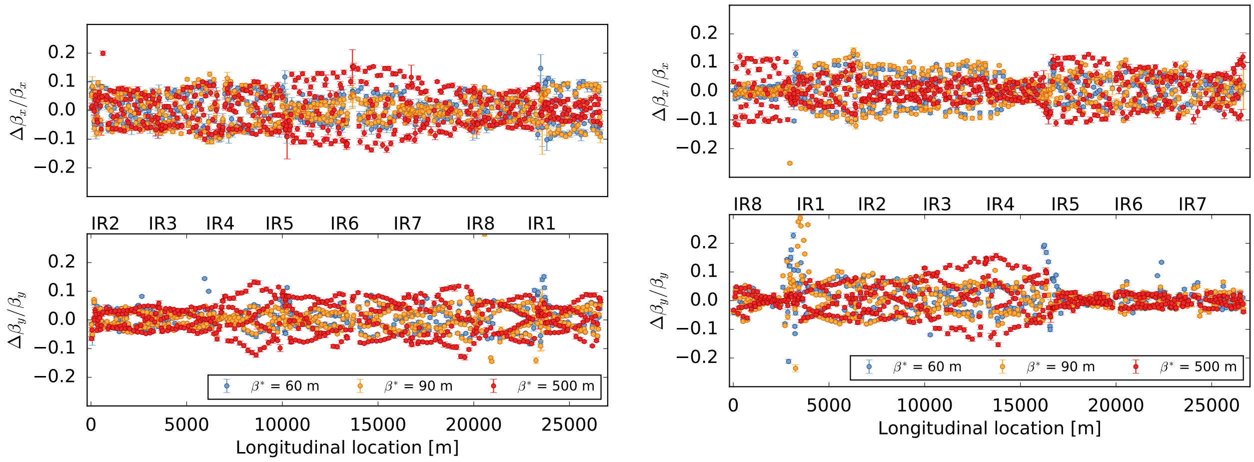

(a) Beam 1.

(b) Beam 2.

Figure 5.5: β-beating during the de-squeeze process at 60 m, 90 m and 500 m β^* before corrections.

5.2.6 Optics measurements and corrections at 1.7 km

While de-squeezing to $\beta^* = 1.7$ km, a large coupling increase was observed from the continuous measurement of coupling by the Base-Band Tune system (BBQ), Fig. 5.6. Turn by turn data was measured and analyzed in order to compute the coupling corrections. The coupling corrections use skew quadrupoles located in IR1 and are summarized in Tab. 5.2.

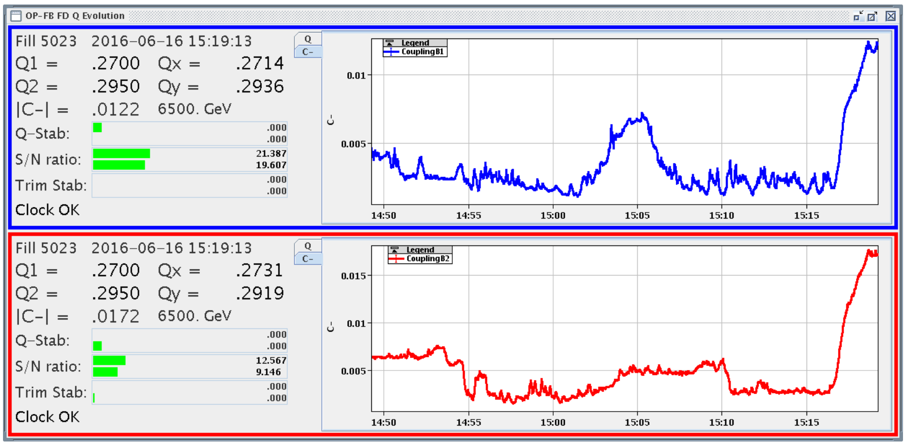

Fill 5023 2016-06-16 15:19:13
Q1 = .2700 Qx = .2714
Q2 = .2950 Qy = .2936
|C-| = .0122 6500. GeV
Q-Stab: .000 .000
S/N ratio: 21.387 19.607
Trim Stab: .000 .000
Clock OK

Fill 5023 2016-06-16 15:19:13
Q1 = .2700 Qx = .2731
Q2 = .2950 Qy = .2919
|C-| = .0172 6500. GeV
Q-Stab: .000 .000
S/N ratio: 12.567 9.146
Trim Stab: .000 .000
Clock OK

Figure 5.6: Increase of coupling after de-squeeze to 1.7 km as measured by BBQ.

Corrector	Strength [m^{-2}]
kqsx3.r1	-4.7 $\cdot 10^{-3}$
kqsx3.l1	-4.7 $\cdot 10^{-3}$

Table 5.2: Local corrections implemented at β^* 1.7 km.

A comparison of coupling before and after corrections can be seen in Figs. 5.7a and 5.7b in order to validate the effectiveness of the coupling corrections.

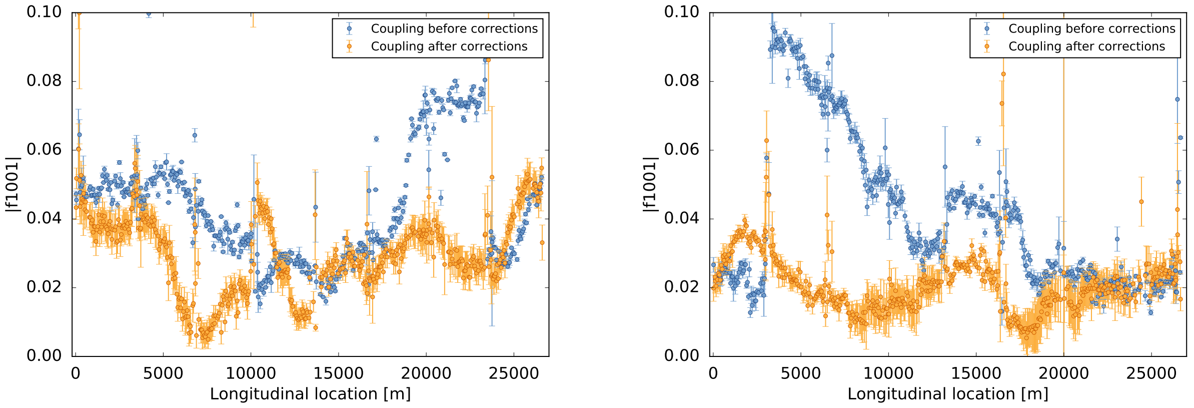

(a) Beam 1.

(b) Beam 2.

Figure 5.7: Coupling resonance terms before and after corrections at β^*=1.7 km.

The required correction strength is computed from the measured β-beating and dispersion. The first local corrections in the de-squeeze process were done at $\beta^* = 1.7$ km. A first guess of the corrections was taken from the local corrections implemented during the nominal optics commissioning in 2016 [105], shown in Tab. 5.3. Nevertheless, it was found that the triplet errors were not the same in the high-β^* and nominal optics. A summary of local corrections computed and applied into the machine are shown in Tab. 5.4. This table also summarizes the relative changes in $\Delta\, \vec{k}_1(\%)$ with respect to the nominal value.

MAD-X variable	Design magnet k_1[10^{-3} m^{-2}]	Δk_1 [10^{-5} m^{-2}]	Correction (%)
ktqx2.l1	-8.73	+0.65	-0.07
ktqx2.r1	8.73	-1.0	-0.11
ktqx2.l5	-8.73	0.27	-0.31
ktqx2.r5	8.73	1.48	0.17
ktqx1.l5	8.73	-2	0.23
ktqx1.r5	-8.73	2	0.23

Table 5.3: Local corrections applied at nominal optics.

MAD-X variable	Design magnet $\vec{k}_1$[10^{-3} m^{-2}]	$\Delta\vec{k}_1$ [10^{-5} m^{-2}]	Correction (%)
ktqx2.r1	-4.82	-1.4	0.29
ktqx2.l1	4.82	+1.4	0.29
ktqx2.r5	-4.82	-0.63	0.13
ktqx2.l5	4.82	+1.24	0.26

Table 5.4: Local corrections applied at β^* 1.7 km.

The effectiveness of the corrections has been evaluated by comparing the β-beating around the ring before and after the corrections, Figs. 5.8a and 5.8b. An overall reduction in β-beating can be seen for both beams in both planes. This decrease is especially remarkable in between IR5 and IR1 in Beam 1 horizontal and in between IR1 and IR5 for beam 2 in both planes. On the other hand, a summary of rms β-beating is showed in Tab. 5.5

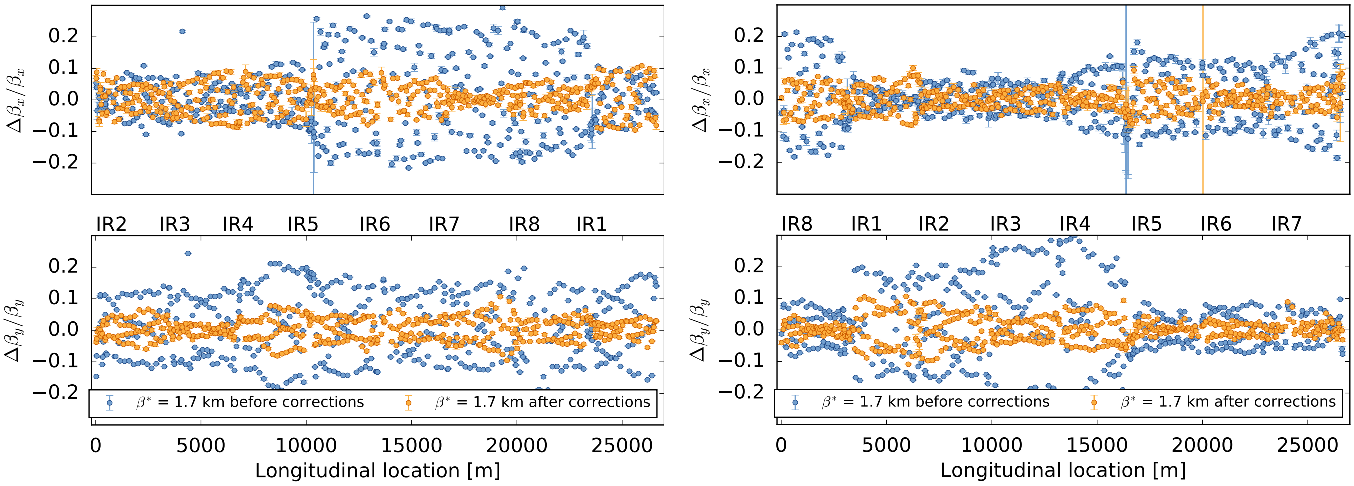

(a) Beam 1.

(b) Beam 2.

Figure 5.8: β-beating before and after corrections at β^*=1.7 km.

	Beam 1				**Beam 2**			
	Before local corr.		**After local corr.**		**Before local corr.**		**After local corr.**	
	Hor.	Ver.	Hor.	Ver.	Hor.	Ver.	Hor.	Ver.
rms $\frac{\Delta\beta}{\beta}$(%)	13.7	11.9	4.6	3.4	8.2	13.2	3.5	3.8

Table 5.5: β-beating rms before and after local corrections at β^*=1.7 km.

5.2.7 Optics measurements and corrections at 2.5 km

Measurements conducted for β^*-beating, coupling, dispersion and β^* at the end of the desqueeze process are discussed in this section.

As mentioned in the introduction, high β^* measurements were made twice in 2016 with two different aims. The objective of the first measurement was to commission the optics while the goal of the second measurement was to validate the settings modifications done in IP1. The quadrupolar strength configuration was modified with the aim of moving away the phase advance from 180° and therefore avoid having $\sin\mu_{\mathrm{x,IP}\to\mathrm{RP}} = 0$. The strengths of the power supplies placed in IR1 controlling both common and separate quadrupoles have been redefined to achieve this objective.

5.2.8 Measurements and global corrections

Global corrections were calculated during the first session of high-β^* optics measurements. Global corrections have been divided in two plots: MQT in Fig. 5.9 and MQM and MQL in Fig. 5.10. Both plots show the magnitude and the sign of the absolute change of the quadrupolar strength for both beams. Plots have been subdivided into the correspondent arcs labeled from IR5 to IR8 to have a better estimation of the correction strength in each arc of the LHC.

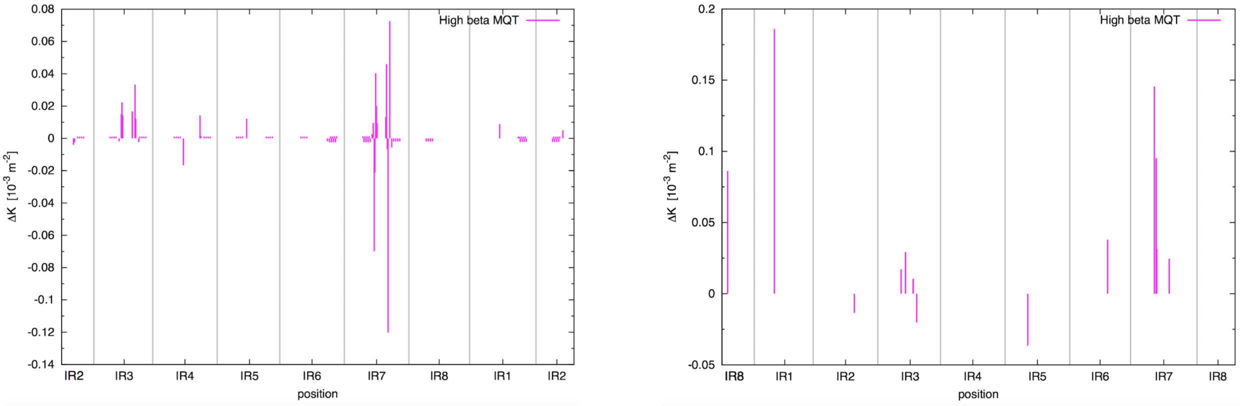

Figure 5.9: Global corrections applied in the MQT magnets (Beam 1 left and beam 2 right).

		Beam 1			**Beam 2**		
		Before global corr.	**After global corr.**		**Before global corr.**	**After global corr.**	
		June	June	August	June	June	August
$\frac{\Delta\beta}{\beta}$(%)	max	10 ± 2	15 ± 7	12.9 ± 0.7	10 ± 1	9 ± 0.6	12.9 ± 0.7
	rms	4.3	1.9	2.8	3.6	2.3	1.22

Table 5.6: rms and maximum values for the horizontal β-beating for both beams before and after global corrections.

		Beam 1			**Beam 2**		
		Before global corr.	**After global corr.**		**Before global corr.**	**After global corr.**	
		June	June	August	June	June	August
$\frac{\Delta\beta}{\beta}$(%)	max	10 ± 1	6.8 ± 0.4	6.8 ± 0.6	7.4 ± 0.3	3.4 ± 0.1	6.8 ± 0.6
	rms	3.4	2.7	2.4	2.8	1.2	1.8

Table 5.7: rms and maximum values for the vertical β-beating for both beams before and after global corrections.

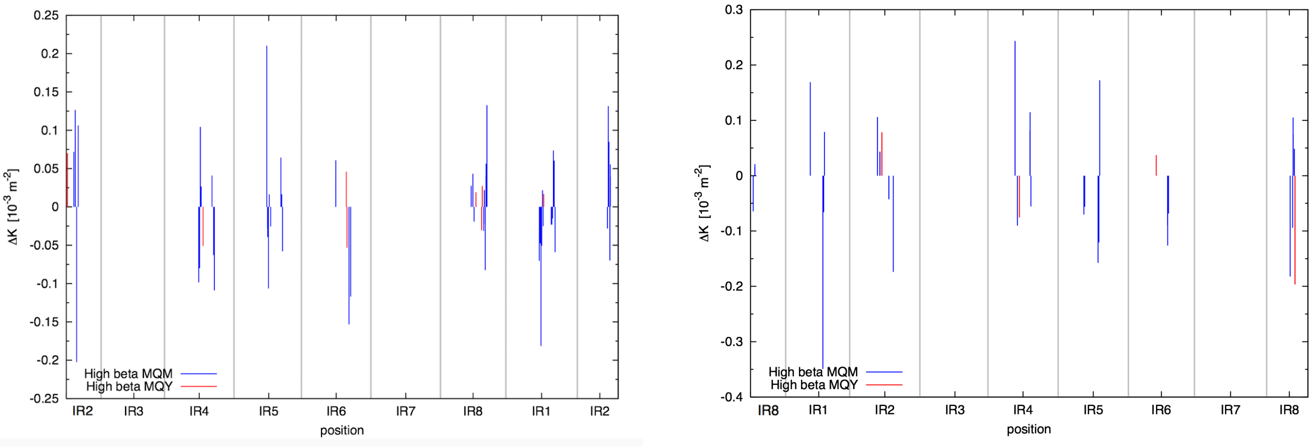

Figure 5.10: Global corrections applied in the MQM and MQY magnets (Beam 1 left and beam 2 right).

Effectiveness and revalidation of optics corrections

A comparison between β-beating before and after global corrections is shown in Figs. 5.11a and 5.11b. The effectiveness of the global corrections is assessed in Tabs. 5.6 and 5.7 by comparing the rms β-beating and maximum value before and after corrections. A general decrease in the β-beating RMS can be observed for both planes and both beams. The local change in the IR1 optics has not significantly increased the overall β-beating. Additionally, a comparison between the measurements corresponding to the different optics configurations is shown in Figs. 5.12a and 5.12b.

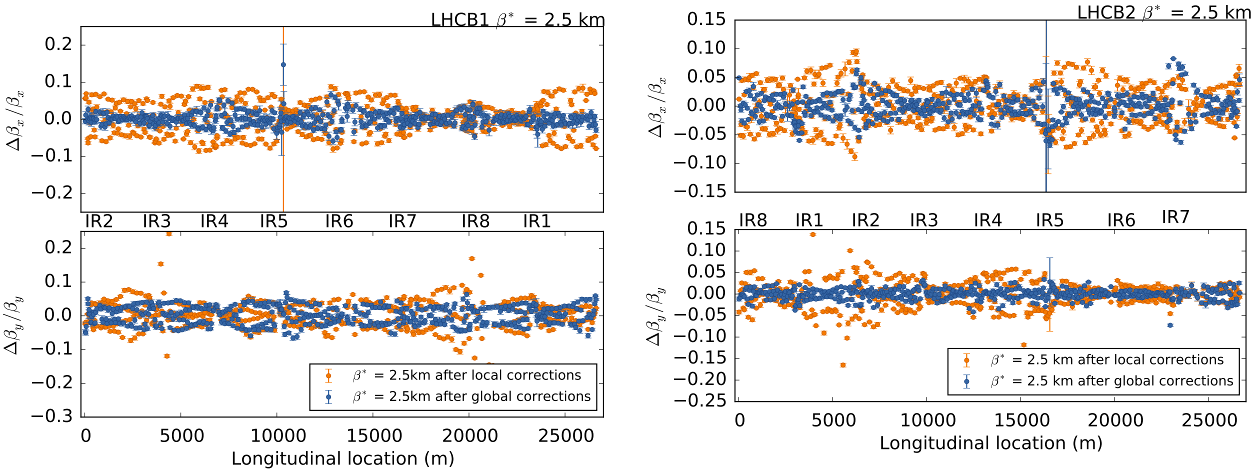

(a) β-Beating Beam 1.

(b) β-beating Beam 2.

Figure 5.11: β-beating before and after global corrections at $\beta^* = 2.5$ km.

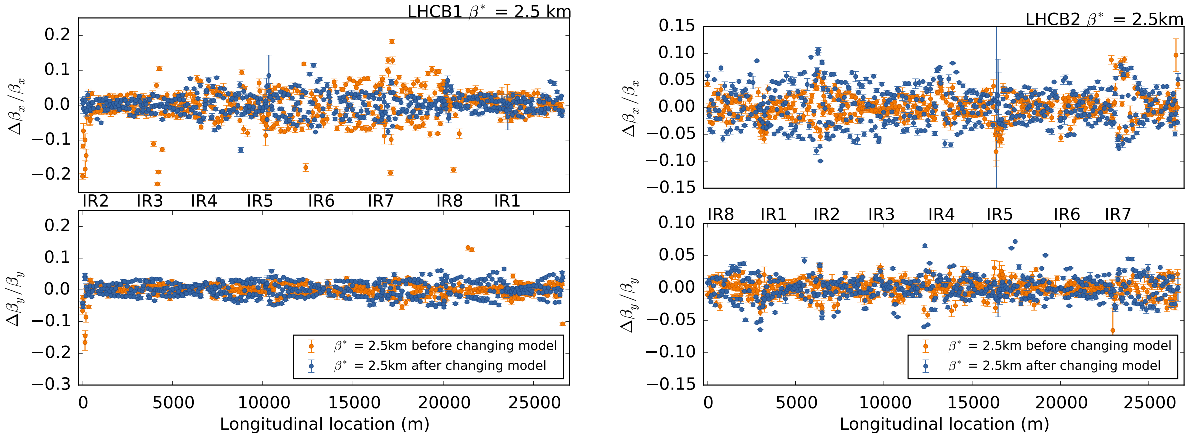

(a) β-beating Beam 1.

(b) β-beating Beam 2.

Figure 5.12: β-beating before and after changing the phase advance between the interaction point (IP) and the roman pots at $\beta^* = 2.5$ km.

5.2.9 Effectiveness and re-validation of calibration factors calculation

Figures 5.13a and 5.13b show the β-function measured after corrections using β^{ϕ}, β^{A} and $\beta^{\mathrm{A,calibrated}}$. A decrease of the β-beating measured in IR1 and IR5 can be seen in both figures when applying the calibration factors.

Table 5.26 summarizes the β-beating of the β^{A} with respect to the β^{ϕ} for both beams before and after re-calibrating the BPMs in IR1 and IR5. An average 4% improvement has been observed in the β^{A} measurements after re-calibrating the BPMs. Nonetheless, a remaining 3% average β-beating together with several BPM hardware and software upgrade, motivated the recalculation of the BPM optics-based calibration factors.

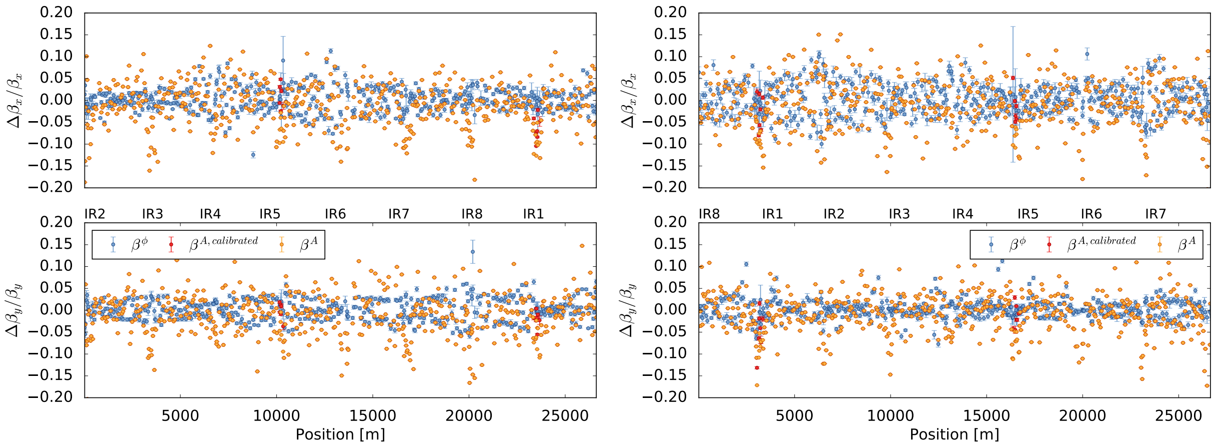

(a) β-beating Beam 1.

(b) β-beating Beam 2.

Figure 5.13: β-beating measured using three different techniques (β^ϕ,β^A,$\beta^{A,calibrated}$).

	Beam 1		**Beam 2**	
	Before re-ca	**After re-cal**	**Before re-cal**	**After re-cal**
$\frac{(\beta_x^{\mathrm{A}}-\beta_x^\phi)}{\beta_x^\phi}$ (%)	-8.5	-2.5	-7.4	-3.1
$\frac{(\beta_y^{\mathrm{A}}-\beta_y^\phi)}{\beta_y^\phi}$ (%)	-8.8	-4.2	-6.7	-3.3

Table 5.8: rms and maximum values for the horizontal β-beating for both beams before and after BPM re-calibration.

5.2.10 Off-momemtum measurements

Dispersion

Off-momentum measurements were performed at $\beta^* = 2.5$ km before and after global corrections. A comparison of the normalized dispersion beating before and after global corrections is shown in Figs. 5.14a and 5.14b. The peak and rms normalized dispersion beating are shown in Tabs. 5.9 and 5.10, where a small reduction of the dispersion beating after the optics corrections is visible.

		Beam 1		
		Before global corr.	**After global corr.**	
		June	June	August
$\frac{\Delta D_x}{\sqrt{\beta_x}}$ $[10^{-3}\mathrm{m}^{1/2}]$	max	19.5 ± 0.8	14 ± 3	20 ± 3
	rms	7.3	4.6	6.1

Table 5.9: rms and maximum values of normalized horizontal dispersion beating before and after global corrections (Beam 1).

		Beam 2		
		Before global corr.	**After global corr.**	
		June	June	August
$\frac{\Delta D_x}{\sqrt{\beta_x}}$ [$10^{-3}\mathrm{m}^{1/2}$]	max	23.7 ± 0.7	15 ± 2	15 ± 2
	rms	7.3	4.5	4.4

Table 5.10: rms and maximum values of normalized horizontal dispersion beating before and after global corrections (Beam2).

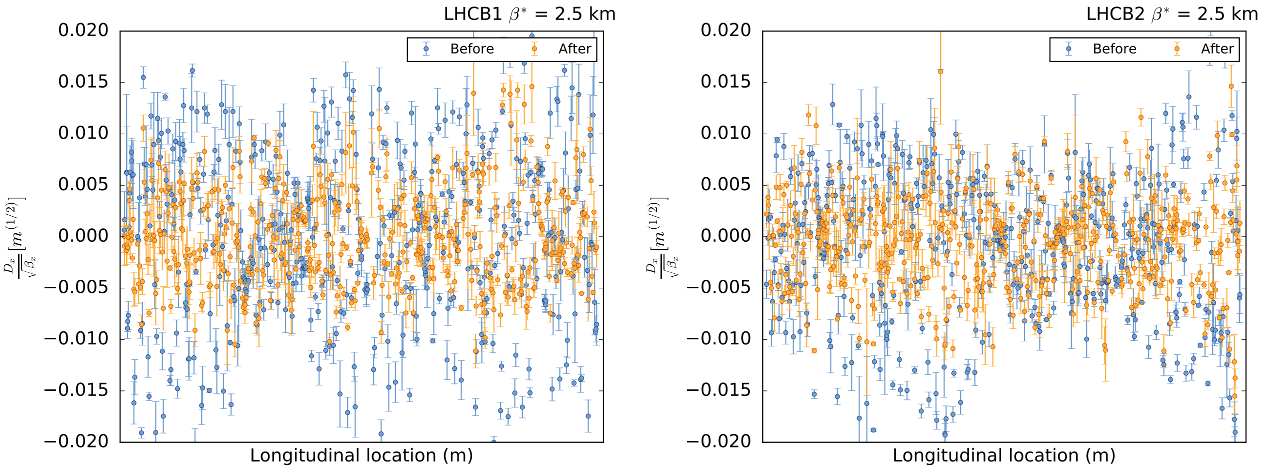

(a) Beam 1.

(b) Beam 2.

Figure 5.14: Normalised dispersion measured in June before and after corrections at $\beta^* = 2.5$ km.

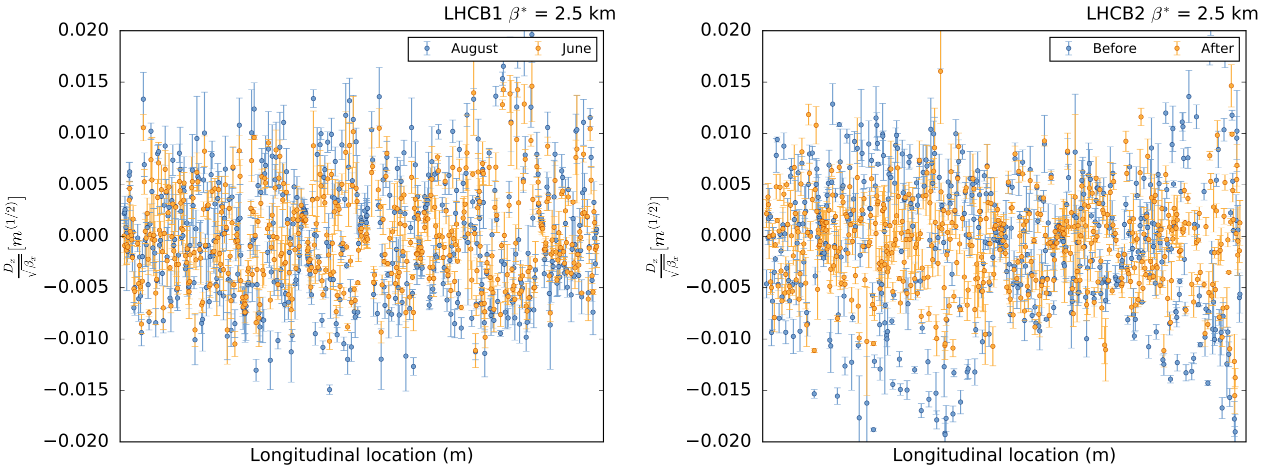

(a) Beam 1.

(b) Beam 2.

Figure 5.15: Normalised dispersion measured in June vs August $\beta^* = 2.5$ km.

5.2.11 Phase advance calculations between different elements of the lattice.

For computing the phase advance between elements in the machine, it is necessary to combine measurements and simulations. This is because phase advance can only be measured between two BPMs, but it can be extrapolated to the closest elements by model propagation through the lattice. Figures 5.16 and 5.17 show a schematic of how this technique works. At first, a segment is defined by two BPMs, one placed on the left of the element and the other located on the right (Fig. 5.16). Secondly, β_i, α_i and γ_i measured at the beginning and at the end of the segment are used as boundary conditions for the MAD-X simulations (Fig. 5.17). The error bar is calculated by error propagation, considering the initial uncertainties, $\Delta\beta_i$, $\Delta\alpha_i$ and $\Delta\gamma_i$ as explained in [2]. The difference between the phase advance measured in August with respect to the values obtained in June is in all the cases smaller than 0.5 °. Table 5.12 summarizes the differences between values measured in June and August, phase advance predicted by model and relative difference in phase and in $\sin(\mu_{IP\rightarrow RP})$.

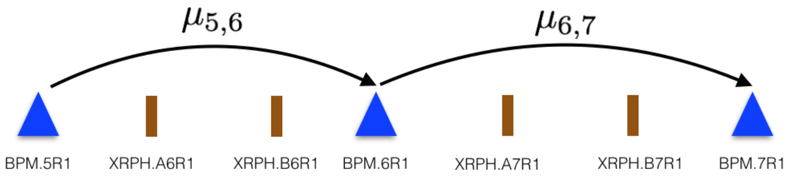

Figure 5.16: Phase advance measured between two arbitrary BPMs.

Figure 5.17: Model propagation.

	August		June	
Roman pot	$\mu_{IP\rightarrow RP}$ (°)	$\mu_{IP\rightarrow RP\mathrm{model}}$ (°)	$\mu_{IP\rightarrow RP}$ (°)	$\mu_{IP\rightarrow RP\mathrm{model}}$ (°)
XRPH.A6R1.B1	176.4 ± 0.2	176.4	176.9 ± 0.3	176.9
XRPH.B6R1.B1	177.3 ± 0.2	177.3	177.7 ± 0.2	177.6
XRPV.A7R1.B1	180.6 ± 0.4	180.6	180.1 ± 0.4	180.1
XRPV.B7R1.B1	182.6 ± 0.4	182.5	181.6 ± 0.4	181.5

Table 5.11: Horizontal phase advance between IP1 and different roman pots.

Roman pot	$\Delta\mu_{IP\rightarrow RP}$ (° measurement)	$\Delta\mu_{IP\rightarrow RP}$ (° model)	$\Delta\sin(\mu_{IP\rightarrow RP})$ (%)
XRPH.A6R1.B1	-0.5 ± 0.3	-0.5	18.5
XRPH.B6R1.B1	-0.3 ± 0.3	-0.2	19
XRPH.B6R1.B1	0.5 ± 0.6	0.6	622
XRPV.B7R1.B1	1 ± 0.6	1	62

Table 5.12: Relative phase advance difference between June and August.

5.2.12 Summary of high-β^* at flattop energy

Results of optics measurements for $\beta^* = 2.5$ km after local and global corrections have been shown. Three sets of measurements were performed at different β^* in order to control the β-beating during the de-squeezing process. The rms β-beating was well controlled below- 6% and no optics corrections were needed during the first part of the de-squeeze (up to 500 m). An intermediate step was done ($\beta^* = 1.7$ km) in order to apply coupling and local corrections. Coupling was successfully corrected, especially in Beam 2 (Fig. 5.7a). A decrease in rms β-beating after applying local corrections, is shown in Tab. 5.5. Global corrections were successfully implemented at β^* 2.5 km reducing rms β-beating to approximately 3% in the horizontal plane and 2% in the vertical plane. Section 5.2.9 shows a decrease in the β-beating of β^{A} with respect to the β^{ϕ} when the calibration factors are applied. Additionally, off-momentum measurements show a slightly improved normalized dispersion beating after corrections. Some slight modifications were performed in IP1 after having analyzed the results of the first session in order to match the requirements set by the experiment ALFA. A deviation with respect the 180° phase advance has been seen in Tab. 5.11. This deviation has allowed ALFA experiment to perform more accurate measurements.

5.3 High-β^* optics at injection

In the TOTEM Technical Proposal [63] it is mentioned the interest of running at 900 GeV per beam (Tevatron energy), because the optics with high-$\beta^* = 1100$ m would make possible the measurement of Coulomb interference (momentum transfer $|t_{\mathrm{min}}| = 0.0005$ GeV^2 feasible at that energy).

High-β^* at injection has been requested by TOTEM after the promising results obtained during 2016 in the very high-β^* (> 1000 m) run at flattop energy, 6.5 TeV, introduced earlier in this chapter [107] . Measurements at high-β^* at injection energy, 450 GeV, aim to complete the study of the differential proton-proton scattering cross-section. The value of the β function at the interaction point defines the goal of the experiments. In order to asses the technical feasibility a preliminary run at$\sqrt{s} = 900$ GeV with a β^* in the range of 50-100 meters has been studied. The optics commissioned was a flat optics with different β^* values in the interaction points 1 and 5. The β^* values in the IP1 (ATLAS/ALFA) are $\beta^*_x = 52.9$ m and $\beta^*_y = 98.1$ m whereas in IP5 (CMS/TOTEM) β^* values are $\beta^*_x = 75.9$ m and $\beta^*_y = 96.5$ m.
Two different approaches have been used for measuring the β^* at the interaction point: β from phase [2, 4] and K-modulation [56]. High-β^* at injection has been commissioned for the first time on 26 October 2017 and validated lately on 8 November 2017. Section 5.3.1 summarizes the measurements and corrections - local, global and coupling- performed during both sets of

	Beam 1		**Beam 2**	
	Horizontal	Vertical	Horizontal	Vertical
rms $\frac{\Delta\beta}{\beta}$(%)	15.7	10.8	30.6	19.5

Table 5.13: RMS β-beating before corrections at high-β^*.

		Before coupling corr.		After coupling corr.	
		Beam 1	Beam 2	Beam 1	Beam 2
$\lvert c^- \rvert (10^{-3})$	Before local corrections	2.9	1.9	0.9	0.6
	After local corrections	5.8	1.7	1	1.5

Table 5.14: $|c^-|$ measurements before and after local corrections at high β at injection.

measurements. Section 5.3.3 summarizes the values of the β^* measured using k-mod, β from phase.

5.3.1 Optics measurements and corrections

The first optics measurements were performed the 26/10/2017 to assess the quality of the optics and to perform corrections if necessary.

Table 5.13 summarizes the values of the rms β-beating without having applied any corrections in the machine.

The first measurements reveal an rms β-beating of about 30% in the horizontal plane in Beam 2. Due to these large values observed, local and global corrections were implemented in the machine. Some minor corrections were applied in order to reduce coupling.

5.3.2 Coupling corrections

Quick initial measurements were performed in order to check the coupling in the machine. The real and imaginary parts of C^- were automatically calculated in the multiturn application during the measurements [96, 123]. The knobs are implemented in the machine changing the value of the skew quadrupole currents. Coupling was lately corrected again after implementing local optics corrections in the machine. The modules of the $|C^-|$ correction applied during the first commissioning of high-β^* at injection are summarized in Tab. 5.14. Coupling was successfully corrected after the first coupling corrections implemented at the beginning of the MD. Additional coupling corrections were performed after local corrections just before k-modulation measurements. Since no turn-by-turn measurements were performed after applying coupling corrections in the machine, the value of the $|C^-|$ was not calculated.

MAD-X variable	Design magnet k [10^{-3} m^{-2}]	Δk [10^{-5} m^{-2}]	Correction (%)
kq5.l1b1	-5.9	-7.5	1.3
kq4.l1b1	3.5	7.5	2.1
kq7.l1b2	3.4	-1.2	-0.4
kq5.l1b2	6.2	2	0.3
kq5.r5b2	-6.0	-3	0.5
kq5.l5b2	6.3	3	0.5
kq6.r5b2	6.0	1.5	0.3
kq6.l5b1	6.0	3.2	0.5
kq5.l5b1	-5.9	-1.5	0.3
kq4.l5b1	3.0	-10	-3.3

Table 5.15: Local corrections applied at high β^* at injection in 2017 as applied in LHC Software Architecture LSA.

Magnet	Circuit	Design magnet k [10^{-3} m^{-2}]	Δk [10^{-5} m^{-2}]	Correction (%)
MQXB.B2L5	- kqx.l5 - ktqx2.l5	6.1	3	0.5
MQXB.A2L5	- kqx.l5 - ktqx2.l5	6.1	3	0.5
MQXB.B2L1	- kqx.l1 - ktqx2.l1	6.2	3.5	0.6
MQXB.A2L1	- kqx.l1 - ktqx2.l1	6.2	3.5	0.6
MQXB.A2R1	- kqx.r1 - ktqx2.r1	-6.3	-5	0.8
MQXB.B2R1	- kqx.r1 - ktqx2.r1	-6.3	-5	0.8

Table 5.16: Local corrections applied at high β^* at injection in 2017 for the Q2 quadrupole as applied in LHC Software Architecture LSA.

5.3.3 First measurements and corrections performed on the virgin machine

The analysis of the first on-momentum measurements shows a large β-beating, as it can be seen in Tab. 5.17. In order to improve the performance of the optics, two sets of corrections were applied into the machine. The first set that attempts to reduce strong localized β-beating sources in the IRs, consisted on local corrections applied in the interaction regions (IRs) 1 and 5 by changing the strength of the several common quadrupoles. Tables 5.15 and 5.16 summarize the relative, absolute and nominal values of the strength change. Due to the electrical configuration of the LHC magnets, a change on the strength of the power supply can affect one or several magnets. On the other hand, a magnet can be powered by one or more power supplies. In the IR, the quadrupole placed in the middle of the triplet, the Q2, is powered by two power supplies: the main one kqx and ktqx that is used for small strength changes. Table 5.15 summarizes the corrections of the magnets powered by one power supply while Tab. 5.16 reflects the change in the Q2 magnet strength after changing the ktqx strength.

The weakest quadrupoles placed in IR1 are the kq4.l1b1 and kq7.l1b1 while for IR5 the quadrupole with less current is the kq4.l5b1. The largest optics corrections was needed for kq5.l1b1 and kq4.l1b1 in IP1 and kq4.l5b1 in IP5. In order to ensure proper operation of

	Beam 1				Beam 2			
	Before local corr.		**After local corr.**		**Before local corr.**		**After local corr.**	
	Horizontal	Vertical	Horizontal	Vertical	Horizontal	Vertical	Horizontal	Vertical
rms $\frac{\Delta\beta}{\beta}$(%)	15.7	10.8	14.7	8.1	30.6	19.5	23.7	13.8

Table 5.17: rms β-beating before and after local corrections at high-β^*.

the quadrupoles, the value of the strength in operation should not be lower than 2% of the maximum value. In this optics, the final value of the magnet strength, k, after applying optics corrections has been kept above this limit.

For the Q2 quadrupoles, the values of the strength correspond to approximately 70% of the injection optics strength.

The Q1 strength has been set to 75% of the current of the quadrupoles in the injection optics configuration.

The effectiveness of the corrections is evaluated by measuring the rms β-beating in the machine before and after corrections. Figures 5.18a and 5.18b show the β-beating around the LHC before and after local corrections. These values are summarize in Tab. 5.17. Even though a decrease in the rms β-beating can be seen in both planes, the values obtained are too large for safe operation [105, 51].

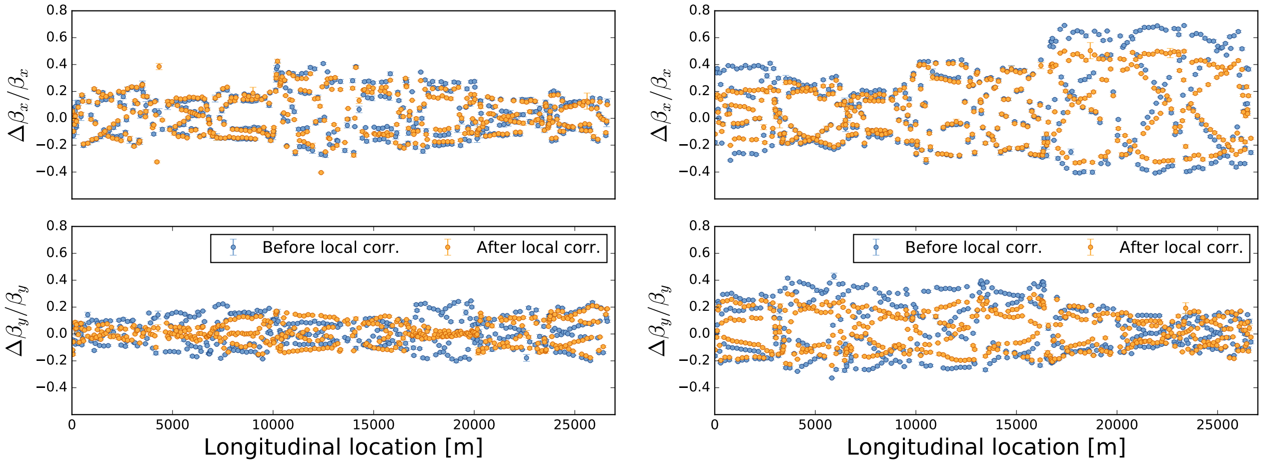

(a) Beam 1.

(b) Beam 2.

Figure 5.18: β-beating before and after local corrections.

β^* calculations

The value of the β at the interaction point can be calculated either by using the segment-by-segment technique [2] or using k-modulation [124, 45]. Table 5.18 summarizes β^* values measured using segment-by-segment technique as well as the values expected by the model in IP1 and IP5 for Beam 1 and Beam 2.

β^* measurements obtained using k-modulation are summarized in Tab. 5.19.

		IP 1				**IP 5**			
		Measured		**Model**		**Measured**		**Model**	
		Hor.	Ver.	Hor.	Ver.	Hor.	Ver.	Hor.	Ver.
β^* [m]	Beam 1	53.6 ± 0.5	88 ± 2	52.9	98.1	108 ± 2	107 ± 3	75.9	96.5
	Beam 2	61.9 ± 0.5	95 ± 1	52.7	101.4	45 ± 1	77 ± 2	63.2	95.4

Table 5.18: β^* value measured using β from phase and expected value predicted by MADX in IP1 and IP5 for both planes after applying local corrections.

		IP 1		**IP 5**	
		Measured		**Measured**	
		Horizontal	Vertical	Horizontal	Vertical
β^* [m]	Beam 1	55 ± 5	88.8 ± 0.2	100 ± 8	104 ± 1
	Beam 2	66 ± 7	95.8 ± 0.3	47.3 ± 0.3	80.1 ± 0.6

Table 5.19: β^* value measured in IP1 and IP5 for both beams using k-modulation after applying local corrections.

β from phase and k-modulation results agree within given error bars. The large β-beating of about 20% is because these measurements were performed before global corrections.

Some of the k-modulation measurements have poorer resolution and accuracy than β^* results obtained using the segment-by-segment technique.

The poor resolution and accuracy obtained in k-modulation results can be due to large tune fluctuations. Tune jitter for a given optics can be simulated using MADX in order to have a first order estimation of its value. An error of one part per million with respect to the circuit current is introduced in the different circuits in order to see the impact on the tune. Figure 5.19 summarizes the effect of each different circuit in the horizontal and vertical tune jitter, $|\Delta Q|$.

Fluctuations of the tune jitter during the measurements performed in October have been measured by analyzing the data acquired using the diode-based base-band-tune (BBQ) technique (Tab. 5.20) and the data obtained with the Turn-by-Turn measurements (Tab. 5.21). Turn-by-turn measurements are performed using the AC-dipole as external excitation [122]. The AC-dipole data values are the mean values of the individual tune distributions from each measurement file. For the BBQ-data, an average smoothing was used to reduce the noise and the AC-dipole excitations were cleaned.

Figures 5.20-5.23 show the tune evolution during the measurements performed in October. These plots combine the measurements obtained using BBQ and turn-by-turn techniques.

A significant slow drift of the tunes is observed for both beams and planes, implying probably a decay of mean quadrupolar field.

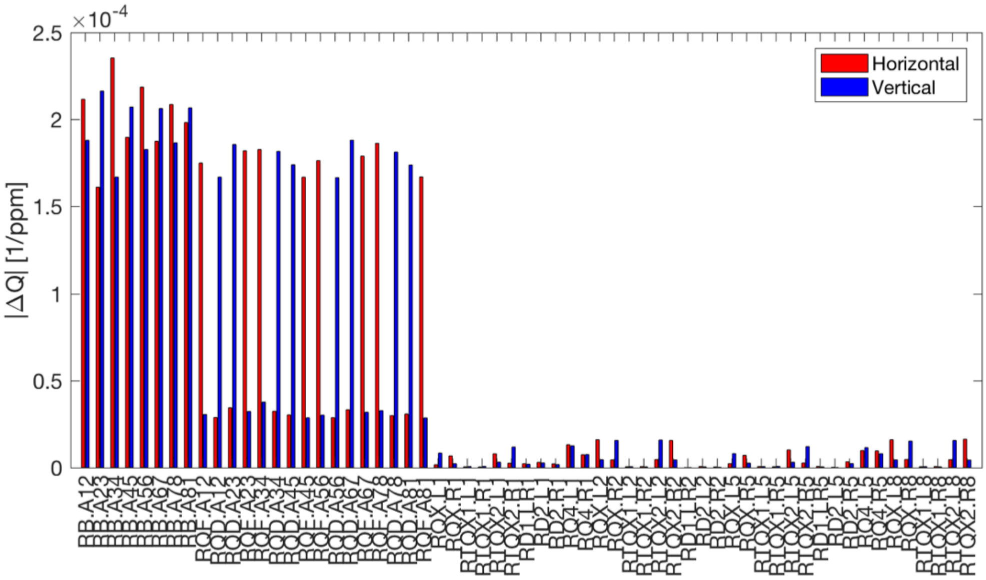

Figure 5.19: Simulations of tune variation per ppm of quadrupole circuits.

	BBQ					
	Horizontal			**Vertical**		
	Tune jitter in $[10^{-4}]$	σ tune jitter in $[10^{-4}]$	Simulated tune jitter in $[10^{-4}]$	Tune jitter in $[10^{-4}]$	σ tune jitter in $[10^{-4}]$	Simulated tune jitter in $[10^{-4}]$
Beam 1	2.3	-1.0 | +1.1	1.5	2.4	-1.1 | +1.1	1.5
Beam 2	3.1	-1.1 | +1.1	1.5	2.4	-0.9 | +1	1.5

Table 5.20: Tune jitter simulated and measured by analyzing the data recorded using BBQ technique.

5.3.4 Global corrections

After the implementation of local corrections, global corrections were computed in order to reduce the large β-beating observed after local corrections. The modification of the strength of the quadrupoles Δk is shown in Figures 5.24a and 5.24b. Plots are divided by type of magnet MQM (dispersion suppressor areas), MQY (matching sections) and MQT (trim quadrupoles).

Figures 5.25a and 5.25b compare the β-beating before and after global corrections.

Table 5.22 quantifies the performance of global corrections showing the rms β-beating after the local corrections and after global corrections. From this table, it can be concluded that global corrections were highly effective for both planes and both beams.

Table 5.23 summarizes the β^* measurements performed after global corrections using β from phase approach and model values for both beams and IPs. The larger β^* measurements can be seen in IP5 for both beams, with an average β^*-beating of 6%.

	Turn-by-turn			
	Horizontal		**Vertical**	
	Tune jitter in $[10^{-6}]$	σ tune jitter in $[10^{-6}]$	Tune jitter in $[10^{-6}]$	σ tune jitter 10^{-6}
Beam 1	2.8	-1.2 | +0.7	3.4	-1.5 | +0.20
Beam 2	2.8	-1.2 | +0.5	3.2	-0.9 | +1.0

Table 5.21: Tune jitter measured by analyzing the data recorded using TbT method.

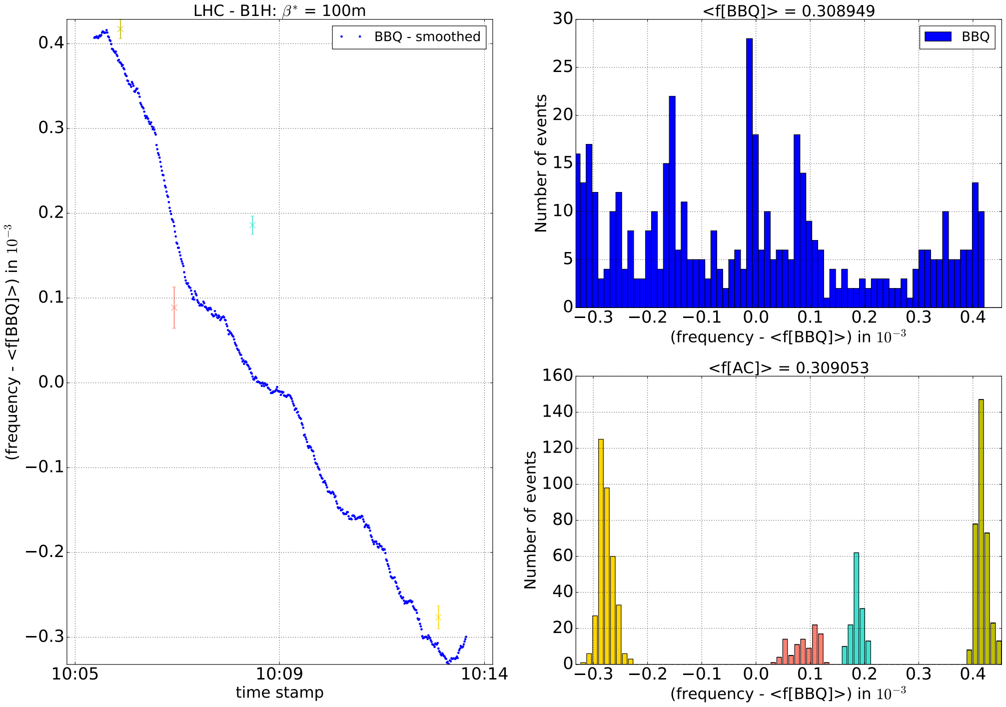

Figure 5.20: Horizontal tune jitter measured using BBQ (blue) and turn-by-turn (dots) as a function of time (Beam 1).

		Beam 1			
		After local corr.		**After global corr.**	
		Hor.	Ver.	Hor.	Ver.
rms $\frac{\Delta\beta}{\beta}(\%)$	Beam 1	14.7	8.1	4.9	2.7
	Beam 2	23.7	13.8	3.3	3.8

Table 5.22: rms β-beating after local corrections and after global corrections at high-β^*.

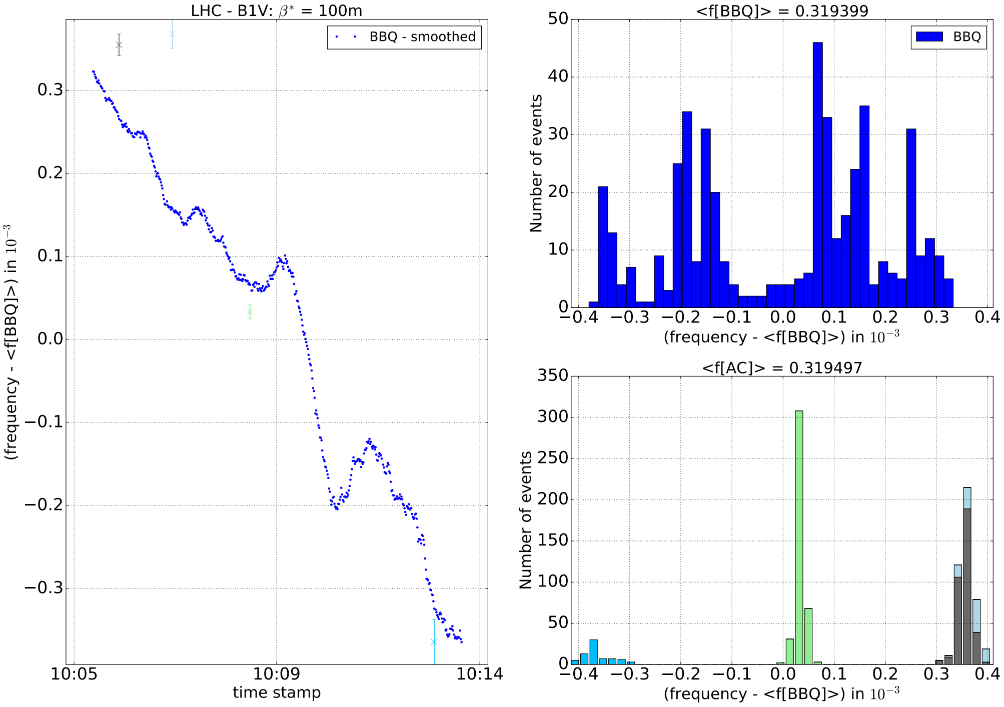

Figure 5.21: Vertical tune jitter measured using BBQ (blue) and turn-by-turn (dots) as a function of time (Beam 1).

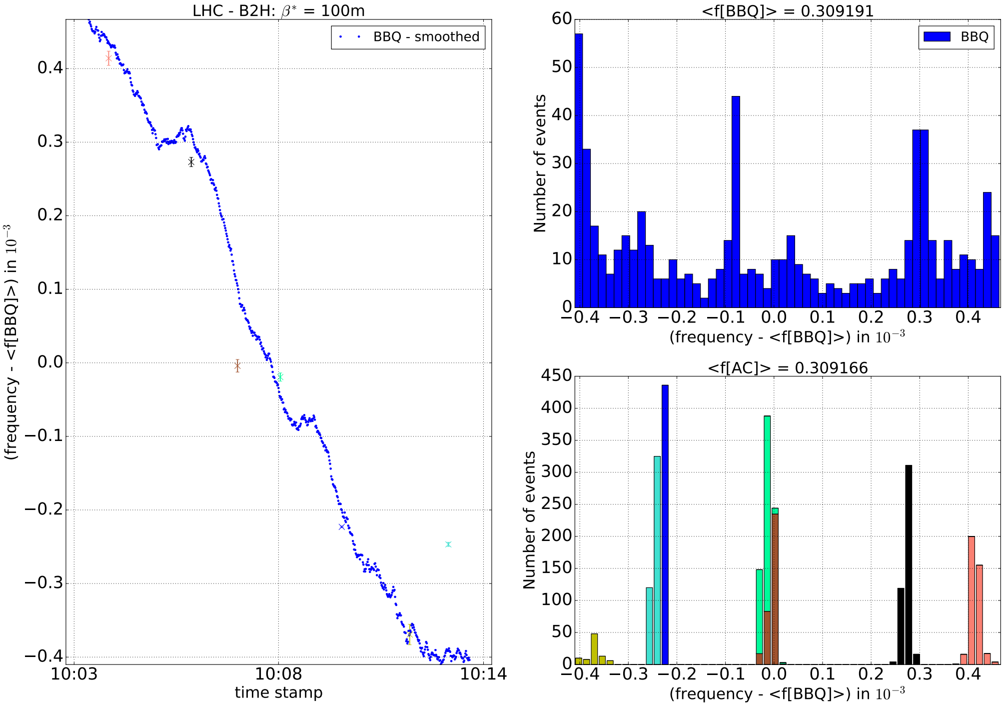

Figure 5.22: Horizontal tune jitter measured using BBQ (blue) and turn-by-turn (dots) as a function of time (Beam 2).

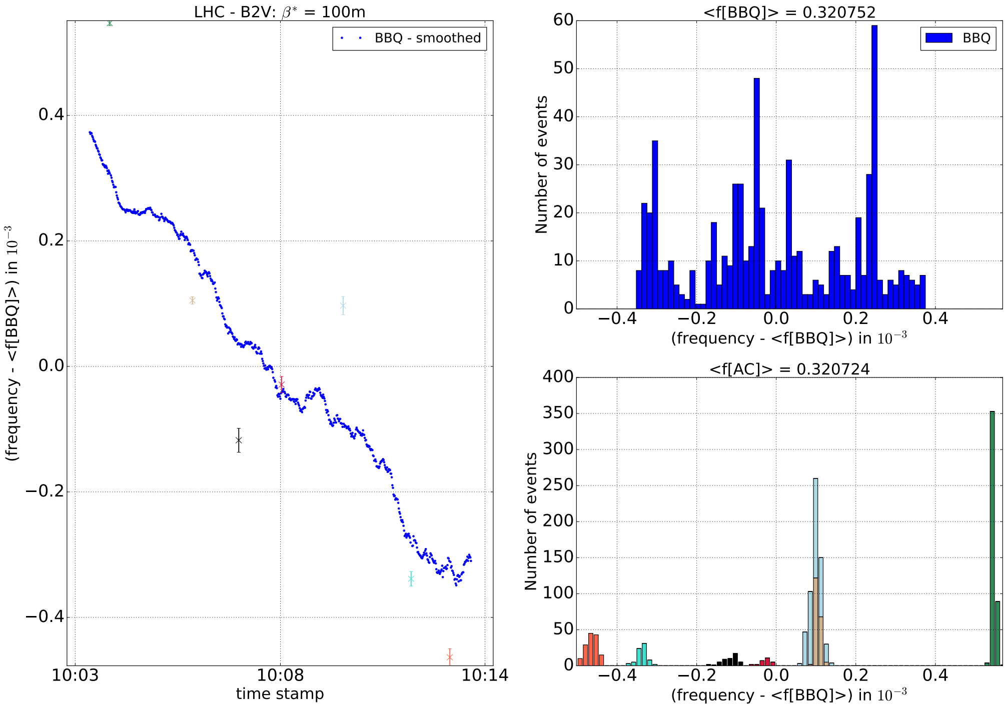

Figure 5.23: Vertical tune jitter measured using BBQ (blue) and turn-by-turn (dots) as a function of time (Beam 2).

		IP 1				**IP 5**			
		Measured		**Model**		**Measured**		**Model**	
		Hor.	Ver.	Hor.	Ver.	Hor.	Ver.	Hor.	Ver.
β^* [m]	Beam 1	53.8 ± 0.6	95 ± 1	52.9	98.1	79 ± 1	88 ± 1	75.9	96.5
	Beam 2	52.1 ± 0.8	101 ± 1	52.7	101.4	65 ± 2	90 ± 2	63.2	95.4

Table 5.23: β^* value measured using β from phase and expected value predicted by MADX in IP1 and IP5 for both planes after applying local corrections.

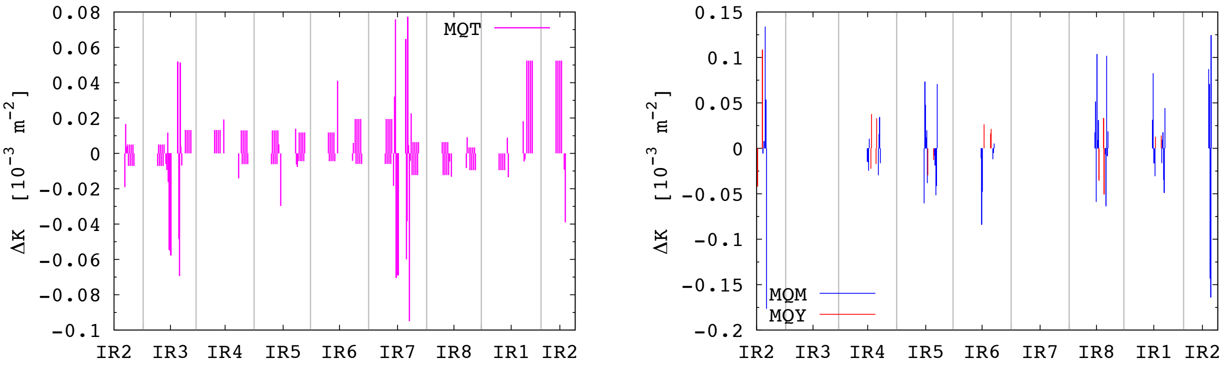

(a) MQT quadrupoles power supplies.

(b) MQM and MQY quadrupoles power supplies.

Figure 5.24: Change in the quadrupolar strength, Δk, applied in order to perform global corrections for Beam 1.

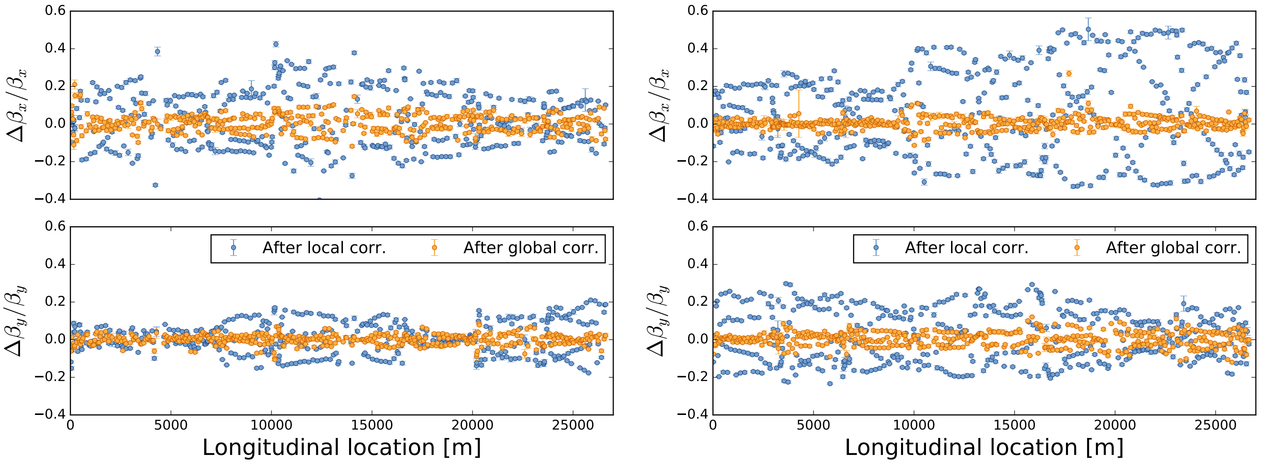

(a) β-beating Beam 1.

(b) β-beating Beam 2.

Figure 5.25: β-beating after local corrections and after local and global corrections.

5.3.5 Second set of measurements

A second set of measurements was performed the 08/11/17 in order to validate the results obtained during the first set of measurements. A tune shift of 0.03 was observed at the beginning of the second set of measurements. One possible explanation is the effect of the quadrupole hysteresis especially when running with small strength values. In order to match the tune to the design one the MQTs are used. The change in the tune observed in the BBQ was corrected by trimming the MQTs to larger values than in the first set of measurements. Figure 5.26 shows a comparison of the MQTs strength between October and November.

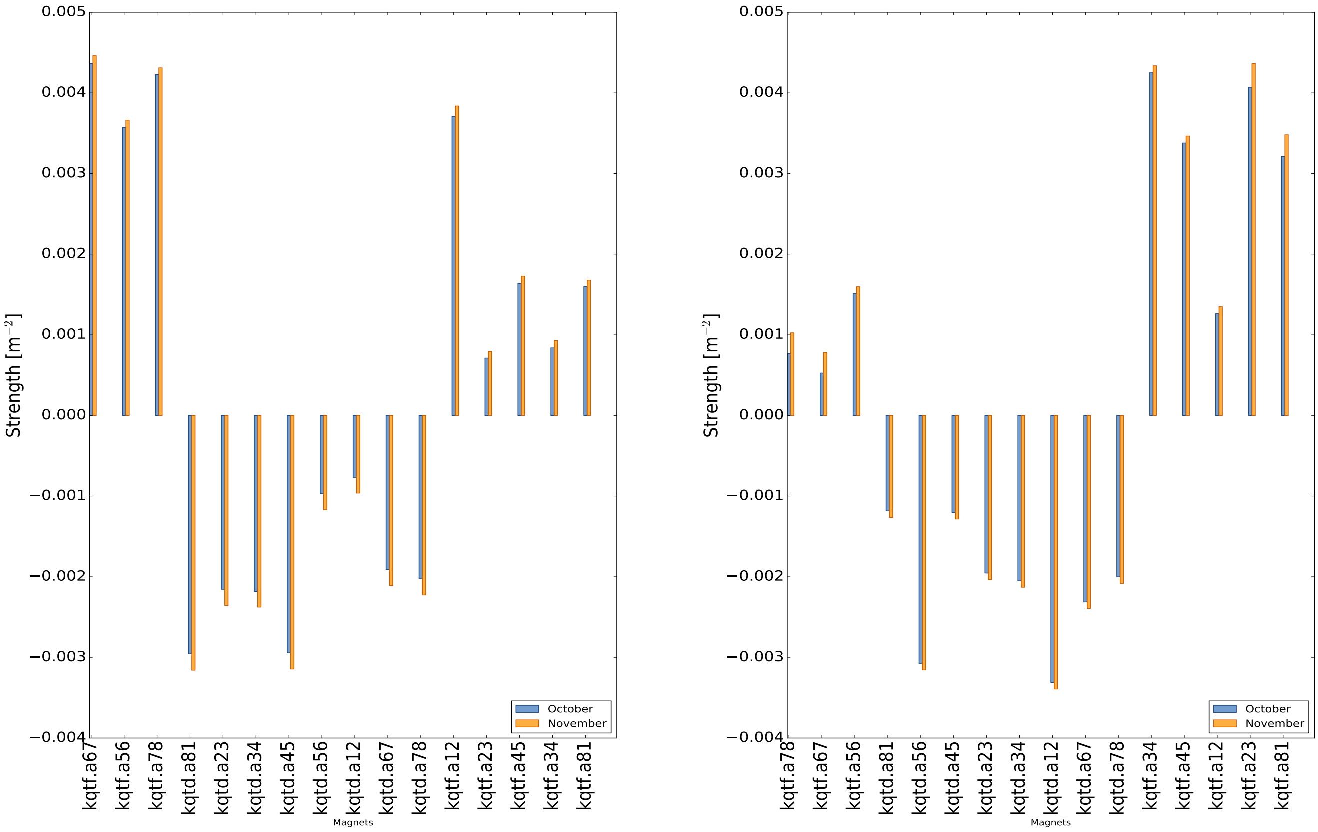

Figure 5.26: Comparison of the strength of the MQTs set into the machine in October and in November after the tune correction.(left Beam 1 and right Beam 2).

The reproducibility of the β-beating computed in October was evaluated during this second iteration of high β^* at injection. Figures 5.27a and 5.27b shows β-beating measured around the LHC in October and November with local and global corrections.

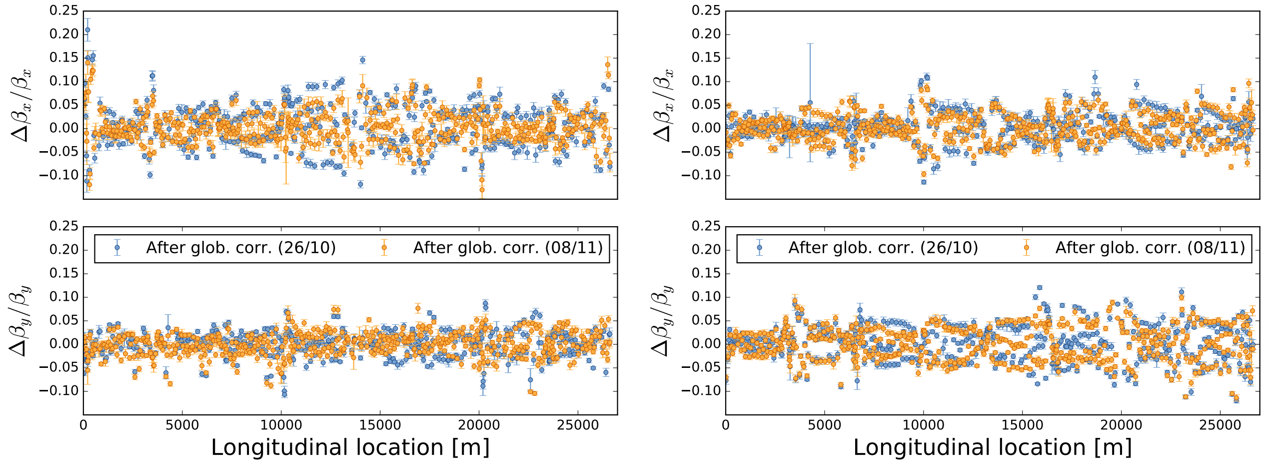

(a) β-beating Beam 1.

(b) β-beating Beam 2.

Figure 5.27: β-beating measured in October and November.

Table 5.24 shows a comparison of the rms β-beating measured in October and in November.

	Beam 1				**Beam 2**			
	October		**November**		**October**		**November**	
	Hor.	Ver.	Hor.	Ver.	Hor.	Ver.	Hor.	Ver.
rms $\frac{\Delta\beta}{\beta}$(%)	4.9	2.7	3.5	2.6	3.3	3.9	3.0	3.6

Table 5.24: rms β-beating measured in October vs November.

		IP 1				**IP 5**			
		Measured		**Model**		**Measured**		**Model**	
		Hor.	Ver.	Hor.	Ver.	Hor.	Ver.	Hor.	Ver.
β^* [m]	Beam 1	53 ± 1	99 ± 1	52.9	98.1	77 ± 1	94.5 ± 0.7	75.9	96.5
	Beam 2	53.3 ± 0.6	100 ± 2	52.7	101.4	66 ± 1	94 ± 1	63.2	95.4

Table 5.25: β^* value measured using β from phase and expected value predicted by MADX in IP1 and IP5 for both planes measured in November.

The largest discrepancy between this two measurements have been observed in Beam 1 in horizontal plane. For the rest of the planes and beams the differences between October and November is less than 1%. Therefore, the overall reproducibilty of the β-beating is kept bellow 2%.

Table 5.25 summarizes the β^* values measured in November using β phase approach at IP1 and IP5. Comparing the measured β to the values predicted by the model, it is possible to see a decrease of the β-beating for both beams and planes in IP5. On the other hand, the largest discrepancies between the two different set of measurements in β^* have been observed in IP5. These changes can be explained due to the change in the MQT strength at the beginning of the MD. From Fig. 5.26 it can be seen that the strength of two defocusing and one focusing MQTs have been changed in IP5 while only the current of one MQT was modified in IP1.

5.3.6 Effectiveness and re-validation of calibration factors calculation

Figures 5.28a and 5.28b show the β-function measured after corrections using β^{ϕ}, β^{A} and $\beta^{\mathrm{A,calibrated}}$. A decrease of the measured β-beating of the β^{A} with respect to β^{ϕ} , defined as $\frac{(\beta_x^A-\beta_x^{\phi})}{\beta_x^{\phi}}$, can be seen in both Figs. 5.28a and 5.28b when applying the calibration factors in IR1 and IR5.

Table 5.26 summarizes the β-beating of the β^{A} with respect to the β^{ϕ} for both beams before and after re-calibrating the BPMs in IR1 and IR5. An improvement of the BPM re-calibration has been observed in 2017 with respect to 2016 since the maximum remaining β-beating, has been decreased to values lower than 2% after applying the calibration factors.

	Beam 1		**Beam 2**	
	Before re-cal.	**After re-cal.**	**Before re-cal.**	**After re-cal.**
$\frac{(\beta_x^A-\beta_x^\phi)}{\beta_x^\phi}$ (%)	-6.1	-0.5	-6.8	-1.6
$\frac{(\beta_y^A-\beta_y^\phi)}{\beta_y^\phi}$ (%)	-6.1	0.3	-7.4	-2.0

Table 5.26: rms and maximum values for the horizontal β-beating of the β^{A} with respect to the β^ϕ for both beams before and after recalibrating the BPMs in IR1 and IR5.

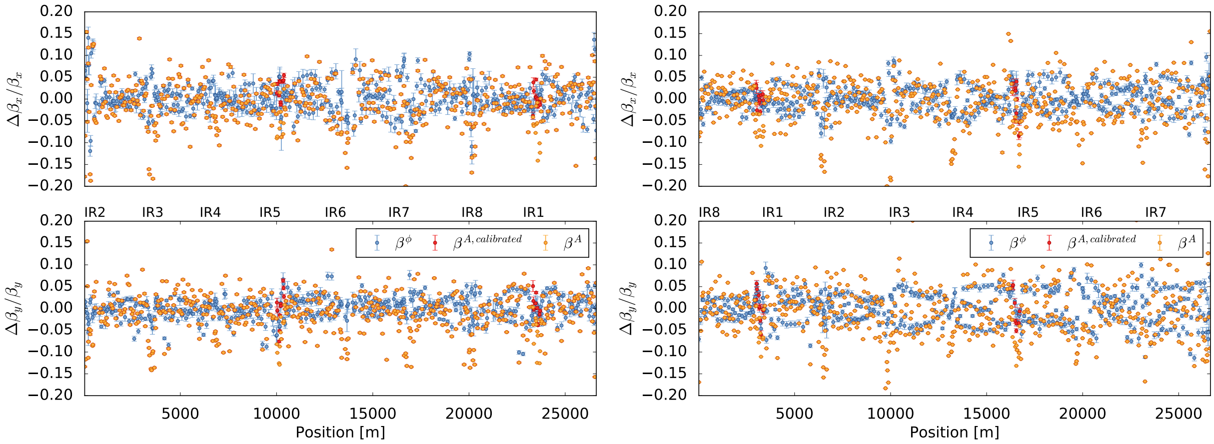

(a) β-beating Beam 1

(b) β-beating Beam 2

Figure 5.28: β-beating measured using three different techniques (β^ϕ,β^A,$\beta^{A,calibrated}$).

5.4 Summary

Even though virgin high-β^* optics presented high rms β-beating, the combination of local and global corrections managed to reduce it below 5% rms.

High-β^* optics was first commissioned in October 2017 and revalidated lately in November 2017. The comparison of both measurements, October and November, shows a discrepancy between the two sets of measurements of up to 1.5 % in the rms β-beating. Rms β-beating value was well controlled below 4% in November, which is the relevant one as it was performed with the operational cycle.

On the other hand, the most accurate results of β^* were obtained using β from phase method with a resolution of 2%. In terms of accuracy, larger β-beating has been observed in IP5 in both beams and planes.

The tune jitter level, shown in Fig. 5.19, is between 1.5 and 2 times large than the simulated value affecting the β^* function measurements using the k-modulation method, introducing large error-bars in the values of the β function measured in the BPMs closest to the IP. Therefore, these values have not been used for the global corrections. Finally, BPMs have been re-calibrated by implementing calibration factors computed using optics measurements approaches. A decrease of approximately 6% has been observed on β-beating of the β^{A} with respect β^ϕ both for Beam 1 and Beam 2 in horizontal and vertical plane.

Chapter 6

PSB Optics measurements and Corrections

As part of the LHC Injector Upgrade Project the injection energy of the CERN PS Booster will be changed to increase intensity and brightness of the delivered beams. The new injection scheme is likely to give rise to β beating above the required level of 5% and new measurements techniques are required. Achieving accurate optics measurements in PSB lattice is a challenging task that has involved several improvements in both hardware and software. This chapter summarizes all the improvements that have been performed in the optics measurement acquisition system together with a brief summary of the first results obtained.

Several major changes have been performed in PSB and in the rest of the injectors as part of the LHC Injector Upgrade project (LIU) [125]. LINAC4 will replace injection of protons by H^- ions. New injection system is based in charge-extraction principle, ions will be injected into a stripping foil used to strip electrons, located at the centre on the injection bump. The new system will present many advantages with respect to the old injection system such as decrease in the space-charge effects, improvement of the injection efficiency (from current 50% to 98%) but it will require a more accurate control of the optics functions. The new injection system will have an unknown effect in the β-function, with a possible strong error at the injection location. In order to have a full control on optics, the acquisition, control and analysis systems have been further developed including both software and hardware aspects.

The accuracy of the optics functions reconstruction in PSB is limited by its lattice configuration. The value of the phase advance between consecutive BPMs is approximately equal to $\mathrm{Q}_{x,y}/16$. The study of the dependency of the β^{ϕ} as a function of the phase advance value $\phi_{x,y,i,j}$ is presented in [2]. An alternative method to β^{ϕ} is the β^{A}, but it also presents a limitation since it is biased by the calibration factors as shown in Ch. 4. An optics-based-bpm-calibration method has been implemented at the PSB in order to measure the calibration factors and therefore be able to use the β^{A} approach. A dedicated optics with different working point with a more favorable phase advance between BPMs has been developed in order to get a β^{ϕ} that can be used for reference value for β^{A}. This new working point, denoted as Q3Q5 has been developed exclusively for optics-based-BPM calibration factor calculations. The maximum tune shift is limited by the strength of the magnets dedicated to the tune shift. The error-bar of the β^{ϕ} (σ_{β}) associated to the new working point and the nominal working point are signaled in Fig. 6.1.

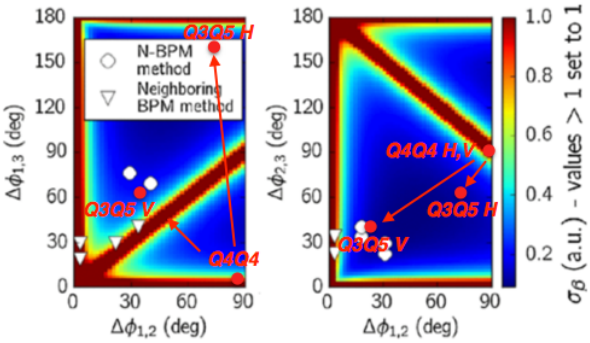

Figure 6.1: β^ϕ error bar as a function of the phase advance together with the phase advance values for the PSB taken from [2].

The implementation of optics measurement based on turn-by-turn data also required the upgrade of the existing hardware and software dedicated for the PSB turn-by-turn optics measurements. This chapter summarizes the studies performed as part of the commissioning of a new optics measurements since the beginning of 2016 to 2018, including:

1. Commissioning of the new pick-up system.
2. Commissioning of the upgrade of the experimental kickers: the transverse feedback system and the tune kicker.
3. Commissioning of a new working point denoted as Q3Q5, with different horizontal and vertical tunes that will be used for obtaining a reference value of th β^ϕ function for computing calibration factors.
4. Implementation of the otpics-based-BPM-calibration procedure introduced in Chapter 4 based on the ratio $\sqrt{\beta^{\mathrm{A}}/\beta^{\phi}}$.
5. Implementation of the optics-based-calibration factors measured using the Q3Q5 working point into the normal operational working point.

6.1 Experimental setup used during performance of optics measurements

Beam optics has been measured in PSB since 2013, using both turn-by-turn data and ORM [14, 126, 127, 128]. Optics functions measurements based on turn-by-turn data requires experimental kickers to excite the beam in phase-space to larger amplitudes. This excitation is performed by using experimental kickers, introduced in Ch. 1. In case of PSB, there are two different kicker magnets operating in different modes, installed at PSB that can be used for optics measurements. Nonetheless the hardware specifications were a limitation factor for the accuracy of the optics measurements based on turn-by-turn method and several equipment upgrades were required in order to improve the resolution of the optics measurements.

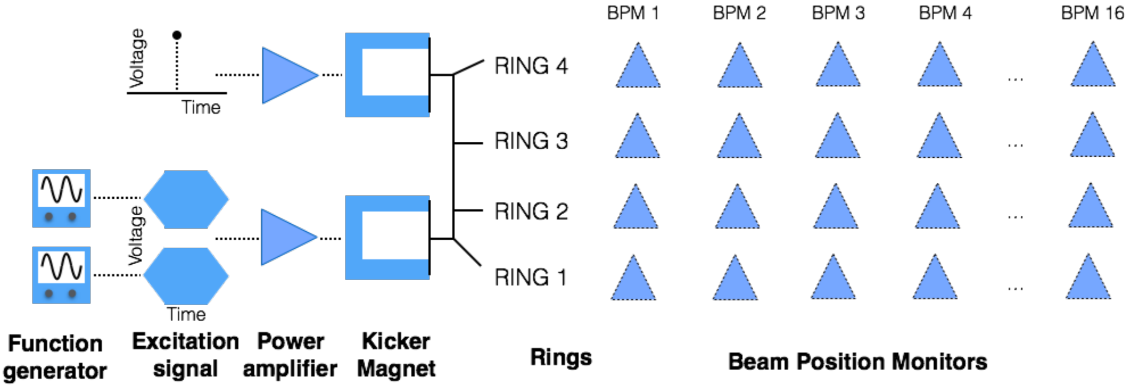

Figure 6.2: Hardware configuration used for optics measurements in 2018 (Horizontal and vertical plane) using the TFB system.

6.1.1 Hardware configuration

External excitation is performed as described in Ch. 1, both one time per cycle and periodically within the same cycle. In PSB, beam excitation can be performed using two external excitation sources, allowing to drive the beam in both horizontal and vertical plane to larger phase space amplitudes. Single kick measurements are performed by using the BBQ kicker while multiple kick excitation are performed using the transverse feedback (TFB or ADT) originally installed for beam stabilization but used as an AC-dipole during these studies [86].

The frequency of the TFB is usually expressed as a function of the beam tune denoted as driven tune, $Q_d = f_{\text{excitation}}/f_{\text{beam}}$. Both the amplitude of the driven oscillations and the number of turns recorded have an impact on the Fourier analysis resolution [129].

Single kick excitations in PSB is performed using the kicker BR.QMK12L1 that it is used in normal operation for tune, dispersion and chromaticity measurements. The tune kicker is operated by ramping up and down within one turn in order to apply a single transverse kick then allow free betatron oscillations.

Figure 6.2 shows an schematic of the complete instrumentation installation including the external kickers and an illustration of how they are triggered.

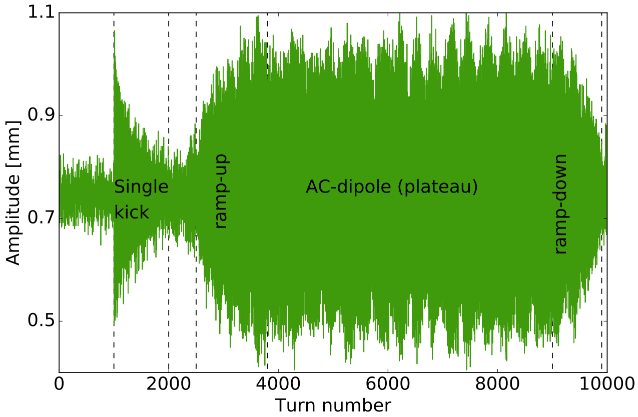

Figure 6.3: Optics measurements procedure in PSB.

Figure 6.3 shows the beam response to the two types of external excitation, the single kick and the transverse feedback. The single kick beam response shows a decoherence effect after the beam receives a single kick, which is caused by the different oscillating frequencies of the particles inside the beam. The effect leads to a measured center of charge in the vicinity of 0 after a number of turns. The number of turns than can be acquired before the beam completely decoheres can be modified – increase in one plane and decrease in the other plane – by changing the sextupolar current. Several measurements with different sextupolar current were performed in November 2017 in order to decrease the vertical chromaticity from -1.2 units to -0.1 increasing therefore, the number of turns available for the analysis. Nonetheless, the increase in the number of turns, only in the vertical plane, did not have a direct impact on the β-resolution. A large decoherence effect is observed just after the excitation and it cannot be avoided by changing the sextupolar current. Because of the reduced number of turns available for the analysis, this excitation method had not been used as widely as the TFB.

Decoherence effect can be avoided by exciting the beam in continuous mode (ramping up and ramping down the beam) [48] using the TFB system working as an AC-dipole. The excitation amplitude induced by the BBQ kicker will depend on the maximum kicker strength, while in the case of the TFB the amplitude will depend both on the angular kick strength, the difference in the frequency values (ΔQ) and the values of the β functions at the AC-dipole [87].

Transverse feedback has been the main excitation source thanks to its two main advantages: a larger driven amplitude for the same given voltage and a larger number of turns acquired thanks to the lack of decoherence. On the other hand, the operation of TFB is more complex since involves a large control of the beam tune.

6.1.2 Hardware improvements

External excitation kickers

The amplitude of the transverse driven excitation obtained during the measurements performed in 2013-14 was not large enough to accurately measure β-function based on turn-by-turn techniques and optics measurements were mainly based on orbit [128]

Prior to 2015, the maximum power delivered by the TFB power amplifier was 100 W. In order to increase the driven oscillations amplitude, the transverse feedback power amplifiers have been upgraded from an initial power to a nominal final value of 800 W. The internal TFB amplifier has been upgraded in two steps: in 2016 and 2017 the power amplifier was only operational in vertical plane and, finally, in 2018 it became fully operational in both planes. The larger driven voltage allowed to increase the peak-to-peak beam response without having to reduce the ΔQ and therefore without exciting resonances.

Nonetheless, during 2018 studies, it was found that the power amplifier started saturating for input voltages larger than 2 V and, therefore, the input voltage value was kept under this value. A frequency analysis of the TFB response has been analyzed in [130]. This analysis concludes that there was no remarkable jitter in the driven tune, but however, there is a considerable pollution of higher order modes.

The strength of the power amplifier connected to the single kick magnet has been also increased allowing to obtain a larger peak to peak amplitude. In this case the limitation is the number of turns available for the analysis. An attempt of increasing the length of the excitation before the beam completely decoheres was performed by changing the sextupole configuration. Different values in a range of 0 to 90 A were tested without obtaining a clear improvement in number of turns available for the analysis. Figure 6.3 shows that due to the dechorence effects, the number of turns available for Fourier analysis is only about 500 turns while in case of the transverse feedback it is possible to analyze 5000 turns.

BPM upgrades

The new BPM system installed in 2015 at the PSB produces turn-by-turn trajectories for individual bunches over the full acceleration cycle since the old analog to digital converters were replaced by new ones that deliver a continuous sample stream at a rate of the order of 100 MS/s (mega samples per second), i.e. 100 times faster than the beam revolution frequency. BPM gain can be optimized for different beam intensity values in order to keep the noise to signal ratio as low as possible. The gain calibration of the BPMs cannot be done separately for the two channels associated to each channel: Σ channel proportional to the beam intensity and Δ value proportional to the difference. Therefore the gain has to be carefully set in order to not overflow the ADCs associated to each channel). For typical beam displacements less than 1/10 of the beam pipe aperture, the difference Δ is smaller by about this factor compared to the sum.

Reaching a final level of the hardware settings has been an iterative work where different teams were involved. The new BPM hardware, detailed described in [131], was tested during the commissioning. The collaboration between BE-OP, BE-BI and BE-ABP allowed to improve the acquisition system including the sett up of the new excitation kicker and the new BPM ADC commissioning.

6.2 Software improvements

The performance of optics measurements in PSB has been fully automatized. New tools have been developed in order to acquire the data and to analyze it, as well several different instrumentation have been upgraded in order to improve the optics measurements accuracy.

The lattice design and especially the location of the BPMs was not originally designed for measuring β-functions. Several software and analysis methods have been developed in order to be able to measure the β-function with a 5% resolution requested by the PSB Operations team. Several improvement were required in all the different steps of the acquisition-analysis process. A summary of the different software upgrades performed at different stages of the measurement process are described below and have been summarized in Fig. 6.4.

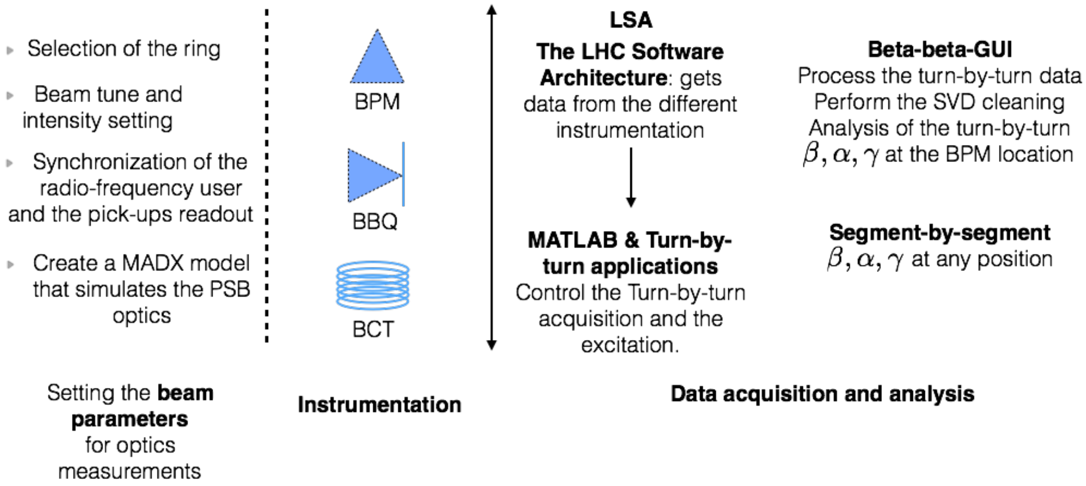

Figure 6.4: Optics measurements procedure in PSB.

- **Setting the beam parameters for optics measurements**

  SA new BPM turn-by-turn application has been fully developed. This new application combines all the functionality required during the optics measurements: selection of the ring, BPM gain, beginning of the acquisition (time), number of turns being recorded. Additional beam parameters such as the intensity, the tune or the chromaticity are configured in a different software. Different studies have been performed in order to optimize the beam intensity used during the optics-measurements. For the given energy of 160 MeV, the BPM resolution will delimit the region of intensity operation. A study of the performance of the BPMs was performed for a range of intensities of 100-250 $\cdot 10^{10}$ for the four rings, without observing a direct impact on the resolution while changing the beam intensity within that range thanks to the BPM gain suggestion that is evaluated automatically. Improvement on the creation of a MADX model for each different working point and excitation value. The model can now be created using a graphic interface that allows to obtain the lattice parameters for a given natural tune and external tune values. These lattice parameters are later used for the optics analysis [132] (accelerator class).

- **Instrumentation**

  - Improvement in the data conversion from raw analogue signal to data accessible in the Front-End Software Architecture (FESA) [133]. BPM granularity has been increased from 0.1 mm to the maximum number of digits allowed by the ADC converter. This improvement enhances the BPM resolution from an average of 0.05 mm to 0.03 mm.

- **Analysis**

  - Adaptation of the existing LHC code analysis code: signal analysis and optics computation based on Fourier analysis. The Single-Value-Deconponsition (SVD) [129] has been adapted by decreasing the number of modes that are kept and that are considered to be related to physics parameters of the beam motion. Additionally, the β^{ϕ} code has been modified in order to adapt the number of BPMs used for the β-function analysis. The β^{ϕ} combined the information from phase advances between three BPMs located at different places of the machine. A summary of the most relevant errors has been created for first time for PSB in order to be able to implement the β^{ϕ} method introduced in [4] and not using [1] restricting the BPM to the neighbor BPMs.

- β function can only be directly measured at the BPM location. Nonetheless in some scenarios it is also interested to measure optics functions at a different locations. A discrepancy in the emittance measured at PSB extraction line and PS injection [17] motivated the adaptation of LHC software to PSB, that allows to obtain the optics functions at an arbitrary position. Creation of a segment-by-segment [42, 134] in order to obtain the values of the β at different element. Segment-by-segment runs MADX [109] in a part of the accelerator in between two BPM positions. The measured optical functions at the BPMs are used as boundary conditions for MADX. β function can be obtained using both β^{ϕ} and β^{A} while α and γ functions are currently only computed using phase advance measurements, and their resolution is limited by the ϕ advance value. Alternative ways of computing the α and γ function based on β^{A} and MADX are being analyzed. This method has first been developed for LHC [42] and it has been adapted to PSB.
- Creation of an script for the calculation of the optics-based-BPM calibration factors and adaptation of the code in order to apply the calibration factors to the frequency analysis.

6.3 Optics measurements procedure

6.4 Optics-measurements methods limitations in PSB

Optics functions reconstruction, both based on phase advance and amplitude, have been further developed for PSB since the beginning of the BPM commissioning. Reconstruction of β-function based on phase advance measurements is known as N-BPM method β^{ϕ} [2]. On one hand, the old β^{ϕ} error-bar calculation based on Monte-carlo simulations [2] approach has been replaced by analytical calculations [4]. The implementation of the analytic phase advance method, requires the knowledge of the systematic errors (quadrupole misalignements, sextupole misaligments and BPM misalignements) [135] that have been summarized in a error file.

The accuracy of β^{ϕ} approach is limited by the PSB lattice. PSB rings are divided into 16 equivalent cells, each of then is composed by a focusing quadrupole, defocusing quadrupole, dipoles and two BPMs (horizontal and vertical) [14, 126, 127]. PSB operational working point at 160 MeV is $Q_x = 4.18$, $Q_y = 4.30$ (showing a large dependency with beam intensity). The location of the BPMs combined with the values of the tune lead to a phase advance between consecutive BPMs close to 90°, ($\phi_{x,n} - \phi_{x,n-1} = 96.1°$ and $\phi_{y,n} - \phi_{y,n-1} = 96.3°$).
Those phase advances between consecutive BPMs represent a challenge for the β^{ϕ} method [4]. In this approach, the relation between the phase advance ϕ and the β-function is given by a cotangent function, that vanishes for $\phi = \frac{n\pi}{2}$ and goes to $\pm\infty$ for $\phi = n\pi$. The number of BPMs used in the β calculation will directly affect the accuracy of the measurements. More accurate results will be obtained for larger number of BPMs, but this will require a very precise values of the different magnetic errors and misalagniments. A compromise between this two

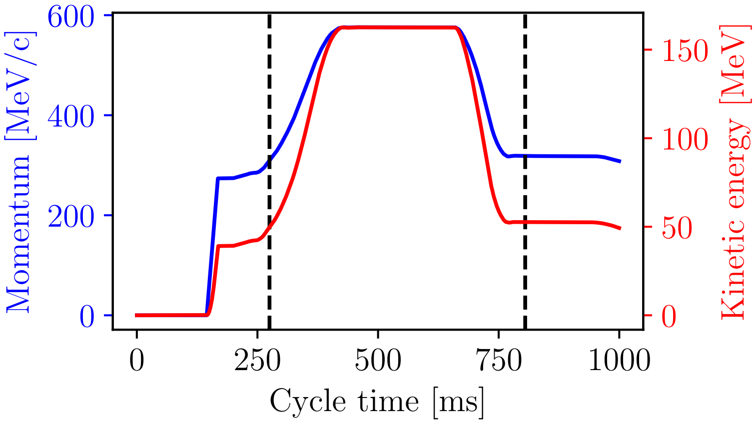

Figure 6.5: Magnetic cycle in PSB [17].

paramaters has been reached by using 5 BPMs (two to the left and two to the right of the BPM being studied).

On the other hand, the β^A method [10] has been adapted to the PSB lattice by removing the more noisy BPMs from the action calculation and by developing a dedicated optics-based-approach for obtaining the calibration factors of the BPMs.

This Chapter introduces and evaluates an optics-based-BPM approach for calculation of calibration factors based on the ratio $\beta^{\mathrm{A}}/\beta^{\phi}$. In order to obtain the BPM calibration factor it is necessary to have an accurate reference value, obtained using the β^{ϕ} method. This β^{ϕ} reference value is obtained by optimizing the phase advance between the consecutive BPMS, by changing the working point of the machine.

6.5 Operation of PSB

6.5.1 Development of a new operation cycle of PSB

A specific cycle has been developed for the performance of optics measurements. Beam is injected from LINAC at 50 MeV 275 ms after the start of the cycle and then it is ramp up to 160 MeV. This energy is reached after approximately 125 ms (or 400 ms after the start of the cycle) and it is kept constant until the 675 ms (plateau) as shown in Fig. 6.5. Optics measurements are performed during this flat part of the cycle, covering a small fraction of the plateau. Beam is ejected 530 ms after the injection.

Optics measurements have been performed using the two possible radio-frequency systems (H1 and H2) in order to maximize the stability of the machine.

An overview of the different software used in the process of acquiring, measuring and analyzing is shown in Fig. 6.4. This figure is divided in different parts associated to different steps that have to be performed during the optics measurements.

6.5.2 Developing of a new working point, Q3Q5

A more optimal phase advance for β^{ϕ} reconstruction can be achieved by moving the machine tunes. New working point aims to move the phase advance between consecutive BPMs further from 90° in order to improve the accuracy of the measurements. The new working point will be defined by the settings of the trim quadrupoles, the set of quadrupoles that are in charge of moving the working point. The maximum tune change allowed by the power supplies were $Q_x = 3.38$ and $Q_y = 5.47$ at 160 MeV, moving the phase advance to $\Delta\phi_x = 14°$ and $\Delta\phi_y = 32°$ with respect to 90°. Change in the measured phase advance between consecutive neighbours when changing the working point is shown in Fig. 6.6.

A comparison of horizontal and vertical phase advance in the optics Q3Q5 and Q4Q4 is shown in Fig. 6.6, where it can be seen that the phase advance between consecutive BPMs moves from 90 °. Horizontal and vertical β-function are also modified when moving the working point, as it can be seen in Fig. 6.7.

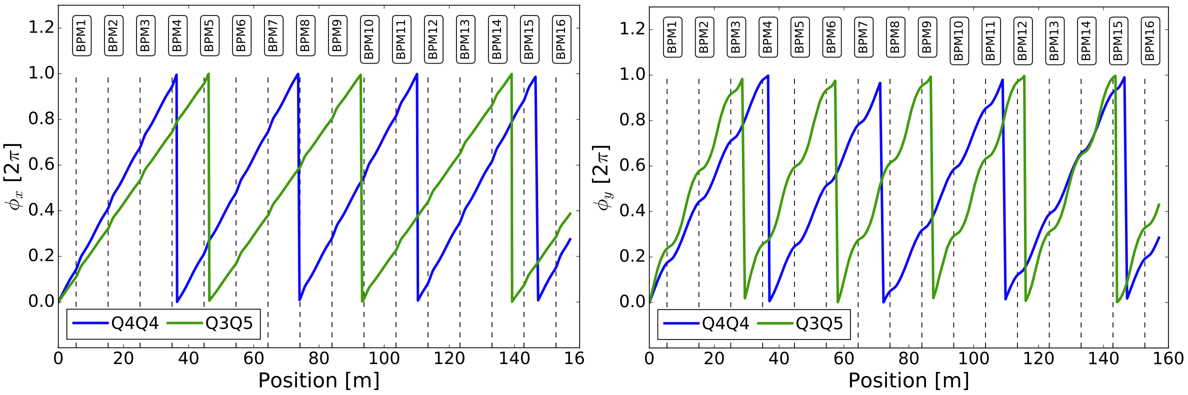

Figure 6.6: Phase advance at the two different working points Q3Q5 and Q4Q4.

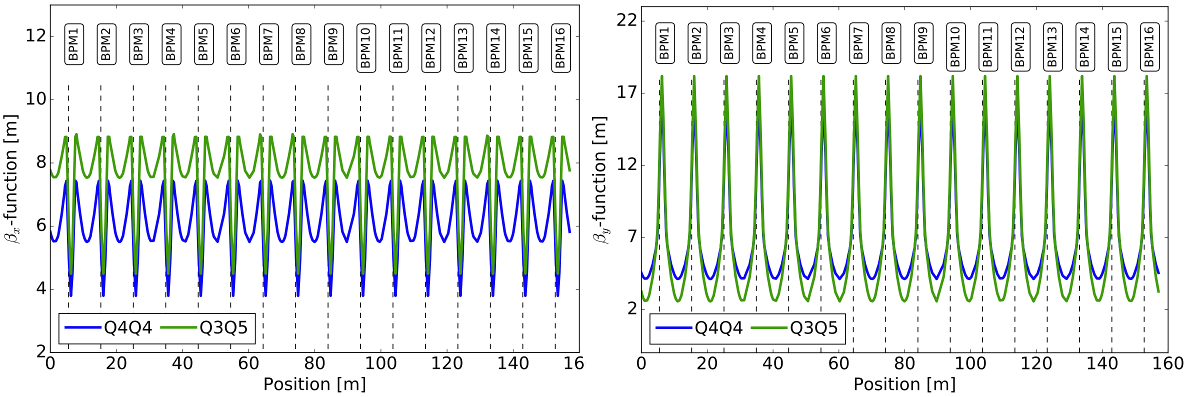

Figure 6.7: β-function at two different working points Q3Q5 and Q4Q4.

Analysis of the PSB stability

One of the main limitations that we had to face during the commissioning was the lack of the stability of the machine. PSB MD are performed in parallel with many other users and the

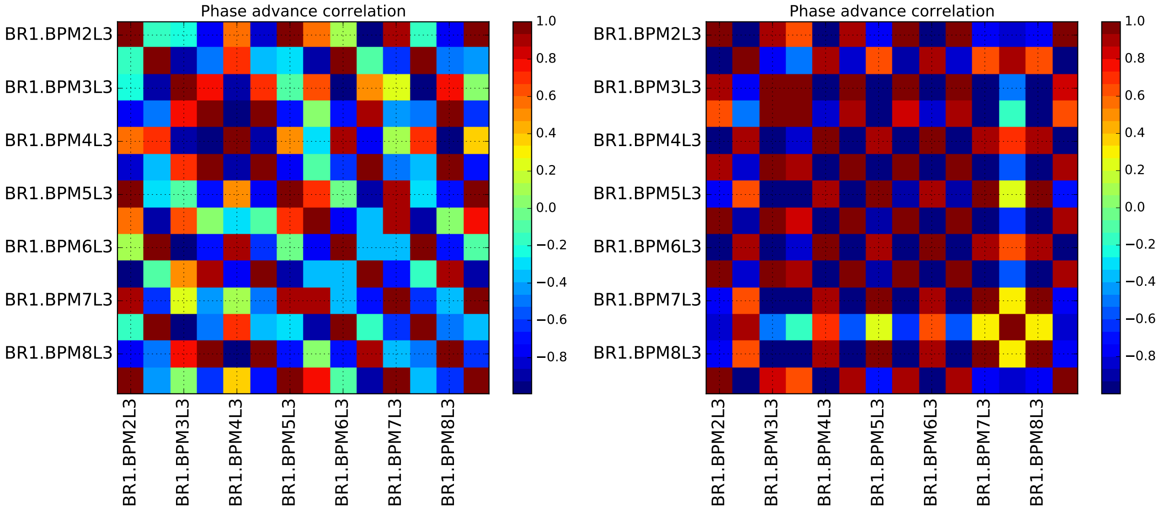

Figure 6.8: Phase advance stability using correlation between phase advance measured in consecutive acquisitions (Q3Q5): Horizontal (left), vertical (right).

time dedicated to each user is limited in one supercycle. During one cycle in the supercycle, the beam is injected and extracted. The intensity of the beam is fixed by the number of turns being injected from LINAC and by the efficiency of the injection process. Due to lack of reproducibility of the machine, even if the number of turns is kept constant, the intensity in every measurement may vary in a range of 10%. Intensity fluctuations lead to changes in the tune, and in consequnce, to a different values in the Δ (difference between the natural and the driven tune). The stability of the injection LINAC (LINAC4) to PSB also plays a very important roll in the accuracy of the measurements. Tune stability depends on the intensity fluctuations that, at the same time, depend on the injection efficiency.

Correlation matrix

The effects of the lack of stability have been studied by analyzing the phase advance correlation matrix (between two given BPMs). Because the phase advance are equally spaced in terms of phase advance, a correlated phase advance fluctuation should have an equal impact on all the BPMs. On the other hand, arbitrary change in the phase advance (not correlated) will be extremely difficult to correct and will present a limitation for the method, affecting the accuracy of the results.

The study of the stability of the machine has been analyzed for the Q4Q4 working point (Fig. 6.8) and the working point Q3Q5 (Fig. 6.9). In both cases, the change of phase advance between two BPMs in consecutive measurements is not correlated and therefore these fluctuations will have a great impact on the optics measurements accuracy.

6.6 Measurement procedures and results

Optics measurements have been performed in several days in order to find the optimal settings both for the beam intensity and the external kickers [136, 137].

On one hand, different studies have been performed with different intensities within a range of

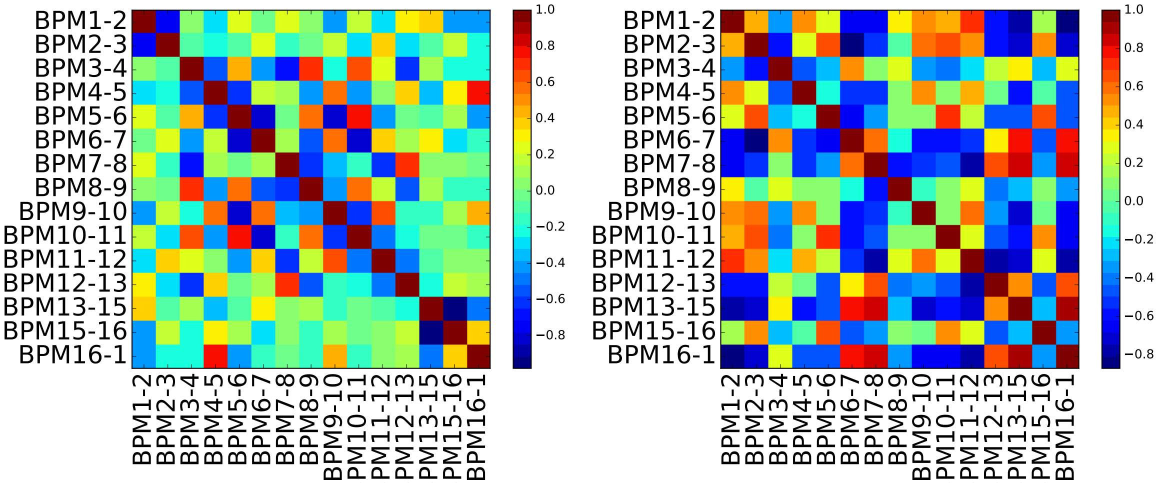

Figure 6.9: Phase advance stability using correlation between phase advance measured in consecutive acquisitions (Q4Q4): Horizontal (left), vertical (right).

100 $\cdot 10^{10}$ – 250 $\cdot 10^{10}$ particles per bunch (ppb) and with different external frequency kickers. The efficiency of the injection (from LINAC4 controlled by the numbers of turns that are being injected) it is not constant, leading to a relative fluctuation of ± 10%. The observed detuning, for this range of intensities, is 2 $\cdot 10^{-3}$ in the horizontal plane and 1 $\cdot 10^{-2}$ in the vertical plane. A clear tendency between the BPM resolution and the intensity has not been observed in this intensity range, therefore the lower intensity has been selected for the studies in order to decrease the space charge effects.

The distance between the external tune and the natural frequency, $\Delta Q_{x,y}$, should be large enough to induce large excitation within triggering a resonance. The optimal ΔQ should not be within the natural tune range of values. The most used ΔQ tunes during the optics measurements for both were: ΔQ_x = -4$\cdot 10^{-3}$ and ΔQ_y = +4$\cdot 10^{-3}$. Stability issues were addressed during the first turn-by-turn acquisitions. Optimization in the lattice (octupolar current, harmonics) were needed in order to find stable conditions with the highest charge per bunch.

Performance of optics measurements in all the 4 rings started once the final settings were optimized. Measurements have been first performed in the working point Q3Q5, in order to obtain the calibration factors of all the 4 rings. Since the first prototypes of new ADC converters were first installed in Ring 2, this has been the ring that has been most studied and that will be used as an example for the other 3 rings.

During the measurements performed at both Q4Q4 and Q3Q5 a larger noise level was observed for three BPMs: “BPM4”, “BPM6”, “BPM15”. The difference in noise with respect to the other BPMs is larger in the new working point distorting the turn-by-turn data, not allowing to measure the β function accurately. One possible explanation BPMs failure could be given by the fact that those BPMs are connected to the radial loop feedback that stabilize the beam specially in the working point Q3Q5 where the beam is less stable. Since the reason of the BPM malfunctioning is not clear and the additionally noise has not been filtered using SVD cleaning, the BPM has been removed from the analysis in the Q3Q5 in order to affect the rest of the BPMs both in the β^{ϕ} and the β^{A} method. This effect has not been as strongly observed in the Q4Q4 working point and therefore the BPMs in that scenario have not been removed.

A study of the phase advance uncertainty has been performed in order to understand the effect of the machine stability in the measurements as opposed to the error introduced by the phase advance value. Figure 6.10 and Tab. 6.1 summarizes the phase advance uncertainties measured in the 4 rings for both planes and both working points Q4Q4 and Q3Q5. The lack of stability in the new working point increases the statistical component of the error-bar, leading to a larger than expected error-bar

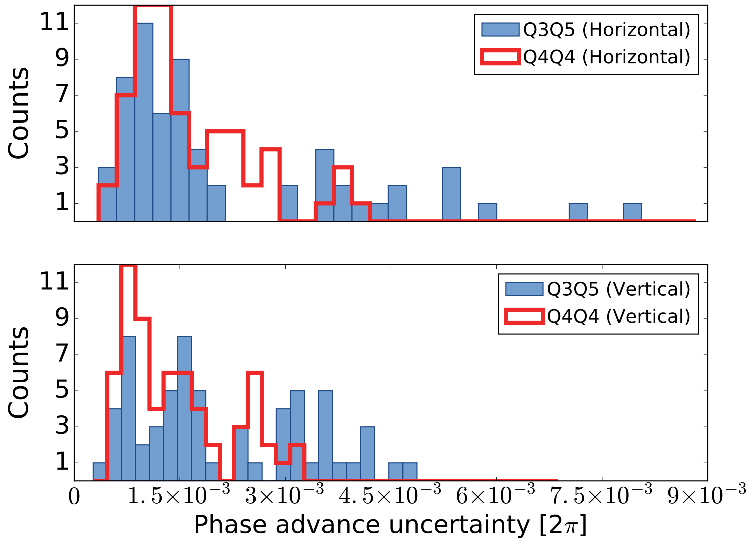

Figure 6.10: Horizontal and vertical phase uncertainty for all rings.

	r.m.s $(\sigma(\phi_{x,ij}))$	r.m.s $(\sigma(\phi_{y,ij}))$
Q3Q5	$1.4 \cdot 10^{-3}$	$1.4 \cdot 10^{-3}$
Q4Q4	$0.8 \cdot 10^{-3}$	$0.8 \cdot 10^{-3}$

Table 6.1: Summary of phase-advance error in 2π units measured in September and October in Ring 2 for the working point Q3Q5 and Q4Q4.

6.6.1 Working point Q3Q5

β^{ϕ} Q3Q5 measurements using β^{ϕ} and β^{A}

β functions measured in both horizontal and vertical planes in ring 2 are shown in Fig. (6.11). Rings 1, 3 and 4 have the same optics configuration and for simplicity they will not be included in this chapter.

Calibration factors

Electronic calibration factors, that relate the voltage difference induced in the pick-up with the beam position, [131] depends on the geometry of the pick-up. The previous geometric calibration factor value used during the turn-by-turn measurements (2015) were measured during their installation. Optics-based-calibration calculation approach aims to provide a method for keeping track of the BPM calibration factors changes with time in a fast and non-invasive way. The fundamentals of this approach are described in Ch. 4, and they have been measured for

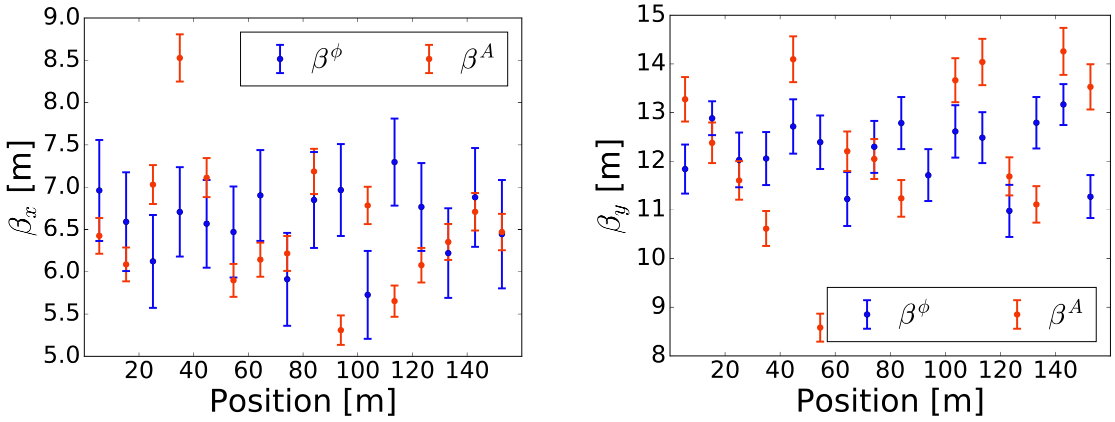

Figure 6.11: Horizontal β function measured as a function of position for two different working points Q3Q5: β^{ϕ} (top), β^{A} (bottom) (Ring 2).

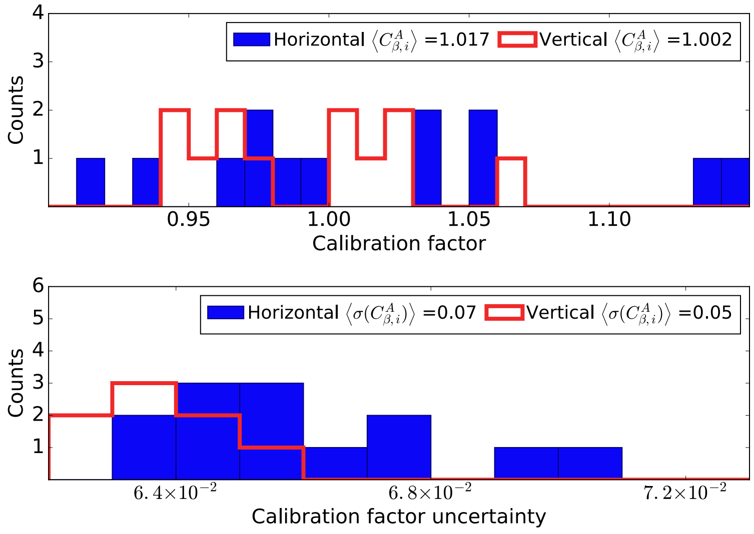

Figure 6.12: Calibration factors and calibration factors uncertainty measured (Ring 2).

all the rings using the optics functions measured at Q3Q5. Spread of both calibration factors and their associated error bar have been analyzed for all the rings. Figure 6.12 shows the calibration factors (top) and their associated errors (bottom) measured in Ring 2 as a sample for all the rings. Measurement calibration factor uncertainty is dominated by the uncertainty of the β^{ϕ} and β^{A}-function, limiting the average calibration factor resolution to a 6% ± 1% in both horizontal and vertical plane for the 4 rings.

6.6.2 Working point Q4Q4

Once the calibration factors were computed using the β functions in the working point Q3Q5, optics functions were measured in Q4Q4.

Figure 6.13 shows the β-functions measured with three different techniques: β^{ϕ}, β^{A} and $\beta^{\mathrm{A,calibrated}}$ in the horizontal and vertical plane in the Ring 2. As in the previous section, this ring will be used as a representative sample of the 4 rings. A more quantitative analysis of the results obtained using the three techniques including the rms β-beating and the average

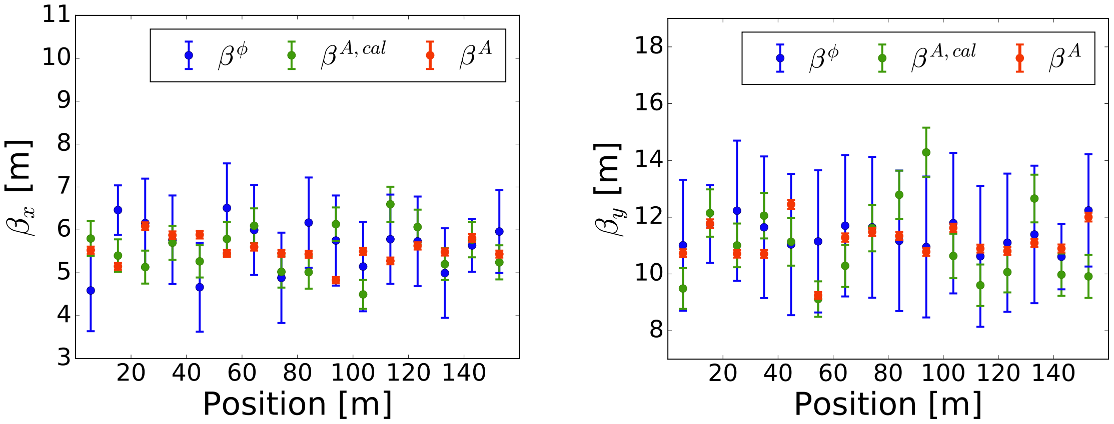

Figure 6.13: β function measured as a function of position: β^{ϕ}, β^{A} and $\beta^{A,cal}$.

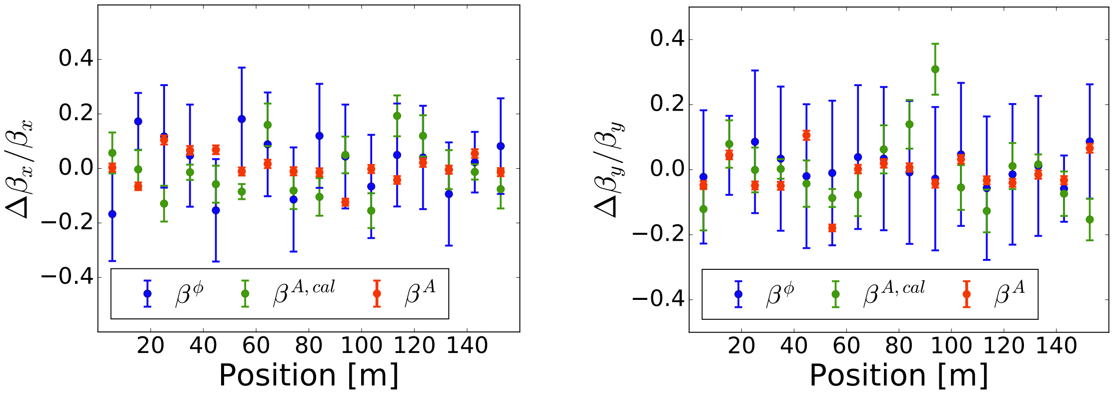

Figure 6.14: β-beating measured as a function of position: β^{ϕ}, β^{A}, $\beta^{A,cal}$.

β-error bar is summarized in Tab. 6.2. The β-beating, ilustrated in Fig. 6.14, is defined as $(\beta^{\mathrm{meas}} - \beta^{\mathrm{MADX}})/\beta^{\mathrm{MADX}}$ where β^{meas} refers to the β measured using three different approaches: β^{ϕ}, β^{A}, $\beta^{A,\mathrm{cal}}$.

6.7 Conclusion

The installation of the new injection system has served as motivation for improvements in the different steps required in order to obtain the optics functions. The performance of optics measurements in the early stage of the BPMs upgrade have been a very useful tool for the commissioning of the installation of the new pick-up system, allowing to debug different synchronization issues. Additionally, all the hardware upgrades and software development de-

	Horizontal			Vertical		
	β^{ϕ}	$\beta^{A,\mathrm{cal}}$	β^{A}	β^{ϕ}	$\beta^{A,\mathrm{cal}}$	β^{A}
r.m.s. $(\frac{\Delta\beta}{\beta})\%$	11	10	5	4	11	6
average (β-errorbar) %	17	6	2	20	6	2

Table 6.2: Summary of r.m.s β-beating measured in Ring 2.

scribed in this section will allow to measure in a fast and systematic way the PSB optics just after the start of the RUN 3. The measurement acquisition has improved the automatizing of the measurements allowing to perform faster measurements. All these improvements will be very useful in the detection of any possible problem when injecting the beam from Linac4.

On the other hand, the poor stability of the machine in the working point Q3Q5 is a limiting factor while computing the calibration factors. Several sources contribute to the machine instability, but only one of them has been identified: fluctuations in the intensity of the beam injected. Figure 6.1 shows that the error-bar associated to the new working point should be approximately 5 times smaller than the measured in the nominal working point. Nonetheless, only a factor of 2 is observed mainly due to the lack of stability of the new working point. Fluctuations in the machine over time affects both the phase advance measurements and the amplitude measurements. β-function reconstruction based on the phase advance are more solid against machine variations since this approach relays on relative quantity, phase advance between two BPMs. In case of the amplitude approach, machine instabilities will impact directly the precision of the measurements, obtaining readout far from the value of the real β-function.

Machine instabilities at Q3Q5 have an impact on the calibration factors calculation that will propagate to the $\beta^{\mathrm{A,cal}}$ measured in Q4Q4. This effect can be observed by comparing two quantities: the average β^{A} errorbar before and after the BPM re-calibration and the rms β-beating of β^{A} with respect to the β^{ϕ}, before and after the BPM re-calibration. An increase in the error-bar after re-calibrating the BPMs is introduced in the propagation of the calibration factor error-bars. On the other hand, the increase in the rms β-beating when using $\beta^{\mathrm{A,cal}}$ is due to the calibration fluctuations. These two quantities are summarized in Tab. 6.2 both for horizontal and for vertical plane.

The lack of stability of the alternative working point Q3Q5 might introduce in some cases possible outliers, as it can be seen in Fig. 6.12. An improvement in the stability of the machine in the working point Q3Q5 will also improve the precision of the $\beta^{\mathrm{A,cal}}$ method obtaining an alternative method of β^{ϕ}, not biased by the calibration factors and within the tolerances set by the operation team.

Chapter 7

Summary of Thesis Achievements and Future Work

A novel approach of computing the calibration factors of Beam Position Monitor (BPMs) based on optics measurements has been presented in this thesis. Optics measurements and corrections are essential activities carried out in accelerators during the commissioning period and during the time allocated to improve the machine performance. Those activities allow delivering to the experiments the design luminosity within the tolerance limits. Those tolerance values are, at the same time, correlated to the optics measurements precision. The precision achieved during optics measurements is highly dependent on the optics configuration, defined by the β-function at the experiment's location (β^*). Most extensively methods used for computing the optics functions in accelerators around the world, such as the Large Hadron Collider (LHC) and its injectors are based both in the turn-by-turn approach and in K-modulation technique. β-function obtained using the phase of the turn-by-turn data in the frequency domain, β^ϕ, and K-modulation present some limitations in scenarios where knowledge of β-function is critical for the performance of the experiment. In the case of β^ϕ, this limitation on accuracy is reached when the phase advance value between a pair of BPMs i an j, $\phi_{i,j}$, is close to $n\pi$. Phase advance values in the vicinity of $n\pi$ are observed for two accelerators at CERN, in the Proton Synchrotron Booster (PSB) in regular operation and in the LHC when is running with low values of the β-function at the interaction point ($\beta^* < 60$ cm). On the other hand, K-modulation resolution is limited by the machine tune jitter that has to be kept close to 10^{-5} [45]. Results presented in [57] show that for LHC, tune stability fluctuates between 2×10^{-5} and 10^{-4} being on the limit of the required resolution.

The need for reaching a constant level of precision and accuracy for all the different optics scenarios has motivated the study and further development of an existing alternative method, denoted as β^{A}. This approach is based on the measurement of the amplitude of transverse oscillations. It has not been as extensively used as the two methods previously described since it is biased by the BPM calibration factors. BPMs are calibrated before installation to obtain the most accurate possible relation between the induced voltage in the BPMs electrodes and the position of the centre of charge [138]. Nonetheless, reconstruction of β-function using information contained in the amplitude, β^{A}, showed a systematic offset with respect reference values obtained using the phase β^ϕ or K-modulation, $\beta^{\text{K-modulation}}$. During the first optics measurements after the LHC shutdown performed in 2015 and described in detailed in Ch. 3, it was found that the ratio between the β^{A} and the other approaches- that is directly proportional to the calibration factors of the BPMs- did not agree with the BPM calibration factor specifications. By further analyzing several optics measurements in 2015, it was found that the difference between β^{A} and the reference values only depends on the BPM geometry and not on the optics configurations. A more significant discrepancy has been observed in the experimental regions, where the geometry of the BPMs differs from the geometry of the BPMs placed in the rest of the accelerator. The fact that the ratio between the measured β-functions is independent of the optics configuration motivated the developement of an alternative calibration approach, based on two optics function: β and dispersion. This approach aims to complement the existing electronic calibrations.

Optics-based-BPM calibration factors studies in LHC have involved the adaptation of an existing optics previously used for the alignment of the triplet quadrupoles denoted as Ballistic or alignment optics. Ballistic optics was first tested in 2015, and since then it has been progressively modified to extend the range of BPMs being calibrated. In the latest version of the optics, developed and implemented in 2017, the dispersion function in the IRs was not matched to 0 leading to an alternative optics function that can be used in combination with β^{ϕ} to measure calibration factors. The suitability of ballistic optics for optics calibration factors together with the commissioning of this optics carried out in 2017 have been assessed in Ch. 4. Calibration factors have been measured using optics-measurement-based approaches both in Beam 1 and Beam 2 in IR1 and IR5, achieving a sub-per cent uncertainty. Accuracy of those calibration factors has been assessed by computing the relative difference between the β^{A} and a reference value, β^{ϕ} and $\beta^{\text{K-modulation}}$. An average reduction of 6% has been observed in this relative difference after re-calibrating the BPMs using optics-measurement-based techniques. The effect of re-calibrating the BPMs using optics-measurement-based approaches on the β^{A} has been analyzed in detail in Ch. 4

Calibration factors measured using β-function ratio, $\sqrt{\beta^{\mathrm{A}}/\beta^{\phi}}$ have been validated computing the ratio between dispersion function and normalized dispersion, $D_x/ND_x\sqrt{\beta_x}$. Nonetheless, the large error-bars associated with the dispersion measurements propagate directly to the calibration factor calculations affecting the accuracy of the measurements.

Analysis of BPM calibration factors, based on optics measurements, has led to fruitful discussions and collaborations with the CERN team that is in charge of the BPM system. The results introduced in Ch. 4 will be used during Run III to improve not only the β^{*} measurements but also the operation. Additionally, detailed information about the limitations of the BPM system that have been observed while performing optics measurements will be used as an input for the new BPMs that will be installed in the HL-LHC.

Optics-based-BPM calibration factors studies in PSB involved hardware upgrade and software developments. The commissioning of the PSB optics measurements has been successfully performed. The optics configuration developed for computing the calibration factors consisted of moving the working point, i.e. the horizontal and vertical tunes. Measurements performed in this new working point presented some limitations due to the beam instability in the new optics configurations. The radial feedback system, in charge of mitigating the instabilities, is connected to three BPMs also used for performing optics measurements. It has been found that the noise level of those BPMs is larger than the average value altering the turn-by-turn signal recorded, not allowing to compute the calibration factors values accurately. Nonetheless, results obtained in the four rings using the new technique $\beta^{\mathrm{A,calibrated}}$ shows a decrease in the β uncertainty of almost a factor three with respect to β^{ϕ} technique.

Additional activities had to be performed in PSB to obtain a sufficiently large beam response that will allow measuring the optics functions accurately. Those activities covered the installation of different hardware elements, including the new ADC converters in the BPMs, the external beam exciters and a system dedicated to measurement acquisition. Software used for measurement acquisition and analysis have been developed to simplify the optics measurements procedure. The improvements implemented in the machine, together with the in-depth analysis of the β^{A} error-bar will allow to speed up the commissioning of the new injection scheme at the beginning of Run III.

In summary, the present work completes the β^{A} approach by computing optics-based-calibration factors and by further analyzing the error-bar associated with this method. The revisited β^{A} approach aims to give an accurate value of the β-function covering all possible operational scenarios presented in accelerators that are currently operating such as PSB, PS and LHC and future generators of accelerators.

Bibliography

[1] P. Castro-Garcia. *Luminosity and beta function measurement at the electron - positron collider ring LEP*. PhD thesis, CERN, 1996.

[2] A. Langner and R. Tomás. "Optics measurement algorithms and error analysis for the proton energy frontier". *Phys. Rev. Spec. Top. Accel. Beams*, 18(CERN-ACC-2015-0031), Mar 2015. https://cds.cern.ch/record/2002473.

[3] A. Langner, G. Benedetti, M. Carl, J. M. Coello de Portugal, U. Iriso, Z. Mart, and R. Tomás. "Optics Measurement using the N-BPM Method for the ALBA Synchrotron". (CERN-ACC-2015-329):MOPJE057. 4 p, 2015. http://cds.cern.ch/record/2141785.

[4] A. Wegscheider et al. "Analytical N beam position monitor method". *Phys. Rev. Accel. Beams*, 20(11):111002. 10 p, 2017. https://cds.cern.ch/record/2307554.

[5] M. Kuhn, V. Kain, A. Langner, and R. Tomás. "First K-Modulation Measurements in the LHC During Run 2". page MOPB046. 4 p, 2016.

[6] L. Malina, J. Coello de Portugal, T. Persson, P. K. Skowroski, R. Tomás, A. Franchi, and S. Liuzzo. Improving the precision of linear optics measurements based on turn-by-turn beam position monitor data after a pulsed excitation in lepton storage rings. *Phys. Rev. Accel. Beams*, 20(8):082802, 2017.

[7] P. C. V. Thrane, R. Tomás, and J. A. Stvneng. *"Measuring β^* in SuperKEKB with K Modulation"*. PhD thesis, Dec 2018. http://cds.cern.ch/record/2652855.

[8] R. W. Assmann, S. D. Fartoukh, and F. Zimmermann. "Measuring Beta Functions and Dispersion in the Early LHC". (LHC-Project-Report-586. CERN-LHC-Project-Report-586):4 p, Jul 2002. https://cds.cern.ch/record/569463.

[9] A. Franchi. "Error analysis of linear optics measurements via turn-by-turn beam position data in circular accelerators". 2016. arXiv 1603.00281.

[10] A. García-Tabarés Valdivieso and R. Tomás. Optics-measurement-based bpm calibrations. to be published, 2018.

[11] A. García-Tabarés Valdivieso, L. Malina, et al. "MD Test of a Ballistic Optics". Jan 2016.

[12] A. García-Tabarés, F. Carlier, J. M. Coello de Portugal, et al. "Optics-measurement-based BPM Calibration". (CERN-ACC-2016-188):THPMB041. 4 p, 2016.

[13] A. García-Tabarés, P.K. Skowroski, and R. Tomás. "Optics Measurements in the CERN PS Booster Using Turn-by-Turn BPM Data". In *Proc. 10th International Partile Accelerator Conference (IPAC'19), Melbourne, Australia, 19-24 May 2019*, pages 285–288. https://doi.org/10.18429/JACoW-IPAC2019-MOPGW080.

[14] M. Mcateer. *Linear Optics Measurements in the Fermilab Booster and the CERN PS Booster.* PhD thesis, 2014.

[15] A. Santamaria Garcia et al. Identification and compensation of betatronic resonances in the proton synchroton booster at 160 MeV. In *Proceedings, 10th International Particle Accelerator Conference (IPAC 2019): Melbourne, Australia, May, 2019*, 2019.

[16] H Burkhardt. Overiew of the LHC injection and transfer line optics configurations and tolerances. 2005. https://cds.cern.ch/record/986626.

[17] A. Santamaría. Emittance measurements in the PS. `https://indico.cern.ch/event/706213/contributions/2897724/attachments/1617487/2580063/LIU_MDday2018_emittance_PSB_final.pdf`. Presented in LIU MD Day.

[18] M. Stanley Livingston. "Early history of Particle Accelerators". In *Advances in Electronics and Electron Physics*, number 50, pages 1–88, 1980.

[19] Geneva, 1994. CERN Accelerator School : 5th General Accelerator Physics Course http://cds.cern.ch/record/235242.

[20] R. W Hamm and M. E Hamm. *"Industrial accelerators and their applications"*. World Scientific, Singapore, 2012. https://cds.cern.ch/record/1477757.

[21] O. Barbalat. "Applications of particle accelerators". (CERN-AC-93-04-BLIT-REV), Feb 1994. https://cds.cern.ch/record/260280.

[22] G. Aad et al. "Observation of a new particle in the search for the Standard Model Higgs boson with the ATLAS detector at the LHC". *Phys. Lett.*, B716:1–29, 2012.

[23] S. Chatrchyan et al. "Observation of a new boson at a mass of 125 GeV with the CMS experiment at the LHC". *Phys. Lett.*, B716:30–61, 2012.

[24] R. Aaij et al. "Evidence for exotic hadron contributions to $\Lambda_b^0 \to J/\psi p \pi^-$ decays". *Phys. Rev. Lett.*, 117(8):082003, 2016. [Addendum: Phys. Rev. Lett.118,119901(2017)].

[25] E. Wilson. *"An Introduction to Particle Accelerators"*. Oxford University Press, Singapore, 2013.

[26] M. Karl H. Chao, A. Wu and Frank Tigner, M. Zimmermann. *"Handbook of accelerator physics and engineering; 2nd ed."*. World Scientific, Singapore, 2013.

[27] S. Y. Lee. *"Accelerator physics; 4th ed."*. World Scientific, Singapore, 2019.

[28] H. Wiedemamm. *"Particle accelerator physics, 4th edition"*. Springer, 2015.

[29] E. D. Courant and H. S. Snyder. "Theory of the Alternating-Gradient Synchrotron". *Ann. Phys.*, 3:1–48, 1958.

[30] O. S. Bruning, P. Collier, P. Lebrun, S. Myers, R. Ostojic, J. Poole, and P. Proudlock. *“LHC Design Report: volume 1”*. CERN Yellow Reports: Monographs. CERN, Geneva, 2004. http://cds.cern.ch/record/782076.

[31] O. S. Bruning, P. Collier, P. Lebrun, S. Myers, R. Ostojic, J. Poole, and P. Proudlock. *“LHC Design Report: volume 2”*. CERN Yellow Reports: Monographs. CERN, Geneva, 2004. http://cds.cern.ch/record/815187.

[32] M. Benedikt, P. Collier, V. Mertens, J. Poole, and K. Schindl. *“LHC Design Report: volume 3”*. CERN Yellow Reports: Monographs. CERN, Geneva, 2004. http://cds.cern.ch/record/823808.

[33] G. Apollinari, I. Béjar Alonso, O. Bruning, P. Fessia, M. Lamont, L. Rossi, and L. Tavian. *“High-Luminosity Large Hadron Collider (HL-LHC): Technical Design Report V. 0.1”*. CERN Yellow Reports: Monographs. CERN, Geneva, 2017. http://cds.cern.ch/record/2284929.

[34] F. Zimmermann et al. “High-Energy LHC Design”. *J. Phys. : Conf. Ser.*, 1067(CERN-ACC-2018-150. 2):MOPMF064. 8 p, 2018.

[35] M. Benedikt and F. Zimmermann. “FCC: Colliders at the Energy Frontier”. (IPAC-2018-THYGBD1. CERN-ACC-2018-095):THYGBD1. 6 p, 2018.

[36] A. Seryi et al. “Overview of Design Development of FCC-hh Experimental Interaction Regions”. In *Proceedings, 8th International Particle Accelerator Conference (IPAC 2017): Copenhagen, Denmark, May 14-19, 2017*, page TUPVA040, 2017.

[37] *Cern Document Service: ATLAS.*

[38] *Cern Document Service: ALICE.*

[39] *CMS collaboration web.*

[40] *LHCB collaboration web.*

[41] J. M. Coello de Portugal, F. Carlier, A. García-Tabarés, A. Langner, E. Maclean, L. Malina, T. Persson, Piotr Skowroski, and R. Tomás. “Local Optics Corrections in the HL-LHC IR”. (CERN-ACC-2016-176):THPMR040. 4 p, 2016. http://cds.cern.ch/record/2207447.

[42] A. Langner, J. M. Coello de Portugal, Piotr Skowroski, and R. Tomás. “Developments of the Segment-by-Segment Technique for Optics Corrections in the LHC”. Number CERN-ACC-2015-331, page MOPJE054. 4 p, 2015. http://cds.cern.ch/record/2141783.

[43] J. M. Coello de Portugal, F. Carlier, A. Langner, T. Persson, Piotr Skowroski, and R. Tomás. “OMC Software Improvements in 2014”. (CERN-ACC-2015-330):MOPJE056. 4 p, 2015. http://cds.cern.ch/record/2141784.

[44] R. Tomas et al. “Record low beta beating in the LHC”. *Phys. Rev. ST Accel. Beams*, 15:091001, 2012.

[45] F. Carlier and R. Tomás. “Accuracy and feasibility of the β^* measurement for LHC and High Luminosity LHC using k modulation”. *Phys. Rev. Accel. Beams*, 20(1):011005. 11 p, 2017.

[46] M. Hofer et al. “K-Modulation for future High energy colliders”. In *Proceedings, 10th International Particle Accelerator Conference (IPAC 2019): Melbourne, Australia, May, 2019*, 2019.

[47] R. Tomás, M. Aiba, A. Franchi, and U. Iriso. Review of linear optics measurement and correction for charged particle accelerators. *Phys. Rev. Accel. Beams*, 20(5):054801, 2017.

[48] R. Tomas. “adiabaticity of the ramping process of an ac dipole”. *Physical Review Special Topics Accelerators and Beams*, 8:24401, 01 2005.

[49] J. Irwin, C X. Wang, Yiton Yan, Karl Bane, Yue Cai, F.-J Decker, Michiko Minty, G V. Stupakov, and F. Zimmermann. “model-independent beam dynamics analysis”. *Physical Review Letters - PHYS REV LETT*, 82:1684–1687, 02 1999.

[50] X. Shen, M Bai, S.Y Lee, Y Luo, A Marusic, G Robert-Demolaize, R Tomás, and S White. “Application of independent component analysis to ac dipole based optics measurement and correction at the Relativistic Heavy Ion Collider”. *Phys. Rev. Spec. Top. Accel. Beams*, 16(11):111001. 10 p, 2013.

[51] A. Boccardi, E. Calvo Giraldo, M. Gasior, J. L. Gonzlez, O. R. Jones, and R. J. Steinhagen. “On the Continuous Measurement of the LHC Beta-Function - Prototype Studies at the SPS”. (CERN-ATS-2009-031):4 p, May 2009.

[52] L. Malina, J. M. Coello de Portugal, Joschua Dilly, Piotr Skowroski, R. Tomás, and Matthew Toplis. Performance Optimisation of Turn-by-Turn Beam Position Monitor Data Harmonic Analysis. In *Proceedings, 9th International Particle Accelerator Conference (IPAC 2018): Vancouver, BC CA.da, April 29-May 4, 2018*, page THPAF045, 2018.

[53] A. García-Tabarés and R. Tomas. “Optics-measurement-based BPMs calibrations”.

[54] W. J. Corbett, M. J. Lee, and V. Ziemann. “A Fast model calibration procedure for storage rings”. *Conf. Proc.*, C930517:108–110, 1993. [,108(1993)].

[55] W Weterings et al. “Operational considerations for the PSB H- Injection System”. (LHC-PROJECT-Report-0006. CERN-LHC-PROJECT-Report-0006):4 p, Jun 2009. https://cds.cern.ch/record/1203023.

[56] M. Kuhn, V. Kain, A. Langner, and R. Tomás. “First K-Modulation Measurements in the LHC During Run 2”. In *Proceedings, 4th International Beam Instrumentation Conference, IBIC2015*, page MOPB046, 2016.

[57] D. W. Wolf, R. Tomás Garcia, Gnter Quast, and A.-S. Mller. *Analysis of tune modulations in the LHC. Analyse von Tune-Modulationen im LHC*. PhD thesis, Nov 2018. Presented 21 Nov 2018.

[58] R. Calaga, R. Tomás, and F. Zimmermann. “BPM calibration independent LHC optics correction”. (LHC-PROJECT-Report-1039. CERN-LHC-PROJECT-Report-1039):4 p, 2007.

[59] M. Aiba, S. Fartoukh, A. Franchi, M. Giovannozzi, V. Kain, M. Lamont, R. Tomás, G. Vanbavinckhove, J. Wenninger, F. Zimmermann, R. Calaga, and A. Morita. “First β-beating measurement and optics analysis for the cern large hadron collider”. *Phys. Rev. ST Accel. Beams*, 12:081002, Aug 2009.

[60] B. Mikulec, A. Findlay, V. Raginel, G. Rumolo, and G. Sterbini. “Tune spread studies at injection energies for the CERN proton synchroton booster.”. In *Proceedings of HB12*, page MOP249, 2012.

[61] H. Damerau et al. LHC Injectors Upgrade, Technical Design Report, Vol. I: Protons. Technical Report CERN-ACC-2014-0337, Dec 2014. https://cds.cern.ch/record/1976692.

[62] *Cern Document Service: LHCf.*

[63] G. Antchev and others (TOTEM collaboration). Totem upgrade proposal (2013), 2013.

[64] *“MoEDAL collaboration homepage”.*

[65] M. Solfaroli Camillocci, S. Redaelli, R. Tomás, and J. Wenninger. “Combined Ramp and Squeeze to 6.5 TeV in the LHC”. (CERN-ACC-2016-242):TUPMW031. 4 p, 2016. http://cds.cern.ch/record/2207383.

[66] M. Cieslak-Kowalska et al. Evolution of High Intensity Beams in the CERN PS Booster after H^- Injection and Phase Space Painting. In *Proc. of International Particle Accelerator Conference (IPAC’16), Busan, Korea, 2016*, number 7 in International Particle Accelerator Conference, pages 656–659. JACoW. doi:10.18429/JACoW-IPAC2016-MOPOR024.

[67] *“ISOLDE collaboration web.*

[68] B. Mikulec et al. “Commissioning and Results of the Half-Sector Test Installation with 160 MeV H beam from Linac4”. (CERN-ACC-2017-276):MOPIK047. 4 p, 2017. https://cds.cern.ch/record/2289129.

[69] M. Benedikt and G Métral. “Cycling of the PS complex and the SPS Analysis and possibilities for optimisation”. Technical Report AB-Note-2004-061. CERN-AB-Note-2004-061, CERN, Geneva, Aug 2004.

[70] B. Mikulec, A. Blas, C. Carli, A. Findlay, K. Hanke, G. Rumolo, and J. Tan. “LHC Beams from the CERN PS Booster”. 04 2019.

[71] H. Schmickler. “Beam Position Measurement System Design”. page THALA01. 7 p, 2016.

[72] G. Castorina, G. Franzini, Marco Marongiu, A. Mostacci, A. Nosych, and B. Spataro. Stripline Beam Position Monitor Modelling and Simulations for Charge Measurements. In *Proceedings, 6th International Beam Instrumentation Conference, IBIC2017*, page TUPCF16, 2018.

[73] A. A. Nosych, A. Olmos U. Iriso, and M. Wendt. “Overview of the geometrical and non-linear effects of button BPMs and methodology for their efficient suppression.”. In *Proceedings of HB14*, page TUPF03, 2014.

[74] O.R. Jones. “LHC beam instrumentation”. In *Proceedings of PAC07, Albuquerque, New Mexico, USA, PAC-07.*

[75] F. Blas et al. “Conversion of the PS complex as LHC proton pre-injector”. (CERN-PS-97-048-DI):3 p, Jun 1997.

[76] A. Boccardi, M. Gasior, O. Jones, and R. J Steinhagen. “An overview of the LHC Transverse Diagnostics Systems”. (LHC-PROJECT-Report-1166. CERN-BE-2009-002):5 p, Mar 2008. https://cds.cern.ch/record/1156346.

[77] M. Gasior and R. Jones. “The principle and first results of betatron tune measurement by direct diode detection”. Technical Report LHC-Project-Report-853. CERN-LHC-Project-Report-853, CERN, Geneva, Aug 2005. https://cds.cern.ch/record/883298.

[78] M. Gasior and J.L Gonzalez. “New Hardware of the tune measurement system for the proton synchroton booster acceleator”. September 1999. `http://mgasior.web.cern.ch/mgasior/pap/psbqm_hw.pdf`.

[79] M. Gasior. “ High Sensitivity Tune Measurement using Direct Diode Detection”. *Conf. Proc.*, C1204151(CERN-ATS-2012-246):MOAP02. 7 p, Apr 2012. https://cds.cern.ch/record/1476069.

[80] K. Wittenburg. “Beam loss monitors”. 2009.

[81] E.B. Holzer et al. Beam loss monitoring for LHC Machine Protection. *Physics Procedia*, 37:2055 – 2062, 2012. Proceedings of the 2nd International Conference on Technology and Instrumentation in Particle Physics (TIPP 2011).

[82] J. C. Denard. Beam current monitors. 2009. https://cds.cern.ch/record/1213275.

[83] Forte, V. “PSB emittance measurement techniques”. `https://indico.cern.ch/event/714395/contributions/2935656/attachments/1624661/2587042/28-03-2018-LIU_PSB_BD-V_Forte-PSB_emittance_measurement_techniques.pdf`.

[84] V. Berardi et al. *Total cross-section, elastic scattering and diffraction dissociation at the Large Hadron Collider at CERN: TOTEM Technical Design Report.* Technical Design Report TOTEM. CERN, Geneva, 2004.

[85] A. Blas and G. Kotzian. “Upgraded Transverse Feedback for the CERN PS Booster”. page WEP2PO001. 4 p, 2018. https://cds.cern.ch/record/2640829.

[86] C. Carter, C. Christiansen, J. Donnat, G. Gelato, M. Le Gras, H. O. Schnauer, and D.J. Williams. “The transverse feedback system for the CERN PS booster”. *IEEE Trans. Nucl. Sci.*, 28(CERN-PS-BR-81-5):2270–2272, 1981. https://cds.cern.ch/record/134327.

[87] R. Miyamoto, M Cattin, J. Serrano, and R. Tomas. “Signal quality of the LHC AC Dipoles and its impact on beam dynamics”. (CERN-ATS-2010-063):3 p, Jun 2010. https://cds.cern.ch/record/1269893.

[88] S. White, E Maclean, and R. Tomás. “Direct amplitude detuning measurement with ac dipole”. *Phys. Rev. Spec. Top. Accel. Beams*, 16(7):071002. 12 p, 2013. https://cds.cern.ch/record/1709423.

[89] R. Tomás, S. Fartoukh, and J. Serrano. “Reliable Operation of the AC Dipole in the LHC”. (LHC-PROJECT-Report-1095. CERN-LHC-PROJECT-Report-1095):4 p, Aug 2008.

[90] R Tomás. “Normal form of particle motion under the influence of an AC dipole”. *Phys. Rev. Spec. Top. Accel. Beams*, 5(CERN-SL-2002-008):054001. 10 p, Apr 2002.

[91] S. Monig, J. M. Coello de Portugal, A. Langner, E. Maclean, T. Persson, and R. Tomás. "Short Term Dynamic Aperture with AC Dipoles". (CERN-ACC-2016-173):THPMR044. 4 p, 2016.

[92] E. H. Maclean, R. Tomás, F. Schmidt, and T. H. B. Persson. "Measurement of nonlinear observables in the Large Hadron Collider using kicked beams". *Phys. Rev. ST Accel. Beams*, 17(8):081002, 2014.

[93] R. Miyamoto, S. E. Kopp, A. Jansson, and M. J. Syphers. "Parametrization of the driven betatron oscillation". *Phys. Rev. ST Accel. Beams*, 11:084002, Aug 2008.

[94] R. Tomás, T. Bach, R. Calaga, A. Langner, Y. I. Levinsen, E. H. Maclean, T. H. B. Persson, P. K. Skowronski, M. Strzelczyk, G. Vanbavinckhove, and R. Miyamoto. "record low β beating in the lhc". *Phys. Rev. ST Accel. Beams*, 15:091001, Sep 2012.

[95] F. Carlier et al. "LHC optics measurment and correction software progress and plans". In *Proceedings, 10th International Particle Accelerator Conference (IPAC 2019): Melbourne, Australia, May, 2019*, 2019.

[96] T. Persson and R. Tomás. "Improved control of the betatron coupling in the Large Hadron Collider". *Phys. Rev. Spec. Top. Accel. Beams*, 17(5):051004, 2014.

[97] T. Persson et al. "Automatic Correction of Betatron Coupling in the LHC Using Injection Oscillations". (CERN-ACC-2013-0045):3 p, May 2013.

[98] N. Magnin. AC-dipole upgrades. In LHC Optics Measurement and Correction Review. http://indico.cern.ch/event/246159/.

[99] T. Persson et al. "Towards automatic coupling corrections with DOROS BPMs (MD750)"". Oct 2015.

[100] P. Castro, J Borer, A Burns, G Morpurgo, and R Schmidt. "Betatron function measurement at LEP using the BOM 1000 turns facility". page 3 p, May 1993.

[101] M. Wendt. Lhc bpms status quo and introduction. WP2/WP13 meeting on LHC BPM system requirements.

[102] A. Verdier. "Alignment optics for LHC". Technical Report LHC-PROJECT-NOTE-325, CERN, Geneva, Jul 2003. http://cds.cern.ch/record/691914.

[103] L. Van Riesen-Haupt. *"Advanced Accelerator Interaction Region Optics for LHC Operation and Future Hadron Colliders"*. PhD thesis, June 2019.

[104] A. García-Tabarés Valdivieso et al. "LHC injection optics measurements at commissioning (2015)". Apr 2016.

[105] T. Persson, F. Carlier, J. Coello de Portugal, A. García-Tabarés Valdivieso, A. Langner, E. H. Maclean, L. Malina, P. Skowronski, B. Salvant, R. Tomás, and A. C. García Bonilla. "LHC optics commissioning: A journey towards 1% optics control". *Phys. Rev. Accel. Beams*, 20:061002, Jun 2017. https://link.aps.org/doi/10.1103/PhysRevAccelBeams.20.061002.

[106] J.P. Koutchouk. "Measurement of the beam position in the LHC main rings". Technical Report LHC-BPM-ES-0004, CERN, Geneva, 2002.

[107] A. García-Tabarés Valdivieso and others. “Optics measurements and corrections at $\beta^* = 2.5$ km”. Jun 2018.

[108] L. Malina et al. “Performance Optimisation of Turn-by-Turn Beam Position Monitor Data Harmonic Analysis”. page THPAF045. 4 p, 2018.

[109] MAD - Methodical Accelerator Design.

[110] R. J. Steinhagen. Tune and chromaticity diagnostics. 2009. https://cds.cern.ch/record/1213281.

[111] Chamonix 2012 Workshop on LHC Performance, 2012. https://cds.cern.ch/record/1424362.

[112] E. Bravin and J. Wenninger. “BI changes in LBOC meeting, Tuesday 25 Apr 2017”. https://indico.cern.ch/event/632455/contributions/2557667.

[113] P. Hagen et al. WISE: A simulation of the lhc optics including magnet geometrical data. 01 2008.

[114] S. Fartoukh. “Achromatic telescopic squeezing scheme and application to the LHC and its luminosity upgrade”. *Phys. Rev. Spec. Top. Accel. Beams*, 16(CERN-ACC-2013-0289):111002. 33 p, Dec 2013. http://cds.cern.ch/record/1636178.

[115] S. Fartoukh et al. “Experimental validation of the Achromatic Telescopic Squeezing (ATS) scheme at the LHC”. *J. Phys. : Conf. Ser.*, 874(CERN-ACC-2017-328. 1):012010. 7 p, 2017.

[116] D. G. d’Enterria. Forward Physics at the LHC. In *Proceedings, 15th International Workshop on Deep-inelastic scattering and related subjects (DIS 2007). Vol. 1 and 2: Munich, Germany, April 16-20, 2007*, pages 1141–1152, 2007.

[117] R. Alemany-Fernndez et al. “Cross-Calibration of the LHC Transverse Beam-Profile Monitors”. (CERN-ACC-2017-197):MOPAB130. 4 p, 2017.

[118] S. Ask. Status of the Forward Physics Projects in ATLAS. (arXiv:0706.0644):747–750. 4 p, Jun 2007. 4 pages, 2 figures. Proceedings of the XV International Workshop on Deep-Inelastic Scattering and Related Subjects, Munich, Germany, April 2007.

[119] H. Burkhardt. High-beta optics. 2011.

[120] H Burkhardt, T Persson, R Tomas, J Wenninger, and S Cavalier. Commissioning and Operation at Beta* = 1000 m in the LHC. (CERN-ACC-2013-0187):3 p, May 2013.

[121] G. Vanbavinckhove. *Optics measurements and corrections for colliders and other storage rings.* PhD thesis, Jan 2013. Presented 16 Jan 2013.

[122] J. Serrano and M. Cattin. “The LHC AC Dipole system: an introduction”. May 2010.

[123] E. Fol and others. “LHC MD 1988: Automatic coupling correction test”. Feb 2017.

[124] M. Kuhn et al. “New Tools for K-modulation in the LHC”. Number CERN-ACC-2014-0159, page 4 p, Jun 2014.

[125] E. Benedetto et al. “machine development studies in the cern ps booster, in 2016.

[126] P. Castro-Garcia. *Linear Optics Measurements in the Fermilab Booster and the CERN PS Booster.* PhD thesis, Fermilab, 2014.

[127] M. McAteer. “Linear optics measurements and preparations for nonlinear optics measurements in the PSB”, 2014. `https://ab-dep-abp.web.cern.ch/ab-dep-abp/HSS/HSS_meetings/2014/20140331/HSS%20meeting%20slides.pdf`.

[128] M. McAteer, C. Carli, B Mikulec, R Tomas, and M Aiba. “Preliminary results of linear optics from orbit response in the CERN PSB”. (CERN-ACC-2013-0055):3 p, May 2013. http://cds.cern.ch/record/1572990.

[129] L. Malina, J. M. Coello de Portugal, Joschua Dilly, Piotr Skowroski, R. Tomás, and M. Toplis. “Performance Optimisation of Turn-by-Turn Beam Position Monitor Data Harmonic Analysis”. page THPAF045. 4 p, 2018.

[130] P. Skowronski. “Status of optics measurements Part 1: Technicalities”, 2018. `https://indico.cern.ch/event/726839/contributions/2991681/attachments/1649109/2636650/20180514_PSB.pdf`.

[131] J. Belleman. A proposal for a trajectory measurement system for the ps booster”. http://jeroen.web.cern.ch/jeroen/btms/btms.pdf.

[132] PSB-MADX repository.

[133] FESA. “Front-End software architecture”. https://be-dep-co.web.cern.ch/content/fesa.

[134] P. Skowronski. 2018. `https://indico.cern.ch/event/771695/contributions/3207688/attachments/1749170/2833417/20181108_OMC.v1.pdf`.

[135] G. Piero di Giovanni. Private Communication, 2017.

[136] A. García-Tabarés. “Optics Measurements at 160 MeV”, October 2018. `https://indico.cern.ch/event/760902/contributions/3157184/attachments/1725833/2788039/presentation_psb_2018101_1.pdf`.

[137] P. Skowronski. “Status of optics measurements PSB WG 13”.

[138] A. A. Nosych et al. “Geometrical non-linearity correction procedure of LHC Beam Position Monitors”.

[139] F. Carlier, J. M. Coello de Portugal, E. Maclean, T. Persson, and R. Tomás. “Observations of Resonance Driving Terms in the LHC during Runs I and II”. (CERN-ACC-2016-179):THPMR037. 4 p, 2016. https://cds.cern.ch/record/2207444.

Appendices

Appendix A

Analysis of error-sources in β^{A}-calculation

A.1 β^{ϕ}-error propagation in action calculation

The errorbar of the $\beta^{\mathrm{D},\phi}$ will propagate to the action calculation shown in Eq. (4.10) according to:

$$\sigma_{2J^{\mathrm{D},\phi}}|_{\beta_i^{\mathrm{D},\phi}} = \frac{1}{\mathrm{N}'}\sqrt{\sum_{i=1}^{\mathrm{N}'}\left(\frac{2J_i^{\mathrm{D},\phi}\sigma_{\beta_i^{\mathrm{D},\phi}}}{\beta_i^{\mathrm{D},\phi}}\right)^2}, \tag{A.1}$$

Assuming that the action value at a BPM i, $2J_i^{\mathrm{D},\phi}$, and the β^{ϕ} relative error, $\frac{\sigma_{\beta_i^{\mathrm{D},\phi}}}{\beta_i^{\mathrm{D},\phi}}$, are not correlated, the action value can be taken out the summation as the average action value $2J^{\mathrm{D},\phi}$, leading to:

$$\left.\frac{\sigma_{2J^{\mathrm{D},\phi}}}{2J^{\mathrm{D},\phi}}\right|_{\beta_i^{\mathrm{D},\phi}} \approx \frac{1}{\mathrm{N}'}\sqrt{\sum_{i=1}^{\mathrm{N}'}\left(\frac{\sigma_{\beta_i^{\mathrm{D},\phi}}}{\beta_i^{\mathrm{D},\phi}}\right)^2} \approx \frac{\sqrt{\mathrm{N}'}}{N}\frac{\overline{\sigma_{\beta^{\mathrm{D},\phi}}}}{\beta^{\mathrm{D},\phi}} \tag{A.2}$$

The average relative error-bar from β^{ϕ} measured in several optics of 2017 was 0.9%.

$$\frac{\sigma_{2J^{\mathrm{D},\phi}}}{2J^{\mathrm{D},\phi}}|_{\beta_i^{\mathrm{D},\phi}} \approx 0.05\% \tag{A.3}$$

A.2 Tune uncertainty propagation in β^{A}-calculation.

The effect of the natural and driven tune uncertainty in the AC-dipole compensation have been analytically studied. Performing error propagation in Eq. 4.9. Lambda factor, used in the compensation of the AC-dipole effect is given by:

$$\lambda = \frac{\sin[\pi(\mathrm{Q_d} - \mathrm{Q})]}{\sin[\pi(\mathrm{Q_d} + \mathrm{Q}))]} \tag{A.4}$$

Its associated error, induced by the tune uncertainty, is given by:

$$\sigma_\lambda^2 = \left(\frac{\partial\lambda}{\partial Q_d}\sigma_{Q_d}\right)^2 + \left(\frac{\partial\lambda}{\partial Q}\sigma_Q\right)^2 \approx 2\left(\frac{\partial\lambda}{\partial Q}\sigma_Q\right)^2 \tag{A.5}$$

Assuming that the uncertainty of the natural tune $\sigma(Q)$ and the driven tune $\sigma(Q_d)$ are equivalent and equal to $\sigma(Q)$ and using the parity properties of the sinusoidal functions, the two terms of Eq. A.4 are equivalent. Applying trigonometrical identities, the numerator of Eq. A.4 can be expressed as:

$$\begin{aligned}
\sigma_\lambda^2 &= 2\left(\frac{\pi\cos[\pi(\mathrm{Q_d} - \mathrm{Q})]\sin[\pi(\mathrm{Q_d} + \mathrm{Q})] - \pi\cos[\pi(\mathrm{Q_d} + \mathrm{Q})]\sin[\pi(\mathrm{Q_d} - \mathrm{Q})]}{\sin^2\pi(Q_d + Q)}\right)^2 \sigma_Q^2 \\
&= 2\left(\frac{\pi(\cos\pi Q_d\cos\pi Q + \sin\pi Q_d\sin\pi Q)\times(\sin\pi Q_d\cos\pi Q + \cos\pi Q_d\sin\pi Q)}{\sin^2\pi(Q_d + Q)}\right)^2 \sigma_Q^2 \\
&+ 2\left(\frac{\pi(\sin\pi Q_d\sin\pi Q - \cos\pi Q_d\cos\pi Q)\times(\sin\pi Q\cos\pi Q_d - \sin\pi Q_d\cos\pi Q_d)}{\sin^2\pi(Q_d + Q)}\right)^2 \sigma_Q^2 \\
&= 2\pi^2\left(\frac{2\cos\pi Q_d\sin\pi Q_d(\cos^2\pi Q + \sin^2\pi Q)}{\sin^2\pi(Q_d + Q)}\right)^2 \sigma_Q^2 = 2\pi^2\left(\frac{2\cos\pi Q_d\sin\pi Q_d}{\sin^2\pi(Q_d + Q)}\right)^2 \sigma_Q^2.
\end{aligned} \tag{A.6}$$

The maximum uncertainty introduced in the β calculation due to previously computed error in λ calculation is therefore given by:

$$\sigma_{\beta_i}|_{\sigma\lambda} = \frac{(A_{\mathrm{i}}^{\mathrm{D,meas.}})^2}{2J_C^{\mathrm{D}}}\frac{2}{(1-\lambda)^2}\sigma\lambda. \tag{A.7}$$

A.3 β-beating evolution in a lattice with errors

The perturbed β function in a ring is expressed as a function of the amplitude and phase of the generating driving term f_{2000} [139] and the unperturbed β_{model} function, as

$$\beta^{\mathrm{meas.}} = \beta^{\mathrm{model}}(1 + 32|f_{2000}|^2 + 8|f_{2000}|\sin q_{2000}) \ , \tag{A.8}$$

where $|f_{2000}|$ and q_{2000} are the amplitude and phase of the generating function term. With many small random errors $|f_{2000}|$ and $\sin q_{2000}$ would tend to be uncorrelated giving a ring-average β-beating of

$$\left\langle \frac{\Delta\beta^\phi}{\beta^{\mathrm{model}}} \right\rangle = 32\langle|f_{2000}|^2\rangle \ . \tag{A.9}$$

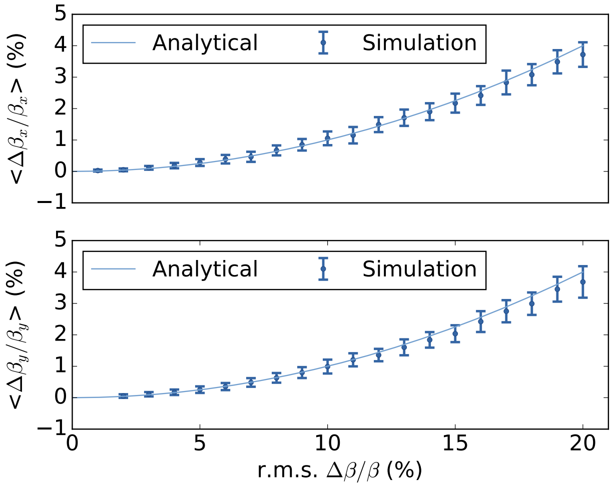

Figure A.1: Beta-beating average as a function of the beta-beating rms considering only BPMs placed in the ARCs.

The rms of the β-beating around the ring is given by:

$$rms\left(\frac{\Delta\beta^{\phi}}{\beta^{\text{model}}}\right) = \sqrt{\frac{1}{C}\int_0^C 64|f_{2000}|^2 \sin^2 q_{2000}\, ds}\ . \tag{A.10}$$

Using that $\sin^2 x = (1-\cos 2x)/2$ and, again, the assumption that $|f_{2000}|$ and q_{2000} are uncorrelated, the standard deviation takes the form

$$rms\left(\frac{\Delta\beta^{\phi}}{\beta^{\text{model}}}\right) = \sqrt{32\langle|f_{2000}|^2\rangle}\ . \tag{A.11}$$

From Eqs. (A.9) and (A.11) the following identity is obtained

$$\left\langle\frac{\Delta\beta^{\phi}}{\beta^{\text{model}}}\right\rangle = rms^2\left(\frac{\Delta\beta_i^{\phi}}{\beta_i^{\text{model}}}\right)\ , \tag{A.12}$$

which implies that the ring-average β function increases with the square of the standard deviation of the β-beating, also known as rms β-beating. This seems to be a universal property of all lattices since no assumptions on the lattice is made other than random error sources. The relation between these two quantities, average β-beating and rms β-beating have been studied in MADX simulations. Figure A.1 shows the LHC Ballistic simulations including the prediction from Eq. (A.12).

Action calculation $2J_{\text{C}}^{\text{D}}$ introduced in Ch. 4, can be alternatively computed using a model β function provided by MADX [109]. Expanding the action calculation $2J_{\text{C}}^{\phi}$ using $\beta_i^{\phi} = \beta_i^{\text{model}} + \Delta\beta_i^{\phi}$, it is possible to obtain the deviation introduced in the action calculation when a model values it is used as a reference value:

$$\begin{aligned}
2J_C^\phi &= \frac{1}{\mathrm{N}}\sum_{i=1}^{N}\frac{\left(A_i^{\mathrm{measured}}\right)^2}{\beta_i^\phi} = \frac{\left(A_i^{\mathrm{measured}}\right)^2}{\beta_i^{\mathrm{model}}+\Delta\beta_i^\phi} = \frac{1}{\mathrm{N}}\sum_{i=1}^{N}\frac{\left(A_i^{\mathrm{measured}}\right)^2}{\beta_i^{\mathrm{model}}\left(1+\Delta\beta_i^\phi/\beta_i^{\mathrm{model}}\right)}\\
&\approx \frac{1}{\mathrm{N}}\sum_{i=1}^{N}\frac{\left(A_i^{\mathrm{measured}}\right)^2}{\beta_i^{\mathrm{D,model}}}\left[1-\left(\frac{\Delta\beta_i^\phi}{\beta_i^{\mathrm{model}}}\right)\right] \approx 2J_{\mathrm{C}}^{\mathrm{model}} - \frac{1}{\mathrm{N}}\sum_{i=1}^{N}\left(\frac{\Delta\beta_i^\phi}{\beta_i^{\mathrm{model}}}\right)\frac{A_i^{\mathrm{measured}}}{\beta_i^\phi}\\
&\approx 2J_{\mathrm{C}}^{\mathrm{model}}\left[1-\sigma^2\left(\frac{\Delta\beta_i^\phi}{\beta_i^{\mathrm{model}}}\right)\right]
\end{aligned}\tag{A.13}$$

$$\frac{2J_C^\phi - 2J_C^{\mathrm{model}}}{2J_C^{\mathrm{model}}} \approx \sigma^2\left(\frac{\Delta\beta_i^\phi}{\beta_i^{\mathrm{model}}}\right). \tag{A.14}$$

The relative error introduced in the action calculation when using a β-model is proportional to the rms β-beating errors. Since the rms β-beating is a always positive, the action calculation will be sistemaytically underestimated.

A.4 $\beta^{\mathrm{A}}/\beta^\phi$ spread

The spread of the ratio $\beta^{\mathrm{A}}/\beta^\phi$-function over the BPMs can be analytically estimated. This spread depends on the spread associated with the calibration factors of the specific BPM type being studied, the action error-bar and the average relative β^ϕ error-bar. In case the BPMs have been re-calibrated, then the relative error-bar associated with the Ballistic calibration factor contribute to the spread replacing the spread associated with the calibration factors.

Relative error-bar β^ϕ have been analyzed for several optics in LHC measured in 2017 as shown in Fig. 5.1. In the case of standard BPMs the average relative error-bar β^ϕ is approximately 1% with a spread of 0.3% independently of the optics analyzed. In the case of stripline BPMs, the relative errorbar β^ϕ depends on the optics, for the optics analyzed in Ch. 5, the average relative error-bar is approximately 2% with a 0.6% spread.

The spread associated to the ratio $\beta^\phi/\beta^{\mathrm{A}}$ is generated by three different contributions: the spread associated to the calibration factors distribution $\left(\frac{2\sigma(C^{\mathrm{A}})}{C_i^2}\right)$, the spread associated to the action calculation $\left(\frac{2\sigma(C^{\mathrm{A}})}{\sqrt{N'-1}}\right)$ and the relative β^ϕ-errorbar $\left(\frac{\sigma_{\beta^\phi}}{\beta^\phi}\right)$. The analysis has been divided into three possible scenarios according to the BPMs being analyzed: standard, stripline and stripline calibrated:

- Standard

$$\sigma\left(\frac{\beta^{\mathrm{A}}}{\beta^{\phi}}\right)^2 = \left(\frac{2\sigma(C^{\mathrm{A}})}{\overline{C_i^2}}\right)^2 + \left(\frac{2\sigma(C^{\mathrm{A}})}{\sqrt{N'-1}}\right)^2 + \left(\frac{\sigma_{\beta^{\phi}}}{\beta^{\phi}}\right)^2 \approx \left(\frac{2\sigma(C^{\mathrm{A}})}{\overline{C_i^2}}\right)^2 + 0.01^2. \tag{A.15}$$

- Stripline

$$\sigma\left(\frac{\beta^{\mathrm{A}}}{\beta^{\phi}}\right)^2 = \left(\frac{2\sigma(C^{\mathrm{A,stripline}})}{\overline{C_i^2}}\right)^2 + \left(\frac{2\sigma(C^{\mathrm{A}})}{\sqrt{N'}}\right)^2 + \left(\frac{\sigma_{\beta^{\phi}_{\mathrm{Stripline}}}}{\beta^{\phi}_{\mathrm{Stripline}}}\right)^2 \approx \left(\frac{2\sigma(C^{\mathrm{A}})}{\overline{C_i^2}}\right)^2 + 0.02^2. \tag{A.16}$$

- Stripline calibrated. In this case, the effect of the calibration factor spread is substituted by the calibration factors uncertainty measured using the Ballistic optics.

$$\sigma\left(\frac{\beta^{\mathrm{A}}}{\beta^{\phi}}\right)^2 = \left(\frac{\sigma_{C_i^{\mathrm{Ballistic}}}}{C_i^{\mathrm{Ballistic}}}\right)^2 + \left(\frac{2\sigma(C^{\mathrm{A}})}{\sqrt{N'}}\right)^2 + \left(\frac{\sigma_{\beta^{\phi}_{\mathrm{Stripline}}}}{\beta^{\phi}_{\mathrm{Stripline}}}\right)^2 \approx 0.02^2 + 0.005^2 \tag{A.17}$$

$$\sigma\left(\frac{\beta^{\mathrm{A}}}{\beta^{\phi}}\right) \approx \sqrt{0.02^2 + 0.005^2} \approx 2\%. \tag{A.18}$$